

Mikko Vänskä

Defining the keyhole modes – the effects on the weld geometry and the molten pool behaviour in high power laser welding of stainless steels

Thesis for the degree of Doctor of Science (Technology) to be presented with due permission for public examination and criticism in the Auditorium 1383 at Lappeenranta University of Technology, Lappeenranta, Finland on the 17th of December, 2014, at noon.

Acta Universitatis
Lappeenrantaensis 625

Supervisor	Professor Antti Salminen Laboratory of Laser Materials Processing Faculty of Technology LUT Mechanical Engineering Lappeenranta University of Technology Finland
Reviewers	Professor John Powell Luleå University of Technology Sweden Doctor Tommi Jokinen ITER Organization France
Opponent	Professor Emeritus Helmut Hügel Institut für Strahlwerkzeuge University of Stuttgart Germany

ISBN 978-952-265-733-6
ISBN 978-952-265-734-3 (PDF)
ISSN-L 1456-4491
ISSN 1456-4491
Lappeenranta teknillinen yliopisto
Yliopistopaino

Abstract

Mikko Vänskä

Defining the keyhole modes – the effects on the weld geometry and the molten pool behaviour in high power laser welding of stainless steels

Lappeenranta

112 pages and 31 pages of appendices.

Lappeenranta University of Technology

Dissertation, Lappeenranta University of Technology

ISBN 978-952-265-733-6, ISBN 978-952-265-734-3 (PDF), ISSN 1456-4491

Keyhole welding, meaning that the laser beam forms a vapour cavity inside the steel, is one of the two types of laser welding processes and currently it is used in few industrial applications. Modern high power solid state lasers are becoming more used generally, but not all process fundamentals and phenomena of the process are well known and understanding of these helps to improve quality of final products. This study concentrates on the process fundamentals and the behaviour of the keyhole welding process by the means of real time high speed x-ray videography. One of the problem areas in laser welding has been mixing of the filler wire into the weld; the phenomena are explained and also one possible solution for this problem is presented in this study.

The argument of this thesis is that the keyhole laser welding process has three keyhole modes that behave differently. These modes are trap, cylinder and kaleidoscope. Two of these have sub-modes, in which the keyhole behaves similarly but the molten pool changes behaviour and geometry of the resulting weld is different. X-ray videography was used to visualize the actual keyhole side view profile during the welding process. Several methods were applied to analyse and compile high speed x-ray video data to achieve a clearer image of the keyhole side view. Averaging was used to measure the keyhole side view outline, which was used to reconstruct a 3D-model of the actual keyhole. This 3D-model was taken as basis for calculation of the vapour volume inside of the keyhole for each laser parameter combination and joint geometry.

Four different joint geometries were tested, partial penetration bead on plate and I-butt joint and full penetration bead on plate and I-butt joint. The comparison was performed with selected pairs and also compared all combinations together.

Keywords: laser welding, keyhole modes, stainless steel, molten pool behaviour

UDC 621.791.725:669.14:669-154:004.942

Tiivistelmä

Mikko Vänskä

Avaimenreiän moodien määrittäminen – vaikutukset hitsin geometriaan ja hitsisulan käyttäytymiseen ruostumattomien terästen suurteholaserhitsauksessa

Lappeenranta

112 sivua ja 31 sivua liitteitä.

Lappeenrannan teknillinen yliopisto

Väitöskirja, Lappeenrannan teknillinen yliopisto

ISBN 978-952-265-733-6, ISBN 978-952-265-734-3 (PDF), ISSN 1456-4491

Avaimenreikähitsaus, jossa lasersäde muodostaa kappaleeseen sylinterimäisen höyryreiän, on toinen laserhitsausmenetelmä ja käytössä joissakin teollisissa sovelluksissa. Modernit suuritehoiset kiinteän olomuodon laserit ovat nousseet yhdeksi suosituimmaksi lasertyypiksi, mutta kaikki prosessimekanismit ja periaatteet eivät ole tunnettuja ja näiden ymmärtäminen auttaa parantamaan tuotteen laatua. Tämä tutkimus keskittyy prosessiperusteisiin ja avaimenreiän käyttäytymiseen joita tutkittiin prosessin aikaisella suurnopeusröntgenvideokuvauksella. Yksi laserhitsauksen ongelma-alueista on ollut lisäaineen sekoittuminen hitsiin; sekoittumisen mekanismi on selitetty ja yksi mahdollinen ratkaisu ongelmaan esitetty tässä työssä.

Kirjan väitös on, että kolme erilaista avaimenreiän moodia esiintyy ja käyttäytyvät eri tavalla. Nämä moodit ovat ansa, sylinteri ja kaleidoskooppi. Kahdella näistä on alamoodeja, joissa avaimenreikä käyttäytyy samalla tavalla mutta hitsisula muuttaa käytösperiaatteita ja lopullisen hitsin geometria on erilainen. Röntgenkuvausta käytettiin visualisoimaan avaimenreiän sivuprofiili prosessin aikana. Useita erilaisia menetelmiä käytettiin kuvien ja videoiden käsittelyyn joilla saatiin selvempi kuva avaimenreiän sivuprofiilista. Kuvien keskiarvolaskentaa käytettiin apuna avaimenreiän sivuprofiilin hahmottamiseen, jota käytettiin rekonstruoimaan avaimenreiän 3D-malli. Tämä 3D-malli oli pohjana avaimenreiän höyrytilavuuden laskemiseen jokaiselle laserparametrikombinaatiolle ja liitosmuodolle.

Neljää erilaista liitosmuotoa testattiin, ne olivat vajaan tunkeuman päällehitsi ja vajaan tunkeuman I-liitos ja läpätunkeuman päällehitsi ja läpätunkeuman I-liitos. Vertailu tehtiin valituille pareille ja lisäksi kaikille parametrikombinaatioille yhdessä.

Avainsanat: laserhitsaus, avaimenreiän moodit, ruostumaton teräs, sulan käyttäytyminen

UDK 621.791.725:669.14:669-154:004.942

Acknowledgements

This thesis was carried out at the Laboratory of Laser Materials Processing of Lappeenranta University of Technology, Lappeenranta, Finland, during December 2011 and December 2014 and at the Institut für Strahlwerkzeuge, University of Stuttgart, Germany, as a visiting researcher, during December 2011 and December 2012 with the experiments and parts of the analysis.

This study is a part of the Finnish Metals and Engineering Competence Cluster's (FIMECC Oy) program Innovation & Network in the project Trilaser. I also want to thank Pamowe-project of Academy of Finland for additional financial support. A part of the funding has been given by Outokumpu Stainless Research Foundation and without them it wouldn't have been possible to start this study. I also want to thank Lappeenranta University of Technology Foundation for their financial support during the exchange period and allowing my researcher exchange to University of Stuttgart and the Lappeenranta University of Technology's Faculty of Technology with mobility support during the exchange.

I want to greatly thank my supervisor, Professor Antti Salminen for his guidance and comments on the thesis. He's been pushing me to finish the thesis and helped a lot along the way.

For valuable comments, grammatical corrections and suggestions on the thesis I want to greatly thank following people: Professor John Powell from Laser Expertise Ltd., England / Luleå University of Technology, Sweden, who acted as a reviewer. Reviewer Dr. Tommi Jokinen from ITER Organisation, France and Professor Emeritus Helmut Hügel from IFSW, Germany, who acted as an opponent.

I thank the following people, they have helped me with different phases of the process. Mr. Felix Abt from IFSW, currently at Orell Füssli Security Printing Ltd., Switzerland, for the experiments and help with the articles. Mr. Meiko Boley from IFSW, for the experiments and he also taught me image processing. Professor Staffan Hertzman from KTH / Outokumpu Stainless Research Foundation, Sweden, he has been involved from the start giving support and good comments on the thesis. Dr. Rudolf Weber from IFSW, he has been guiding during the article writing process. Professor Thomas Graf, who also has been involved with the experiments and helped with the article writing process. Terho Torvinen, who helped in the start of the thesis process.

I also want to thank all IFSW personnel. The year in Germany was extremely enjoyable and I learned a lot and got the thesis done. Thank you for the help!

I want to deeply thank Ms. Anna Unt from LUT Laser, she has given valuable comments, corrections and suggestions; also for her support and encouragement. I want to greatly thank Mrs. Anne Kalliosaari, from LUT Laser, she has given valuable corrections and comments on the manuscript and helped me during the thesis process.

To all colleagues from Lappeenranta University of Technology Laser Laboratory, thank you for the help and support. I want to thank Lappeenranta University of Technology for this opportunity.

I want to thank everyone who has been a part of this work and all projects that this work is connected to.

Great gratitude and thank you for my parents Sirpa and Lars who helped me during all phases of studies and with their help it was possible to advance so far. This wouldn't have been possible without them. I want to thank my sister Marika for her support and encouragement.

To my greatest inspirations and loves of my life and the biggest thank for my lovely and beautiful wife Anne who has been extremely supportive and patient during these years and to our children Senni and Essi. They have given me the energy to finish this and all were abroad during the researcher visit year. I also want to thank our lovely dogs, Sumu and Xara, who actually have helped me to get lots of fresh air and thus keeping my head clear by daily exercise.

Mikko Vänskä,

December, 2014.

Abbreviations

Short	Units	Explanation	Value if applicable
[au]	-	Arbitrary units, values without a specific unit.	
BOP		Bead on plate, weld made onto a flat plate	
c	m/s	Speed of light in vacuum	299 792 458
C-mode		Keyhole cylinder mode	
CO ₂		Carbon dioxide	
	°C	Degrees in Celsius	
dl		Travelled distance	
dN/N		The fraction of particles that does interact when travelling a distance in a material	
e	coulombs	Electron charge	
E	eV	Photon energy	
EK		Keyhole even width kaleidoscope mode	
EN 1.4301		Austenitic stainless steel, 0.02 C, 18.1 Cr, 8.1 Ni (in weight % according to EN standard)	
EN 1.4404		Austenitic stainless steel, 0.02 C, 17.2 Cr, 10.1 Ni, 2.1 Mo (in weight % according to EN standard)	
	eV	Electron volts	
FP		Full penetration	
FPD	mm	Focal point diameter	
FPP	mm	Focal point position	
FPS		Frames per second	
h	Js	Planck's constant	6.626 069 57×10 ⁻³⁴
hsNT		High speed narrow trap mode	
IBJ		I-butt joint, a joint type consisting of two plates with straight edges	
Ionisation		When an electron is freed from its atom by absorbed energy	
K-mode		Keyhole kaleidoscope mode	
KH		Keyhole	
Kalman filter		A stack filter that has a calculation method for image sequences that improves image quality but reduces time resolution	
Kernel		An area or a length in an image to be processed per one cycle	
λ	m or nm	Wavelength	
λ _{min}	nm	Short wavelength limit of an x-ray tube, the minimum emitted wavelength of the tube	
Laser		Light amplification of stimulated emission of radiation	
LK		Large opening kaleidoscope mode	
lsNT		Low speed narrow trap mode	

μ	1/m	Linear attenuation coefficient	
μ/ρ	m ² /kg	Mass attenuation coefficient	
MAC		Mass Attenuation Coefficient, Absorption or scattering probability when photons are travelling a layer of material with density dependence removed	
NT		Keyhole narrow T-mode	
OVAT		One variable at a time	
p, penumbra		Gradient shadow of an edge, i.e. when an object edge does not have a sharp shadow	
Plasma		High temperature ionised material	
PP		Partial penetration	
P	g/cm ³	Density	
Rayleigh length	mm	A length from FFP to the location in beam path in which the beam radius increases by $\sqrt{2}$	
Ru		The average of linearly polarised light perpendicular and parallel to the surface	
SSL		Solid state laser	
T-mode		Keyhole trap mode	
TFT		Thin-film-transistor	
V ₀	V	Potential difference of the x-ray tube	
WT		Wide T-mode	
X-rays	Å	Electromagnetic radiation wavelength range of x-rays	0.01 to 10
X-ray dose	[au]	An amount of x-ray radiation on a target	
Yb		Ytterbium	
Å		Ångström, unit used in x-ray terminology, presents wavelength	
	nm	1 Ångström in nanometres	0.1

Additional material data

Material data of the stainless steel main alloying elements and tracer materials. To be used for molten pool behaviour mechanics discussions and mass attenuation references. (Dragoset et al. 2013) (MaTeck GmbH 2008)

Atomic numbers

	Chromium	24
	Iron	26
	Nickel	28
	Molybdenum	42
	Tungsten	74

Melting points

	Chromium	1 890
	Iron	1 535
°C	Nickel	1 453
	Molybdenum	2 617
	Tungsten	3 410

Boiling points

	Chromium	2 640
	Iron	2 750
°C	Nickel	2 732
	Molybdenum	5 560
	Tungsten	5 657

List of publications

Some parts of this thesis have been published in four articles, listed below. These articles are not directly a part of this thesis but are cited in the thesis text.

Main author

Vänskä, M, Abt, F, Weber, R, Salminen, A & Graf, T 2012, 'Investigation of the keyhole in laser welding of different joint geometries by means of X-Ray videography', Proc of the Int. Congress on Applications of Laser & Electro-Optics, Laser Institute of America. Anaheim.

Vänskä, M, Abt, F, Weber, R, Salminen, A & Graf, T 2013, 'Effects of welding parameters onto keyhole geometry for partial penetration laser welding', Physics Procedia, vol 41, pp. 199-208.

Vänskä, M, Abt, F, Weber, R, Salminen, A & Graf, T 2014, 'Effects of welding parameters and joint geometry to keyhole geometry and vapour volume', 16th International Workshop on Process fundamentals of laser welding and cutting, Institut für Strahlwerkzeuge, Universität Stuttgart. Hirschegg.

Co-author

Lappalainen, E., Unt, A., Sokolov, M., Vänskä, M. & Salminen, A. 2013. Laser welding with high power laser: The effect of joint configuration. The 14th Nordic Laser Materials Processing Conference (NOLAMP 14). Luleå University of Technology. Gothenburg.

Table of contents

Abstract	3
Tiivistelmä	4
Acknowledgements	5
Abbreviations	7
Additional material data	9
List of publications	10
Table of contents	11
1 Background	13
2 Introduction	14
2.1 Laser	14
2.2 Austenitic stainless steels, and laser beam interaction	15
2.3 Keyhole welding	16
2.4 General effects of the parameters on the keyhole	20
2.5 X-ray techniques and videography	21
2.6 X-ray videography in laser welding	25
2.7 Modern x-ray videography in laser welding	28
2.8 Conclusions of previous studies	33
2.9 Image processing	33
2.10 Keyhole modelling and calculations	34
2.11 Mass attenuation coefficient	36
3 Experimental Methods	37
3.1 Flow chart of the experiments	37
3.2 Materials	38
3.3 Joint types	39
3.4 Equipment	40
3.4.1 Laser	40
3.4.2 X-ray	40
3.4.3 Cameras	40
3.4.4 Other equipment	41
3.5 Parameter variables	43
3.5.1 Welding speeds	44
3.5.2 Focal point positions	44
3.5.3 Laser power	44
3.5.4 Materials	44
3.5.5 Sample thicknesses	44
3.5.6 Joint types	44
3.6 Tracer experiment parameters	45
3.7 Visual weld evaluation	46

3.8	Image processing	47
3.9	Sample top side high speed video processing methods	48
3.10	Determining keyhole side view outline	49
3.11	Keyhole reconstruction and keyhole geometry calculation	53
3.12	Melting efficiency	55
3.13	Tracer material selection	55
4	Results and analysis	56
4.1	Keyhole and weld geometry	56
4.1.1	Keyhole opening area	57
4.1.2	Keyhole volumes	61
4.1.3	Partial penetration keyhole and weld depths	64
4.1.4	Partial penetration keyhole and weld cross-section areas	67
4.1.5	Full penetration keyhole and weld cross-section areas	69
4.1.6	Keyhole front inclination angles	70
4.1.7	Weld top surface bead widths	73
4.2	Keyhole modes	74
4.2.1	Trap mode (Keyhole T-mode)	75
4.2.2	Cylinder (Keyhole C-mode)	78
4.2.3	Kaleidoscope (Keyhole K-mode)	80
4.2.4	Modes table	82
4.3	Tracer material and flow patterns in the molten pool	83
4.3.1	Tracer wire with partial penetration	84
4.3.2	Tracer powder with full penetration	86
4.3.3	Tracer powder with partial penetration	87
4.3.4	High speed partial penetration	88
4.3.5	Random images and averages	89
4.4	Melting efficiency and filling capability	90
5	Discussion	94
5.1	Keyhole geometry and efficiency	94
5.2	Flow patterns	97
5.3	Keyhole modes	98
5.4	General	99
6	Conclusions	101
7	Future work	103
	Bibliography	104
	Appendices	112

1 Background

This study concentrated on the behaviour of the keyhole and how the change of values of each main parameter type changed the keyhole geometry. The main parameters were welding speed, focal point position and joint type. This resulted in more detailed information of the keyhole geometry and the molten pool behaviour when the laser parameters were altered or when the joint type changed. This study helps to understand the behaviour of the keyhole and how four different joint geometries affect the keyhole and weld behaviour and geometry.

The most common way of performing welding experiments has been to start with bead on plate experiments, meaning that there are no joint edges in the welding path. Additionally these parameters are used also for I-butt joint, which is the most common joint type in high power laser welding. With certain parameters and parameter windows this method results in a stable process for both joint types and this area is shown in this thesis. There are also parameter windows in which the bead on plate method is not suitable for comparing welding experiments with I-butt joint.

The main objective of the thesis is to provide a deeper understanding of the laser keyhole welding process through analysis of the experimental data of the keyhole behaviour under pre-defined conditions. One of the main objectives was to understand how the joint geometry changes the keyhole geometry, its behaviour and the resulting weld geometry. The vapour volumes for each parameter combination were calculated through 3D-reconstruction of the actual keyhole geometry and this was used to compare the effect of each parameter on the vapour volume.

The argument of this work is that three main keyhole modes exist and these behave differently and have an effect on the molten pool behaviour and the weld geometry. The main modes are the trap mode (T-mode), the cylinder mode (C-mode) and the kaleidoscope mode (K-mode). Seven sub-modes also exist, each having their own features, such as narrow trap (NT), wide trap (WT), high speed narrow trap (hsNT), low speed narrow trap (lsNT), even width kaleidoscope (EK), large opening kaleidoscope (LK) and open cone (OC) modes. The sub-modes have their own features, but cannot be defined as a main keyhole mode due to same keyhole geometry but acting in different welding speed which causes different molten pool behaviour. These could be defined as different molten pool behaviour regimes but the keyhole modes are the main topic in this thesis. These keyhole modes are described and explained in this thesis, the data for the analysis was based on the real time high speed x-ray videography imaging of the keyhole welding process.

2 Introduction

Laser technology has already been used in industry for several decades and the application range is still increasing continuously. Modern solid state lasers (SSLs) have some advantages over older technology lasers, such as CO₂- and Nd:YAG-lasers by allowing higher wall-plug efficiency, for example. Modern SSL's can have high beam quality, which means that the focal point diameter can be small, down to approximately one hundred micrometres with a multi-mode multi-kilowatt lasers and ten micrometres with a single mode laser in the multi-kilowatt range. With a high power laser it is possible to achieve deep penetration welding resulting in a high depth to width ratio. These welds can be less than a one millimetre in width but more than ten millimetres deep. In the process called keyhole welding, the laser beam forms a deep vapour cavity by vaporising the metal. The keyhole moves with the laser beam along the joint melting the material in front of it. The molten metal gives way to the keyhole, flows along the edges of the keyhole, and behind the keyhole it cools, solidifies, and forms the weld. The molten metal movement can be relatively random, meaning that the molten metal can flow any direction in the molten pool.

Even though heavy industry has become increasingly interested in laser technology due to the advantages enabled by the use of the technology; the behaviour and the dynamics inside the keyhole and in the molten pool are partly unknown. Knowing the process thoroughly is extremely important for understanding the process behaviour and thus increasing the quality by understanding what causes the changes in the weld quality.

In the theoretical part of this work the main components of the used technology are explained and previous results from the area of subject are shown. This section consists of detailed information from the basics of modern solid state laser (SSL) technology to x-ray imaging methods and principles. Although the laser beam generation physics is important for the technology, this thesis concentrates mainly on the welding process itself, with the use of data acquired by the means of high speed x-ray videography.

2.1 Laser

The main principle of a laser is the amplification of light by stimulated emission of radiation inside the laser active medium; the theory was started by Einstein in 1916 and continued by invention of a theory of a laser by Schawlow and Townes in 1958 and finally the invention and building of the first published laser by Maiman in 1960. (Einstein 1916) (Schawlow & Townes 1958) (Maiman 1960) An extended explanation of the laser beam generation and modern high power disk laser can be found from appendix 23. CO₂-lasers have been the most used laser sources for welding applications but a new generation of SSLs now shares this market. The principles of a first modern disk laser was published by Giesen et al. from University of Stuttgart in the beginning of 1990's. (Giesen et al. 1994)

2.2 Austenitic stainless steels, and laser beam interaction

The materials used in this study were austenitic stainless steels EN 1.4301 and EN 1.4404. Austenitic stainless steels have usually a good weldability and are one of the most suitable metallic materials for laser welding. Austenitic stainless steels can have several characteristic welding defects if proper precautions are not taken, the main defects are solidification and liquation cracking. One of the precautions is to have clean surfaces as impurities can increase cracking susceptibility. (Lippold & Kotecki 2005) During the laser keyhole welding the material evaporates, which might cause, in some cases, loss of alloying elements and negatively influence corrosion resistance. The heat input also has an effect on the steel properties, but significantly less with austenitic stainless steels when compared to other types of stainless steels, such as ferritic, martensitic and duplex stainless steels. (David, Khan & Debroy 1988) (Westin 2010) (Westin & Fellman 2010) Stainless steels have several applications and with these steels laser welding allows deep penetration. Deep penetration and accurate welds are required in thick section, for example in fusion reactors and chemical industry, in which austenitic stainless steels are used. In some cases the welding processes requires additional features to achieve a sound weld, such as filler wire or optical manipulation of special types of joints. (Jokinen 2004) (Jokinen & Kujanpää 2003) (Vänskä & Salminen 2012)

The interaction between the laser beam and stainless steel occurs in the surface only, due to negligible photon penetration into the material at disk laser wavelength of 1030 nm. Optical penetration means the photon penetrates into the solid steel without melting or vaporising it, this is different behaviour from the keyhole process in which the material melts and vaporises. Bergström et al. have calculated the optical penetration into the steels with SSL photon wavelengths. As the optical penetration was in the range of tens of nanometres, its effect can be neglected. Reflection and reflectivity depends on the material surface and also of the welding process type. (Bergström, Powell & Kaplan 2007) The optical penetration of photons can be compared to x-rays, which are also photons but with significantly higher energies which changes penetration and absorption behaviour.

During keyhole welding of stainless steels the total absorption increases nearly to 90 percent according to Kawahito et al. and this percentage depends on the welding speed. The lower the welding speed, the higher the total welding absorption was in their study. (Kawahito et al. 2011) The absorption into and reflectance from a surface have been calculated for iron, but the quality of the surface has not been clearly presented in these calculations. One of the problems is that there are no calculations for austenitic stainless steels or different types of steel alloys for example. Figure 1 shows reflectance of iron for different wavelengths at melting and evaporation temperatures, in this graph the surface is molten iron. According to Olsen, the reflectivity does not change considerably when the temperature increases from melting to evaporation temperature. (Hügel & Dausinger 1999) (Olsen 2011) (Bergström, Powell & Kaplan 2007)

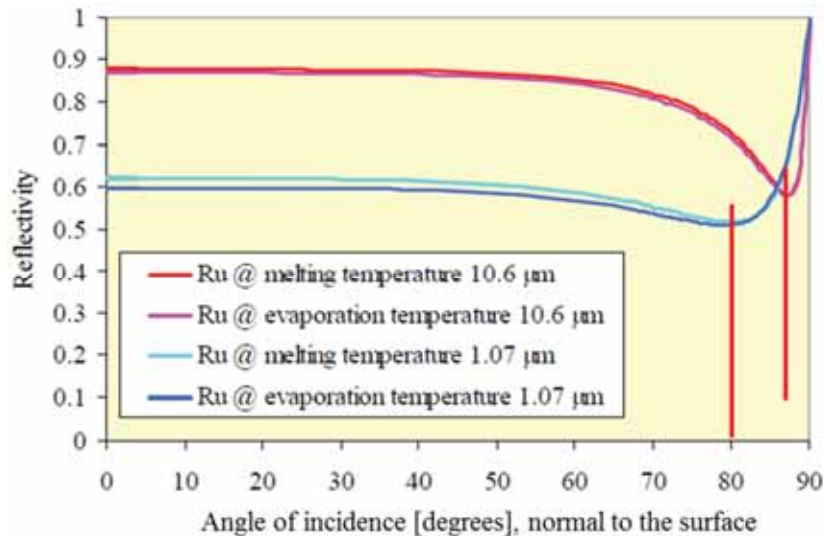


Figure 1. Reflectivity of Fe, iron. R_u is the average of linearly polarised light polarised perpendicular and parallel to the surface, meaning that the R_u value correspond the reflectivity of randomly polarised light. (Olsen 2011)

With SSLs a linearly polarised light is difficult to obtain and especially maintain throughout the process in most of the welding systems. The most common polarisation with disk lasers is random polarization, meaning that there is no dominating polarisation type. Due to very similar reflectance at melting and evaporation temperatures the laser beam behaves similarly independent of the temperature at the keyhole front wall, the molten front. The absorption peak, Brewster angle, occurs at approximately 80 degrees from normal to the surface. Below this angle, interaction angles between 87 and above, the reflectivity is significantly stronger than the absorption. Below the Brewster angle, <80 degrees normal to the surface, the absorption is relatively stable between 40 and 48 %. (Olsen 2011)

2.3 Keyhole welding

There are two main types of laser welding processes, conduction limited welding and the keyhole welding. In conduction limited laser welding the laser beam's energy only melts the material and a weld is formed when the molten metal solidifies behind the laser beam interaction zone. Keyhole welding is a slightly more complicated process due to different behaviour of the material at the laser beam's location. The laser beam is absorbed by the material, the material heats up, melts and starts to boil. This boiling effect forms in the case of stainless steels a metal vapour cavity, a keyhole, mainly of iron, chrome and nickel due to the composition of the stainless steel. When the laser welding head is moved, the molten metal flows around the keyhole and solidifies upon cooling forming the weld. The keyhole geometry varies according to the change in welding parameters.

So far two different keyhole types have been recognized, trap mode and cylinder mode. Of these modes the trap mode is more common compared to cylinder mode. Usually cylinder mode results in larger keyhole front angle, which means that the keyhole front wall is tilted backwards, which also affects beam path inside the keyhole. The main differences are that the keyhole front wall has larger angle, the bottom is almost flat and the penetration is significantly lower than in the light trap mode. (Vänskä et al. 2013) (Vänskä et al. 2014) These two modes can be distinguished from each other according to the laser beam behaviour inside the keyhole, in the cylinder mode the absorption on the front wall is higher resulting stronger vapour formation. Trap mode is a cone shaped and the light is reflected inside the cone deeper into the material. This is also called self-focusing effect, which was proven by Beck and Dausinger in 1989 (Beck & Dausinger 1989).

The basic principle of keyhole welding is presented in figure 2. The keyhole welding process is a relatively well-established technique. There have been major improvements in laser technology which affects the keyhole behaviour due to higher intensity while using modern lasers. The formation of a keyhole requires a power density of approximately 10^4 W/mm² with steels in general. (Semak et al. 1999)

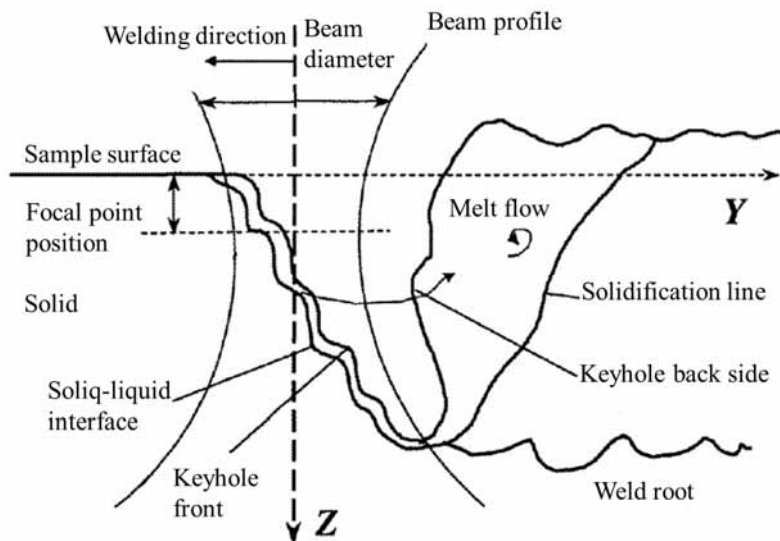


Figure 2. The principle of keyhole welding. (Semak et al. 1999)

Inside the keyhole a phenomenon called self-focusing effect occurs which means that the beam reflects from the side walls of the keyhole and the path changes towards the bottom which decreases in diameter. The first major publication concentrating on the subject was written by Beck et al. (1989), figure 3. The laser beam mode in their study was a Gaussian mode (or the laser beam mode in their study resembled Gaussian mode). By Gaussian beam mode is meant that the intensity is highest on the centre area of the beam area. (Beck & Dausinger 1989) A

laser beam from a multimode fibre results in a top hat mode at and near the focal point, in which the laser beam's energy is distributed relatively evenly in the whole area, but when the beam is inspected outside of the short "top hat area" length it becomes closer to Gaussian mode in which the highest intensity is in the centre. The area depends on the optics properties and cannot be determined as a common unit of length.

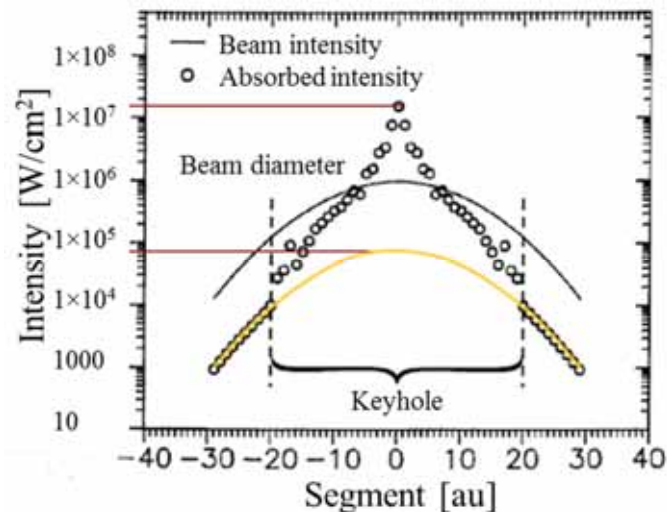


Figure 3. The self-focusing effect. Yellow line is the assumed absorbed intensity. The width, the segment is in arbitrary units, meaning without a determined unit type. (Beck & Dausinger 1989)

The self-focusing effect increases the depth of the keyhole by guiding the laser beam power into a smaller area increasing intensity and this creates more metal vapour and deeper penetration. The self-focusing effect also causes the trap mode keyhole. The keyhole behaviour is in fact a very complicated and strongly parameter dependant due to intensity changes, welding speed effects, and in some cases even a process gas can affect the behaviour. With keyhole welding, three different gas types can be used, which are plasma control-, shielding- and process gases. Plasma control gas is used only to extinguish possible plasma and intense metal vapour formation above the sample surface, shielding gas is used to protect the molten pool from oxidation and process gas can be used to affect the keyhole welding process itself. Fabbro tested the use of an accurately aimed gas jet to stabilise the keyhole. He used argon with 20 l/min through a 2 mm diameter nozzle, which increases the pressure inside the keyhole and thus stabilises the process. The used laser was solid state laser with power of 3 kW, 3 m/min welding speed and focal point diameter of 0.45 mm. Fabbro also stated that pressure generation from vaporisation of the steel might not be sufficient to keep the keyhole open completely resulting in unstable welding process. (Fabbro 2010) Matsunawa showed that the keyhole front wall had humps that were moving and that these humps created an intense evaporation points which caused fluctuations in the process. (Matsunawa 2002)

The energy transfer from the laser beam to the sample affects the keyhole behaviour. The complete energy transfer from the laser beam into the welded sample and to the weld in the end involves very complicated phenomena:

- direct surface absorption, also via possible plasma and metal vapour caused scattering, into the solid and the molten metal,
- absorption into the plasma, if present, and from the plasma via conduction, collision and radiation to the molten metal and to the solid surface,
- heat conduction inside the molten pool and the solid,
- heat convection inside the molten pool.

The heat transfers to the sample is mainly through absorption of the laser beam to the molten wall of the keyhole and the conduction and convection via and inside the molten metal also to the solid sample.

The laser beam itself does not interact considerably with the solid sample surface during a stable keyhole welding process with majority of the welding parameter combinations. This depends on the beam properties, for example a large Gaussian mode beam does interact with the solid sample on the sides heating the surfaces.

Different approaches have been tested in the past the goal being to observe the geometry of the keyhole underneath the sample's surface and understand its behaviour. Webster et al. for example, tested inline coherent imaging for measuring the keyhole depth; however this method reveals no spatially resolved information except the depth. (Webster et al. 2011) High speed imaging has also been used to study keyhole behaviour. According to Eriksson et al. the molten metal thickness in front of the keyhole can be approximately 100 μm and it was measured with 6 m/min welding speed, 6 kW laser power (fiber laser), focal point diameter of 900 μm and the material was austenitic stainless steel EN 1.4301. (Eriksson et al. 2010) (Eriksson, Powell & Kaplan 2013) Berger et al. studied the keyhole dynamics and the mechanisms of pore formation in laser welding of ice by using high speed cameras in the visual spectrum. They found out that basic principles are very similar in welding of ice than in the welding of steels. They also found that spiking, oscillations in the keyhole depth, in the case of ice welding is partly caused by the humps formed on the front wall of the keyhole. This probably occurs also with steels due to changed intensity distribution in the front wall. This means that a hump can prevent that particular part of the beam travelling deeper into the keyhole but increases local absorption on the hump possibly creating a momentary absorption peak causing high vaporisation pressure and momentary increase in keyhole depth. (Berger, Hugel & Graf 2011)

The most sophisticated method (up to date) for observation of the keyhole geometry and dynamics is the in-situ x-ray videography. The earliest x-ray images of the keyhole were likely taken by Arata's group in 1985. They used a 15 kW CO₂-laser to weld low alloyed steel of type

SM41. The purpose of these experiments was to study the effects of shielding gas onto the keyhole geometry. (Arata, Abe & Oda 1985) (Arata, Abe & Oda 1985)

2.4 General effects of the parameters on the keyhole

The inclination angle of the keyhole front has a dependency to the welding speed as shown in figure 4. (Weberpals & Dausinger 2008) The welding speed has also a direct effect on the penetration depth as can be noticed from the study by Matsumoto et al. (2008). In their research they used constant laser power (10 kW), but varied the welding speed from 1 to 6 m/min. For welding speeds 1, 3 and 6 m/min the penetrations were approximately 13, 11 and 9 mm. (Matsumoto et al. 2008) The molten pool dynamics on the surface, studied by Fabbro, was also strongly influenced by the welding speed. The regime below 5 m/min Fabbro called the Rosenthal regime. This regime was characterised with a large molten pool which was mainly increasing the molten pool length and width on the surface. Also strong fluctuations in the molten metal flow occurred in addition to spatter from the edges of the keyhole opening. The study concluded that the keyhole in this region was uniformly heated close to the vaporisation temperature. The second type was a single-wave regime, between 6 and 8 m/min, this was characterised by a large wave moving backwards behind the keyhole, meaning that the molten pool surface moves up and down thus possibly closing the keyhole momentarily. In this type, the keyhole was tilted backwards and the front keyhole wall was heated by the laser beam. Fabbro studied how the molten pool surface behaved and these regimes were based on the molten pool surface movements while using an Nd:YAG-laser with a 4 kW output power and a 0.6 mm focal point diameter. (Fabbro 2010) Salminen et al. showed that the keyhole is commonly slightly oval and excessively high welding speeds decrease penetration. (Salminen, Lehtinen & Harkko 2008) Shimokusu et al. concluded that the focal point position had a significant influence on the penetration depth and the process stability. (Shimokusu et al. 2002)

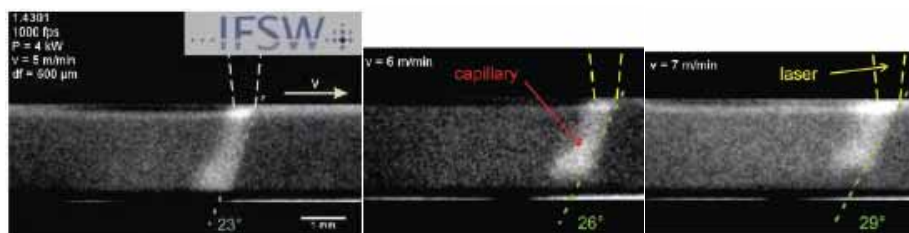


Figure 4. Experiments performed by Weberpals et al. at IFSW with welding speeds of 5, 6 and 7 m/min. (Weberpals et al. 2011)

The welding parameter selection can have a great impact on a weld cross section shape. High welding speed can form, in a case of copper welding, a droplet-shaped weld cross-section having a so called “big bubble” below the top surface even if the weld on the surface is narrow. (Heß 2012) The joint edge roughness can have an effect on the penetration depth, the optimal edge roughness can be used to increase weld penetration depth without increase in laser power.

Sokolov et al. and Lappalainen et al. also showed comparisons of machined edges with and without grit blasting and the bead on plate welding. The results showed that smooth surface could, in some cases, result in penetration close to that of bead on plate and the trend showed that rougher surfaces results in deeper penetration. (Sokolov et al. 2012) (Lappalainen et al. 2013)

2.5 X-ray techniques and videography

X-ray imaging is a well-known method for many applications. In manufacturing of steel products it is typically used for inspection and measurement of welds and samples of several different materials. There are several types of machines, but the main components in traditional x-ray imaging systems are the x-ray tube and the film.

X-rays, electromagnetic radiation photons in a certain wavelength range, are generated by stopping high velocity electrons on to a metal target, the anode. The x-ray tube consists of a glass or metal-ceramic vessel having a filament source of electrons, the cathode, on one side. The other side having the anode and output window. The vessel is almost a vacuum and can be sealed or vacuum pump operated. The wavelength spectrum from the x-ray is not very specific in general and the material and the acceleration voltage changes the minimum and maximum photon energies. In the x-ray terminology, Ångström units are used and the generalized x-ray spectrum is approximately from 0.01 to 10.0 Å, which means 0.01 to 1.0 nm in wavelength. (Halmshaw 1997)

As a simplified explanation; the x-rays penetrate through the sample and the energy passing through is absorbed by the film and forming an image of the sample onto the film. These films are for one time use and are not suitable for all applications. The positive features of the films are that they are inexpensive and still commonly available. Figure 5 shows the basic principle of the x-ray imaging in sample inspection. (Halmshaw 1997)

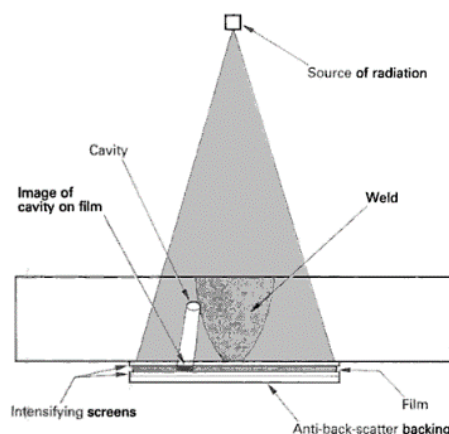


Figure 5. X-ray imaging station principle for sample inspection. (Halmshaw 1997)

Conventional photographic techniques are used to produce the final image of the sample; firstly the film is developed, then fixed, washed and dried. There are also automatic machines that perform the same sequence, as in photographing. When the film, an image, is ready for inspection, it must be illuminated by a light source positioned behind of it to see the image. These films can be scanned with special dual light scanners or by common digital cameras with an x-ray film reader, which have the light source for illumination.

Traditional film methods are not suitable for example for continuous x-ray imaging or real time x-ray videography of laser welding. For continuous x-ray imaging there are two digital radiography techniques, which are Direct Radiography (DR) and Computed Radiography (CR). The difference is that the computed radiography uses storage-phosphor image plates with a separate image readout process and the direct radiography converts the x-rays into electrical charges with direct readout processes.

In DR, the x-ray beams are converted directly into electrical charges or electro-magnetic radiation, photons. The type of conversion can be either direct conversion or indirect conversion. Figure 6 shows the principle of direct radiography. The indirect conversion is used in laser welding research. The direct conversion can have a rotating selenium-dotted drum with a positive electrical surface charge that is exposed to the x-rays. The change of the charge is proportional to the incident x-ray dose. The charge pattern is then converted into a digital image by an analogue-to-digital converter. The main issue in this method is the time it takes for the drum to rotate and transfer the charge. Other method is to have a selenium-based flat-panel detector in which the x-rays are directly converted into electrical charges in a fixed photoconductor layer and readout by a TFT-array under the photoconductor.

In DR systems with indirect conversion of the x-rays a regular digital high speed camera can be used and there is only a light intensity needed to register, which gives more choices of the cameras or the detectors. The scintillator plate, made of Tl(thallium)-doped caesium iodide, converts the x-ray beams into photons and then is recorded by a CCD, which converts the light into electrical charges and then it's transformed into a digital image. Usually there are some optical elements between the scintillator and the CCD such as collector lenses to reduce the size of the photon area. The drawback of this system is that the reduced amount of photons reaching the CCD causes a lower signal-to-noise ratio and a slightly lower quantum efficiency. The indirect conversion can also be made with a scintillator layer, an amorphous silicon photodiode circuitry and finally a TFT array to get the digital data. (Chotas, Dobbins & Ravin 1999)

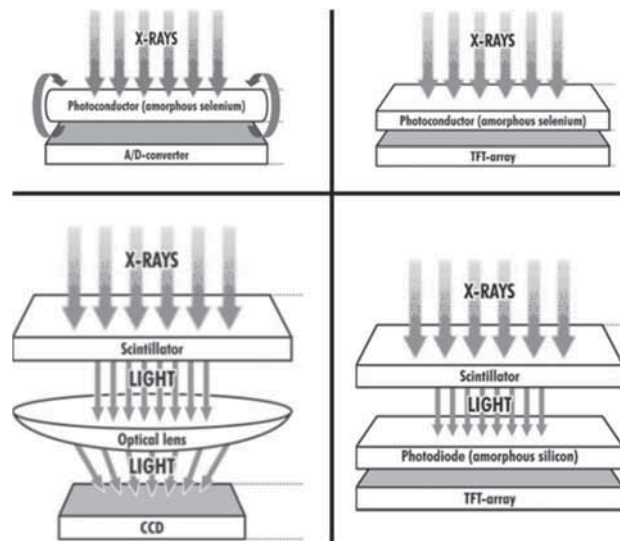


Figure 6. DR. Upper two are direct conversions and two below indirect conversions. (Körner et al. 2007)

There are several methods to perform radiography in general, however all of them have some specific limitations. Some are very good for stationary single imaging, while others can be used continuously. The radiography systems in laser welding research are using direct radiography with indirect conversion; this allows using a common high speed camera, which allows very high frames per second at relatively good resolution, generally at least 1024×1024 pixels. In a videography mode, the x-ray tube itself is continuous, so there are no synchronisation between the x-ray tube and the imaging system. In this process with metals, a geometrical shadow projection is used to see the changes in the sample; figure 7 shows the principle of this method. (Abt, Weber & Graf 2010)

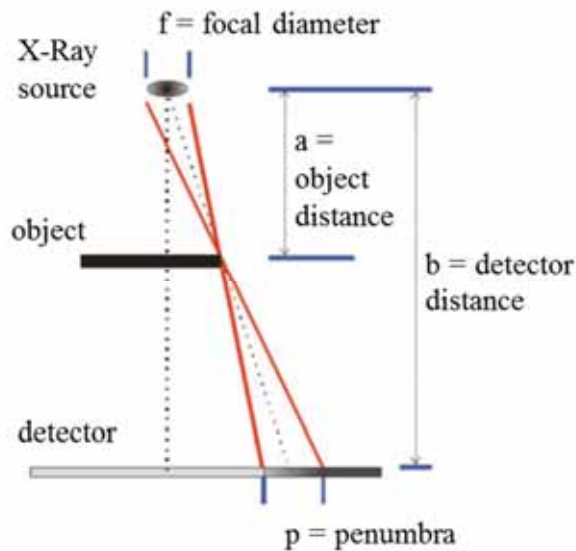


Figure 7. The projection system according to the principle of geometric shadow projection. (Abt, Weber & Graf 2010)

The same principle is used in all of the welding research x-ray videography systems; the x-ray produces a shadow of the sample to the scintillator. The changes in the sample, such as the keyhole, change the intensity that is recorded by the scintillator due to less material in the x-ray beam path. Due to the type of the source, in this case the anode, which is more like a surface that emits the beam, the shadow of the sample and the features are slightly blurry. Micro focused x-ray has a small focal diameter, which increases the sharpness of the image. With a large focal point mode the x-ray power is higher, but the accuracy is slightly lower. The reason for this is the geometrical shadow projection method used in the imaging. The main difference is the area of the light source, the photon source, x-ray target anode in this case. If the radiation source is large, the shadow of an object does not have sharp edges, but rather a shadow gradient from dark to light. With replacing the radiation source with a very small spot, the shadow has much sharper edges and the shadow gradient is much shorter. The same principle works also with all photon energy levels, the x-ray beams, a smaller source results in sharper edges in the image. This also allows seeing smaller features of the process. Geometrical shadow projection system also allows calculation of the magnification. (Abt, Weber & Graf 2010)

Image contrast is very important for observability of small structures in the sample. According to calculations by Abt et al. the contrast of the structures inside the sample is not dependant on the thickness of the sample or the x-ray intensity, but rather the size of the structure and attenuation factors. Which means how easily the material can be penetrated, of the base material and the structure, if there is enough x-ray intensity on the detector plate. The system still requires sufficient x-ray dose on the detector plate, the scintillator, for the features to be visible,

this is the reason why x-ray intensity is also important. The attenuation factors depend on the photon energy of the x-ray beam and a mass attenuation coefficient of the material. (Abt, Weber & Graf 2010)

In the x-ray imaging there is always some noise, which decreases the image quality due to varying grey values of pixels in the image. The mean grey value is the intensity of the x-rays to the detector. This noise and signal to noise ratio affects the image quality and also the detectability of small structures. This is due to the fact that structure and base material needs to have higher contrast ratio than the noise. (Abt, Weber & Graf 2010)

2.6 X-ray videography in laser welding

The keyhole has been observed with many different space and time resolved methods but the keyhole geometry inside steel is only visible with the x-ray videography. The x-ray imaging during the laser welding itself is a well-established method to examine the keyhole behaviour with side view through the material. First experiments were published by Arata et al. during 1985. (Arata, Abe & Oda 1985) (Arata, Abe & Oda 1985) Since then the focal point diameter has decreased and the brightness of the micro focused x-ray sources have significantly improved resulting much higher image quality. Image capturing has become faster and significantly more accurate by the increase of resolution and maximum possible sample width has increased, meaning that the modern high power x-rays are able to penetrate thicker metal samples.

In figure 8 is shown the development of quality aspect and also major breakthroughs in this field. The quality aspect means the accuracy, resolution and measurability of features in x-ray images and videos. The higher the quality aspect the smaller features are visible. The resolution is higher and the accuracy, meaning conformability of visible features, is better with higher image quality aspects. This actually means that in the early days it was not really known if there was a feature such as a keyhole tip or was it just noise in the image or in the video. Measurability means possibility to measure accurately all of the features, today it is well known what the magnification of the system is and with this information it is possible to calculate the scale of the images.

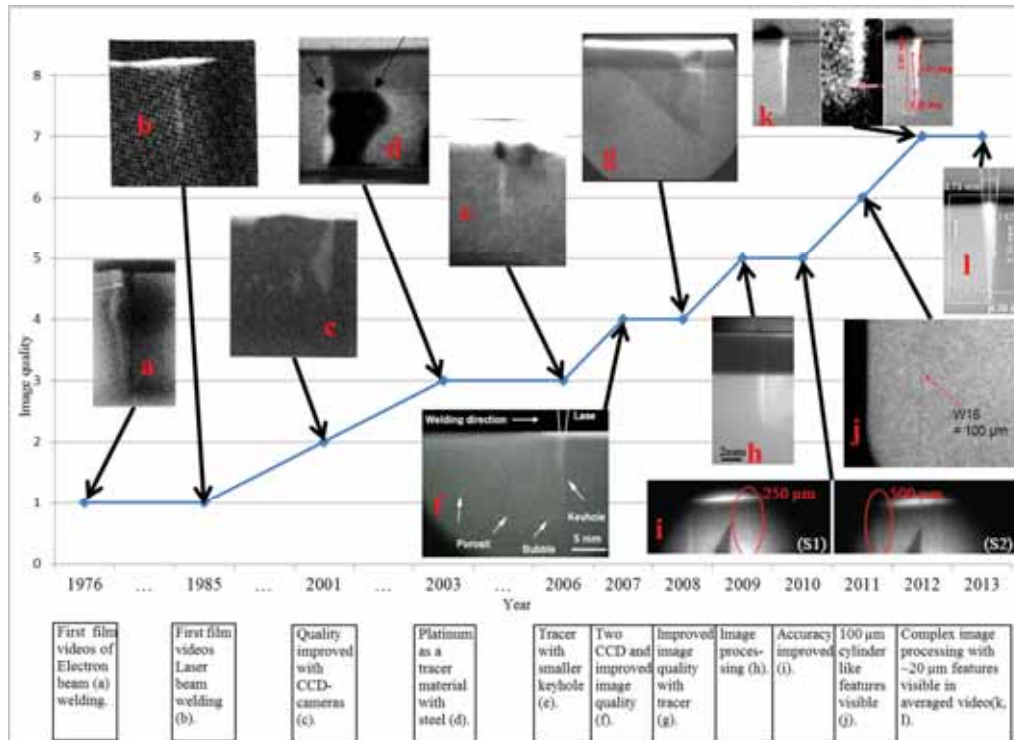


Figure 8. Overview of quality and breakthroughs in x-ray videography of laser welding of steels.

References for the figure above. A larger version of the figure can be found from Appendix 1.

- a. (Arata, Abe & Fujisawa 1976)
- b. (Arata, Abe & Oda 1985)
- c. (Katayama et al. 2001)
- d. (Tsukamoto et al. 2003)
- e. (Kinoshita et al. 2006)
- f. (Katayama, Kawahito & Mizutani 2007)
- g. (Zhang et al. 2008)
- h. (Zhang et al. 2009)
- i. (Abt, Weber & Graf 2010)
- j. (Abt et al. 2011)
- k. (Vänskä et al. 2012)
- l. (Vänskä et al. 2013).

The idea of x-ray videography was likely started by Arata et al. from Osaka University, Japan with interest in how the keyhole acts during deep penetration welding. They studied electron beam welding with the help of x-ray videography. The materials they tested were aluminium

as a base material and silver as the tracer. The purpose of tracer material was to see the molten metal flow inside the molten pool. (Arata, Abe & Fujisawa 1976)

Electron beam (EB) welding has similar features as laser welding. The main difference is that EB welding requires a vacuum chamber, however, it is also possible to weld with a laser in the vacuum. There are several advantages when a vacuum is used, such as elimination of plasma generation above the keyhole. The EB welding can be keyhole welding and x-ray videography was tested with EB first. Figure 9 shows one series of welding process with electron beam and x-ray videography. The material was aluminium with 20 mm width and 50 mm thickness. As can be seen from figure 10, the keyhole is visible and some movement can be seen. The validation of the x-ray videography was performed using EB-welding by Arata and then the technology was transferred to laser welding. (Arata, Abe & Fujisawa 1976)

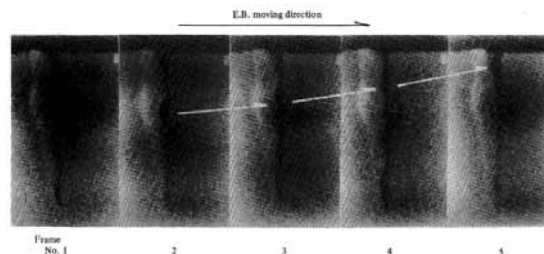


Figure 9. One series of images from Arata et al. experiments, EB-welding. (Arata, Abe & Fujisawa 1976)

The first published x-ray videography tests applied to laser welding were also performed by Arata et al. High power CO₂-lasers were available at that time and first results were published during 1985. The material was mild steel SM41, but they also tested lime-glass welding to observe how the keyhole behaves. The glass tests were filmed with regular high speed camera from the side of the sample. In this case x-ray was not used but the idea was the same, i.e. to observe what happens inside the keyhole. In addition to these experiments, welding of glass has been tested later on by Jin et al. and Li et al. with glass-steel interface and welding of ice and capillary in water by Berger et al. (Jin, Li & Zhang 2002) (Li et al. 2014) (Berger 2011) All of these experiments were performed to study keyhole behaviour in deep penetration laser welding. In the experiments by Arata et al. the laser was 15 kW CO₂-laser and the used power for the welding experiments were 9 and 7.5 kW. Figure 10 shows the setup used. (Arata, Abe & Oda 1985)

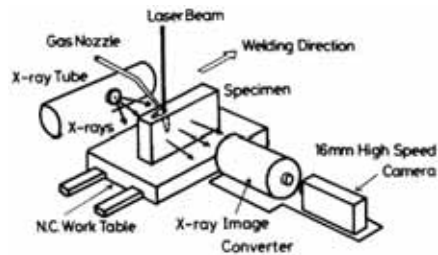


Figure 10. X-ray videography setup for laser welding research, year 1985. (Arata, Abe & Oda 1985)

As shown in figure 11, the keyhole is partly visible but the lower part, the bottom of the keyhole is not really visible in these images. The contrast is mainly sufficient to observe parts of the keyhole and mainly the area near the surface. (Arata, Abe & Oda 1985)

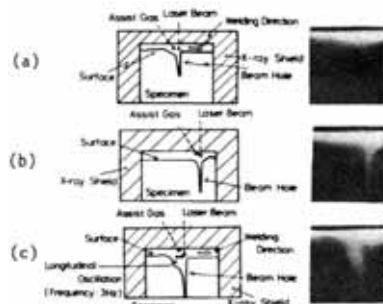


Figure 11. Different processes and x-ray images, a) cw, b) pulsed and c) LSSW. (Arata, Abe & Oda 1985)

2.7 Modern x-ray videography in laser welding

X-ray technology in this field took a leap forward by introducing micro-focused x-ray tubes, which allow a very small focal point diameter, down to μm -range. Using a smaller focal point diameter in the x-ray tube the image quality becomes better due to accurate higher intensity x-ray radiation. The camera technology also has improved in the beginning of 21st century by introducing extremely sensitive and ultra-high speed CCD-cameras that are suitable for this process with a scintillator. Even though the camera requires sufficient amount of light onto the sensor, the micro focused x-ray tubes increases the intensity compared to large focal point x-ray tubes.

Osaka University has had several groups studying the laser welding process. Matsunawa et al. has been one of the laser group leaders and published laser keyhole welding results in 1998 (Matsunawa et al. 1998). Katayama has studied the x-ray videography widely. Results with the emphasis on analysis of pore formation and molten metal flow have been published since 2001, figure 12. (Katayama et al. 2001) (Katayama, Kawahito & Mizutani 2007) The pores were

visible and can help study the pore formation by observing and comparing keyhole upper part and lower part closure times. Kaplan et al. studied keyhole spot welding of steel and to see keyhole behaviour as magnified way with liquid Zn. (Kaplan, Mizutani & Katayama 2002) Yasuaki et al. studied autogenous Nd:YAG-laser welding and also GTA-Nd:YAG-laser-hybrid welding using the x-ray videography. (Yasuaki, Mizutani & Katayama 2003) Kinoshita et al. studied laser welding of a 304 type stainless steel with a 6 kW fiber laser, figure 12. (Kinoshita et al. 2006) Naito et al. studied fiber laser welding and hybrid welding with GTA-process (Gas Tungsten Arc). They used the system in Osaka University and mainly observed molten pool and molten metal flow (Naito, Mizutani & Katayama 2006).

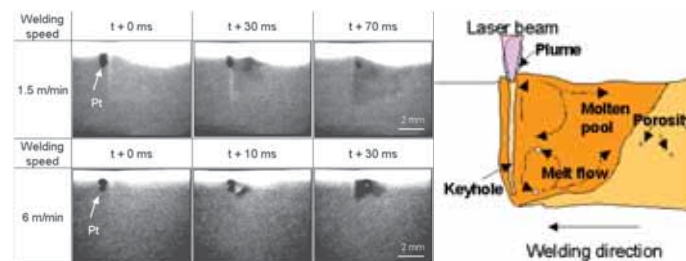


Figure 12. Tracer material in SUS304, which is close to EN 1.4301, and principle of molten metal flow behind the keyhole. (Kinoshita et al. 2006)

Naito et al. showed YAG-laser welding of austenitic stainless steel with the x-ray visualised keyhole. The molten metal flow was visible in their study, but the amount of laser parameters used was limited. (Naito, Mizutani & Katayama 2006). In 2009 Zhang et al. studied laser welding with 10 kW fiber laser and a tracer material. Tracer material was selected with respect to base materials atomic number; in this case the base material was austenitic stainless steel and platinum was the tracer material. Figure 13 shows welds with tracer material. Molten pool is visible, but the molten metal flow of the tracer affects the visible area; in other words if the tracer material flow is not complete throughout the whole molten pool the complete molten pool is not visible with this method. Another main parameter is the welding speed, which affects the weld solidification speed and this also solidification front location. (Zhang et al. 2008) Zhao et al. compared keyhole depth to weld depth and they used image averaging of the x-ray video to achieve better contrast of the keyhole. The material was mild steel and the laser was a 7 kW fiber laser. (Zhao, Tsukamoto & Arakane 2009) Katayama et al. performed welding experiments of EN 1.4301-type stainless steel with a 6 kW fiber laser and x-ray videography system (Katayama & Kawahito 2009). Honda et al. observed keyhole fluctuations with micro focused x-ray (4 μm spot size) videography at 1 kHz frame rate during high power CO₂-laser welding of steels and found out that the molten pool fluctuates behind the keyhole. (Honda et al. 2010)

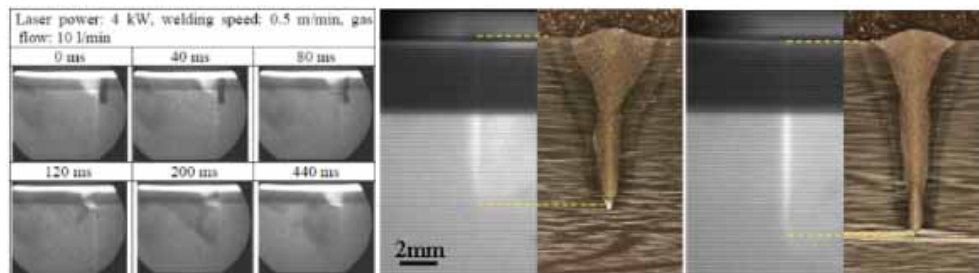


Figure 13. Welds with tracer material on left. Two welds and keyholes on right, x-ray videos processed with averaging. (Zhang et al. 2008) (Zhao, Tsukamoto & Arakane 2009)

At the moment, 2014, there are only two published x-ray videography systems in the world that are built for laser processing research. One of the x-ray systems is in Osaka University in Japan and the other one in Institut für Strahlwerkzeuge (IFSW), University of Stuttgart in Germany. The x-ray system at IFSW is mainly made for laser welding of metals and this has been one of the main design features during the selection of the equipment. The laser that has been mainly used has been a 5 kW disk laser from Trumpf with transport core diameters from 100 to 500 μm , focal point diameters from 50 to 600 μm depending on the optics and focal lengths around 200 to 500 mm. The linear table in the system allows feeding speeds up to 50 m/min. The schematic principle of IFSW x-ray system is shown in figure 14. (Abt, Weber & Graf 2010) (Abt & Boley 2011)



Figure 14. Imaging system in IFSW x-ray station. On the right image 1) scintillator behind a protective case, 2) optics, 3) image intensifier, 4) optics and 5) high speed camera. (Abt, Weber & Graf 2010)

One example image of detectability of wire shape structures behind a 4 mm thick steel plate is shown in figure 15. The smallest wires that are visible are approximately 100 μm in diameter, in these cases the wire is mainly visible but can blend into the background momentarily or partly. The standard test confirmed 160 μm diameter wire visibility. Confirmed circular-hole shape detectability was 125 μm . The detectability depends also on the shape of the structure of the feature. For example, a square shape has a higher detectability due to edges being the same width as the centre, this results in a more even distribution of the x-ray beams in the scintillator. Round and wire like structures have narrow edges in the x-ray beam travel direction so the intensity that penetrates the sample is lower in the edge regions. Wire like shapes also act slightly differently than other shapes; the noise in the image can disturb the wire like shape or

that a wire is only partly visible in the worst case scenario. Figure 15 shows step-hole penetrameter, a pinhole shape structure which has even intensity penetrability along the whole area. (Abt et al. 2012)

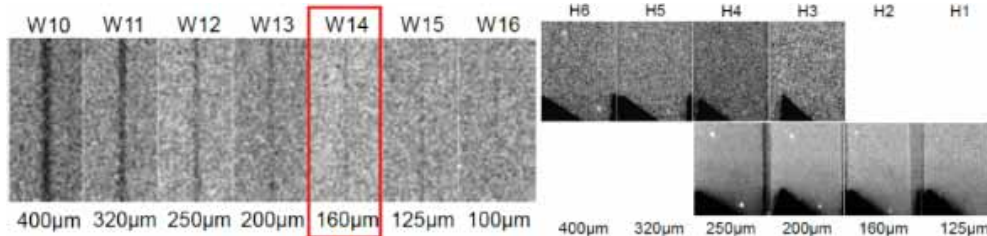


Figure 15. Wire and step-hole penetrameter tests according to standard, IFSW. Step-hole penetrameter tests on the right, upper images with 1 ms exposure time and lower with 200 ms. (Abt et al. 2012)

Abt et al. has performed standard x-ray tests with the imaging system at IFSW laser laboratory's equipment. In the figure above, a wire is behind a 4 mm steel plate taken with 1000 frames per second (fps) at IFSW according to wire penetrameter test. The step-hole penetrameter test included 1 ms exposure time, upper right in previous figure, and also 200 ms exposure time tests, lower right. Testing was performed according to EN standards, wire penetrameter and step-hole penetrameter tests. (EN-Standard 1994) (EN-Standard 1994) (Abt et al. 2012)

Another example is using a tracer material, for example tungsten powder with aluminium as base material, figure 16. The tracer allows observing molten metal flow inside the molten pool. One problem in this arrangement can be that the tracer affects penetration momentarily and when the penetration returns to normal there are less tracer material in the molten pool. It is also possible to use copper as base material and study keyhole behaviour and geometry. On the other hand the keyhole stabilises relatively quickly after the spiking due to tracer. The main interest is the molten metal flow pattern after the spiking when there is still some tracer material present. Also in the next figure a bubble shaped keyhole is shown, the keyhole forms a large vapour bubble below the surface and disturbs the process overall. This forms a special droplet shape weld. (Abt et al. 2011) (Heß 2012)

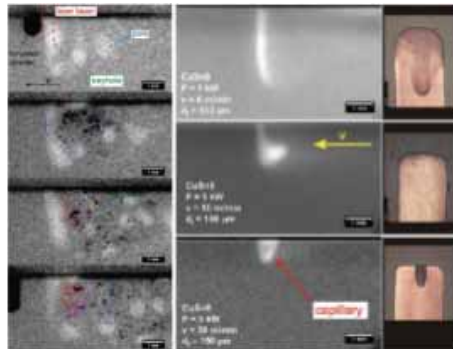


Figure 16. Tracer test with aluminium and tungsten powder and copper welding on right. (Abt et al. 2011) (Heß 2012)

In a previous publication by Vänskä et al., 2012, the differences between bead on plate and butt joints in laser welding of stainless steel were discussed. Two different joint types were used; bead on plate and laser cut I-butt joints. The penetration was considerably deeper for butt joints, but there was a small bevel on the top part of the joint that was caused by the cutting process. The sample preparation method, laser cutting, produced a small bevel on the top of the sample and it affected the welding process. The bevel was approximately the same as depth increase in some cases, but the welds were not underfilled. (Vänskä et al. 2012)

Boley et al. studied how to reconstruct a keyhole and a molten pool geometry together, this resulted in a combined keyhole and molten pool 3D-model. They used tracer material to track the solidification line of the molten pool. The materials were aluminium and steel. A 5 kW disk laser was used for the welding experiments. One method was a simple frame model to achieve a 3D-model of the molten pool, shown in figure 17. These also have some assumptions to form the molten pool geometry, for example the geometry of the molten pool in front and on the side of the keyhole. (Boley et al. 2013)

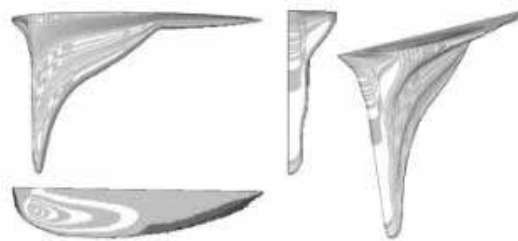


Figure 17. Simple frame model to reconstruct molten pool and keyhole combined. (Boley et al. 2013)

2.8 Conclusions of previous studies

To conclude the previous studies of this area, x-ray videography has been used widely with several materials and welding processes. The main problem has been the very limited laser parameter range, a complete study of the effects of joint and laser parameters has not been conducted until now. In several studies molten pool size and behaviour has been visible but these have not been connected with the keyhole geometry and no definitions of multiple types of keyholes have been presented. This study defines these keyhole modes and connects the modes to laser parameters and to molten pool behaviour. The laser type affects the keyhole welding process in many ways and the fastest increasing laser type to date is modern solid state laser, mainly the fiber laser. There have been x-ray videography results published of CO₂-laser welding and the x-ray parameters were mainly considered and to present different means of achieving keyhole welding process. With this laser type a small focal point size can be achieved with high brightness and is well usable for many different materials with keyhole welding process.

2.9 Image processing

Digital image processing is used in all digital radiography applications to improve image quality and especially detectability of different types of structures. The processing has a great influence on how the image appears in the analysis. Pathology uses digital processing with digital radiography to see different areas or types of structures in more detail. Several different masks, filters, filtering processes and enhancements are used for this purpose. (Prokop & Schaefer-Prokop 1997) (Körner et al. 2007)

Image processing is of crucial importance in x-ray imaging. The raw image might be complicated to read in certain cases. Different image processing methods are used, depending on the application. The image processing program variety is relatively large and all of them have their own highlights. There are several different methods of processing images and the type of structures or features in the image in interest mainly specifies the processing method.

The digital processing helps greatly in the analysis. This is the reason why image processing is widely used in radiography. The similar methods are also used in x-ray videography, but with few additions, for example multi-image processing, video processing, such as averaging and Kalman stack filtering. Digital image processing in laser welding research can benefit from contrast enhancement and adjustment, shading, sharpen masks, find edges with single images and for videos Kalman stack filter, average intensity, standard deviation and minimum and maximum intensities. The most common processes are contrast adjustment, shading, Kalman stack filter, standard deviation and average intensity.

Shading is very important in video processing due to scintillator build and possible defects in the optics, possible shielding plate defects and uneven x-ray dose from the x-ray tube; these are

called stable defects. These stable defects are visible in all experiments, except that there can be more spatters on the protection plate the more welds are performed if protection plate is not cleaned or changed. Shading means that first an x-ray video is taken from an unwelded part of a plate of similar material and thickness. Then an average image is calculated from this video. After this the welding process is filmed and this video is divided by the average shading image. This removes all system flaws and only the process is left in the video. The main limiting factor when selecting an image processing program for shading calculations is the memory capability of the program and the computer, due to large use of memory during the process, and that the program must be able to handle 32-bit images. A shading example is shown in figure 18. The scintillator is made of hexagonal structures which can be visible in average images of the videos. This structure causes more “noise” in single frames and short video averages.

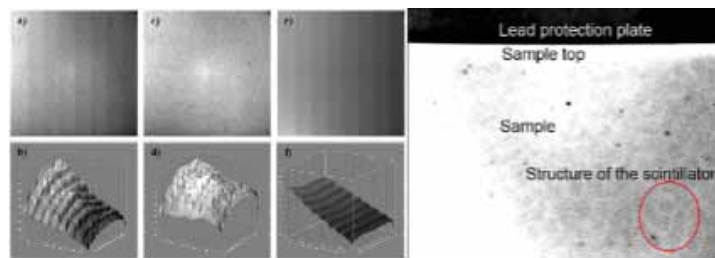


Figure 18. Shading example. (Abt et al. 2011)

In the figure 19 a principle of the shading process is shown, also the images according to corresponding phases. a) raw image of step wedge, b) grey level distribution of the raw image, c) shading average of homogenous even object, d) grey level distribution of even object, e) corrected image of the step wedge and f) grey level distribution. Usually the x-ray tube has uneven intensity distribution, which is also shown. (Abt et al. 2011)

2.10 Keyhole modelling and calculations

The keyhole modelling and welding simulation is very interesting topic and might save time and resources if used properly in industry. The main goal is to test welding parameters and achieve visual results about the formation of the keyhole, its behaviour and the weld geometry. According to the simulations of Courtois et al. the keyhole wall temperature is between 2 700 and 3 500 K with 4 kW laser power and 6 m/min welding speed. The temperature is mainly above the boiling temperature of the steel and all main alloying elements, which is approximately 3 000 K. (Courtois et al. 2014) (Courtois et al. 2014) According to Rai's simulations with 304L stainless steel the temperature in the keyhole wall is 3 100 K when using a 1 kW laser power (CO₂-laser) and welding speed of 1.14 m/min. This temperature is approximately the same as ferrite's, chromium's and nickel's boiling temperature. The comparison of the simulation and welding experiment had significant difference, the welding

experiment showed larger weld pool. Rai used also laser powers of 5 kW and 9.6 kW and the temperature in the keyhole wall was 3 100 K as with lower laser power. (Rai 2008)

The temperature of the plasma, on the other hand, might cause elevated temperature in the keyhole wall. According to Dowden, the experiments with CO₂-laser of measuring the plasma temperature during laser keyhole welding resulted in the range of 5 000 to 18 000 K, which is approximately 4 730 to 17 730 °C. This might have a significant effect on the keyhole wall and on the surface behaviour of the molten pool. In this case the photon wavelength was longer, 10 600 nm, than in the other studies, 1 064 nm, with 1 064 nm wavelength the plasma absorption is significantly smaller. (Dowden 2001) According to Weldingh et al. the plasma formation is connected to heating of the material and so the evaporation of the atoms, thermal electron emission (heated electrons or ions carrying energy) and avalanche plasma ionisation (charged electrons ionising material). This would point out that there could be plasma even without a direct laser photon – electron ionisation. (Weldingh & Kristensen 2001) There have been suggestions that the keyhole has a circular or a rotation symmetric shape. This seems to be valid for low welding speeds, approximately 1 to 6 m/min, this range is also valid for the Rosenthal regime. (Eriksson, Powell & Kaplan 2013) (Daneshkhah, Najafi & Torabian 2012) (Dowden et al. 1987) (Matsunawa & Semak 1996) (Volpp 2012) (Fabbro 2010)

There have been several publications of simulations of the keyhole in laser deep penetration welding. The main problem in most cases that some assumptions must be made. There are also several ways to perform simulation of heat transfer in laser welding. Keyhole acts very dynamically and the exact prediction is very complicated. Most of the keyhole models use assumptions, for example simplified keyhole to study 2D-molten metal flow in the molten pool.

Daneshkhah et al. used a volumetric heat object to simulate the weld geometry. The simulation of the weld during the laser welding was close to actual weld geometry from the welding experiments. The temperature was approximately 3 300 K in the keyhole region. The keyhole was relatively shallow and depth to width ratio was only approximately 3. The material was EN 1.4301 stainless steel, laser power 2.5 kW (Nd:YAG), welding speed of 3 m/min and 200 µm focal point diameter. (Daneshkhah, Najafi & Torabian 2012)

Berger and Hügel calculated fluid dynamic effects in keyhole welding in which they considered different keyhole shapes, such as circular and elongated. They came to a conclusion that three different keyhole regimes exists concerning pressure balance in the keyhole. The regimes were circular keyhole, or circular shape, dynamic keyhole, or self-adapting elongated shape or absorbing front, or no keyhole. The dynamic, elongated keyhole can be unstable according to their results. (Berger & Hügel 2013)

2.11 Mass attenuation coefficient

The x-ray imaging and videography is based on the penetrability and scattering of high energy photons in material. Short wavelength electro-magnetic radiation which has a high photon energy penetrates the material in much larger quantities than wavelengths in and near the visible range. In this range also scattering happens in addition to penetration and this radiation can be detected by using suitable materials, such as cerium activated boron silicates. (Leo 1987) The most common uses for x-rays are in medical field with imaging of bones and in material technology imaging metallic weld's defects. Using of the tracer material with the x-ray during the welding process allows tracking of the molten metal movements due to visibility of the tracer in the x-ray videos. The contrast difference is based on the mass attenuation difference between the base and the tracer material. The higher the attenuation is, the more it absorbs the photons per unit mass and thickness. When comparing iron to chromium and nickel, which are the main alloying elements in stainless steels, the difference is very small and the total x-ray attenuation is very similar. This is one reason why stainless steel alloying elements are not visible in the x-ray videos and images unlike higher atomic number elements that are used for tracing, such as tungsten or molybdenum in sufficient amounts. Molybdenum is an alloying elements of some stainless steels but the weight percentage is relatively small compared to that when using a 99.9 % molybdenum as a tracer wire. Complete explanation of the mass attenuation coefficient can be found from appendix 24.

3 Experimental Methods

All of the research and analysis methods used in this work are described in this chapter. The work was divided into several sections and results were mainly analysed separately. Some of the analyses were performed in combination with others and some examples of the used methods are presented in more detail, image processing in appendix 21.

3.1 Flow chart of the experiments

A flow chart of the experimental procedure is in figure 19, which shows all of the practical test phases. The flow chart is presented to provide a clear idea of the experimental part of the work step by step.

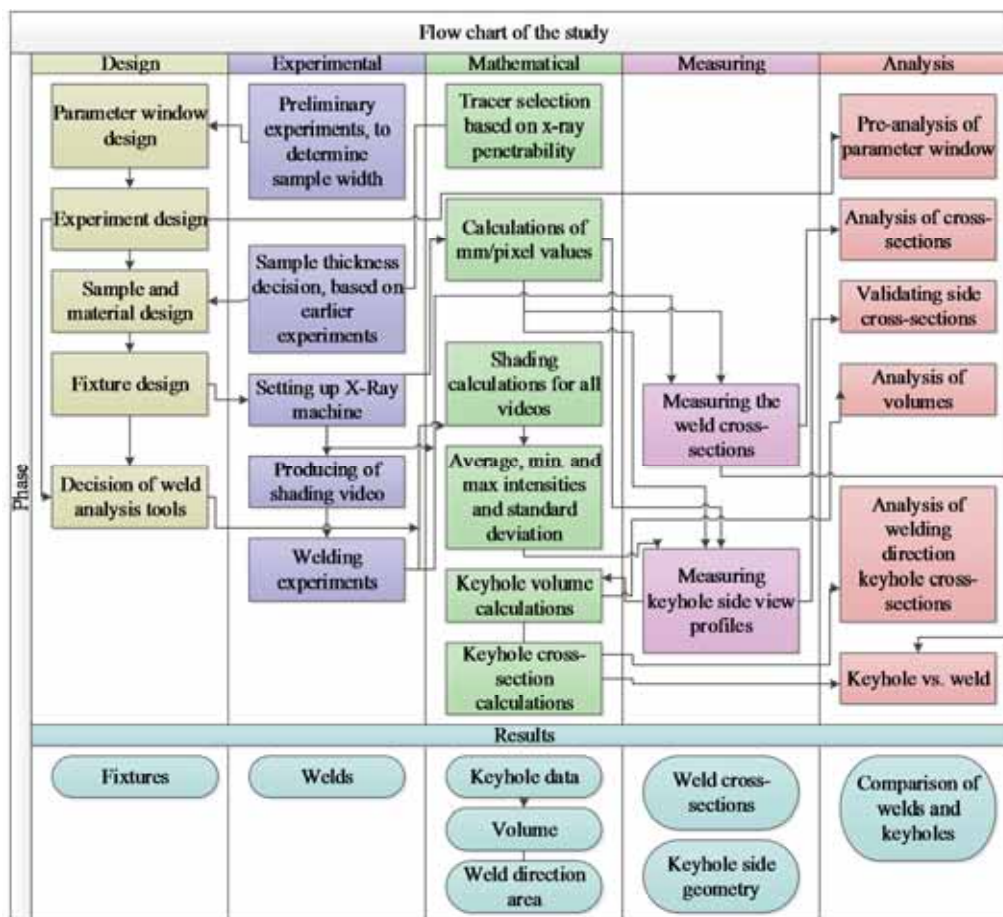


Figure 19. Flow chart of the experiments.

3.2 Materials

Austenitic stainless steel is the largest of the general groups of stainless steels and is the most produced type. This type of steel was selected as the test material due to its usefulness, universality and good weldability with lasers and common use in several processing industries, such as oil and gas refineries and pulp, paper and chemical industries. The main alloying elements of the austenitic stainless steel are chromium and nickel. Chromium contributes to corrosion resistance and ferrite formation, but nickel on the other hand strongly promotes austenite formation as the material solidifies. In table 1 the alloying elements are shown for EN 1.4404 and EN 1.4301 austenitic stainless steels.

Table 1. Alloying elements of two stainless steels used in the experiments.

EN code	ASTM	C	Cr	Ni	Mo
1.4301	304	0.02	18.1	8.1	
1.4404	316L	0.02	17.2	10.1	2.1

3.3 Joint types

The joint geometries used were designed to give two different points of comparison, a bead on plate (BOP), which is to give a rough estimate of a precisely machined edge and a common laser cut I-butt joint (IBJ). The sample thicknesses used in this study were 4.9 and 7.8 mm. The manufacturer defines these plates as 5 and 8 mm in thickness, but the actual thickness was slightly smaller. The actual plate thicknesses were used in all graphs and calculations. All welding parameters were used for all joint types and plate thicknesses.

A machined edge can be very precise, which is at the best cases close to bead on plate welding. Figure 20 shows an example of both thicknesses with laser cut I-butt joints. The bead on plate had same width and the thickness as the butt joints except there was no bevel, all of same thickness samples were cut from one plate and due to that there were no material mixture differences. In addition 40 mm thick samples were used as bead on plate experiments. This was due to easy setup for determining the optimal x-ray parameters and also for some of the tracer experiments.

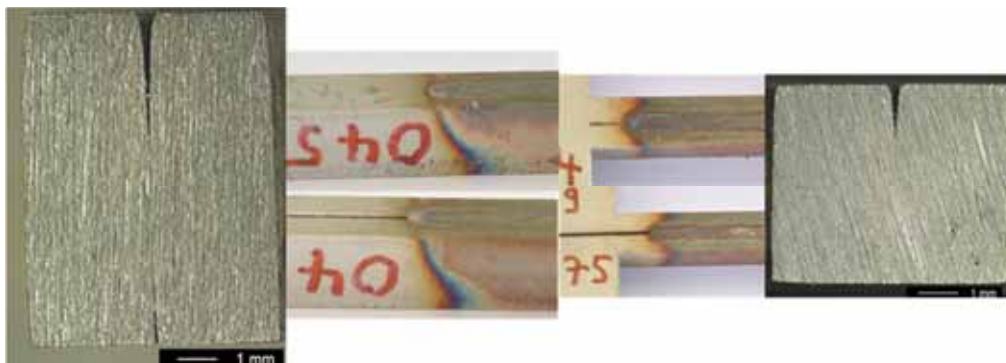


Figure 20. Joint types used in the experiments. The cross-sections of the joints are in the same scale.

The samples were cut with a CO₂-laser and the bevel on the upper part was formed during the cutting process. The average bevel areas were -0.3 and -0.2 mm² with 7.8 and 4.9 mm thick samples respectively. The bevel does affect the keyhole penetration and the filling capability, but it is a common result from several joint manufacturing methods.

Sample width was selected with the usable x-ray intensity to have sufficient x-ray dose on the scintillator. The sample thickness was selected to achieve full penetration and also partial penetration welds, but not to have extremely thick plates thus the cutting quality remains the same.

3.4 Equipment

3.4.1 Laser

The laser was a disk laser, TruDisk 5001, having a maximum laser power output of 5.0 kW. The optical transport fibre diameter was 200 μm . The collimation optics had 200 mm collimation length. The welding head was a Trumpf BEO-D70 with 280 mm focal length lens. All of the experiments were performed with the same laser equipment. The optics resulted in 2.0 mm Rayleigh length and calculated focal point diameter of 280 μm . The focal point diameter and the area at the sample surface was also calculated for each focal point position (FPP). The average intensity was calculated according to used laser power and focal point diameter (FPD), shown in Table 2.

Table 2. FPPs, FPDs, beam areas and its average intensity on the surface.

FPP [mm]	FPD [μm]	Beam area on the surface [mm^2]	AVE intensity [W/mm^2]
+2.0	420	0.14	$3.61 \cdot 10^4$
± 0.0	280	0.06	$8.12 \cdot 10^4$
-2.0	420	0.14	$3.61 \cdot 10^4$
-4.0	560	0.25	$2.03 \cdot 10^4$
-5.0	640	0.32	$1.55 \cdot 10^4$
-6.0	710	0.40	$1.26 \cdot 10^4$

3.4.2 X-ray

Both high power and micro focus modes were tested during the experiments, with high power mode the acceleration voltage, the potential, was 140 kV with 1 284 mA and with micro focus mode 140 kV with 642 mA. Most of the tests were with the high power mode.

3.4.3 Cameras

The top side camera was at 60 degree angle to the sample surface and the illumination laser was below it, in 45 degree angle to the sample surface. For the tracer experiments the setup of top camera was coaxial (with the laser beam) and the illumination laser was in 45 degree angle to the sample surface. The wave mode for the illumination laser was continuous wave and the camera had a narrow band pass filter letting mainly only the illumination laser wavelength pass through. Top side camera was filming with 5 000 frames per second (fps) and x-ray camera 500 fps.

3.4.4 Other equipment

As a plasma control and shielding gas helium was used mainly to suppress possible plasma and intense metal vapour formation and as a secondary purpose to act as a shielding gas with a flow rate of 25 l/min. The set-up also had a fume extraction system to eliminate the hazardous chromium and molybdenum fumes. All equipment was protected with protection plates and – windows. Figure 21 shows the welding setup and a closer principle image of the equipment positions for 7.8 mm samples. Due to the narrow samples the heat does not dissipate effectively away from the solidified weld and due to this the oxidation of the surface is probable. The heat dissipation into the fixture was not calculated or estimated and the most of the heat stays in and near the process and especially the weld. The hot cracking phenomena was considered, but the x-ray system has limitations and the x-ray limitations was taken as a priority and excessive heat as a secondary issue.

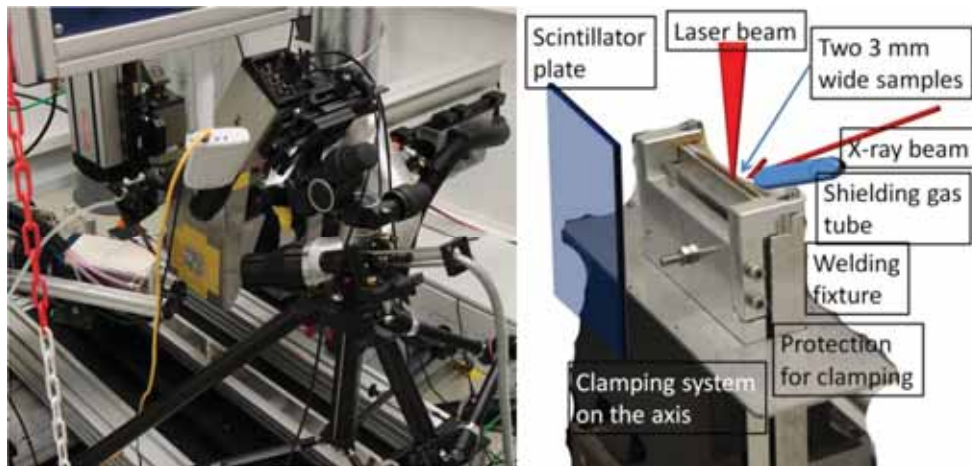


Figure 21. Welding setup on the left and principle image of the beam locations on the right.

New types of fixtures were designed to use the full potential of the x-ray system with as thick sample as possible to minimize the effect of excessive heating of the samples. In figure 22 two designed fixtures are shown for 7.8 and 4.9 mm sample thicknesses. The 7.8 mm sample fixture is designed to act as a large plate so the heat dissipates into the fixture below. The 4.9 mm sample fixture has heat dissipation from the large area sample ends from which the heat dissipates into the fixture. The welding length was 80.0 mm for 7.8 mm thick samples and 40.0 mm with 4.9 mm thick samples.

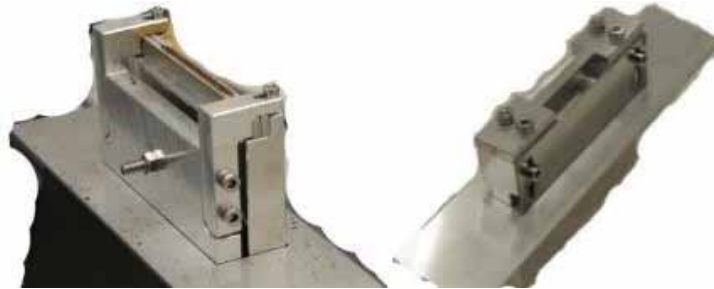


Figure 22. Fixtures for different joint types, left partial penetration and right full penetration.

The positioning of the sample in the x-ray system caused a misalignment of the x-ray tube and the sample top, shown in figure 23. Due to this the sample top is shown as an area with several “edges” in the x-ray videos. The actual keyhole location can be calculated and measured from the images and videos.

The most common way of positioning the x-ray tube to the sample is to align the sample top with the middle point of the x-ray emitter to achieve an accurate sample top. This was not possible due to small imaging area and deep keyhole. The sample location was measured from the x-ray videos.

The system had several lead protection plates to prevent excessive x-ray dose on the scintillator if for example the sample starts to bend and gets further away from the fixture forming a gap and causes the x-ray beam to pass through to the scintillator without sample or fixture attenuation. The scintillator is very sensitive and can even break if exposed to excessive x-ray radiation. Similar, but smaller, misalignment was present in the full penetration welding, and the actual sample root was measured from the x-ray videos.

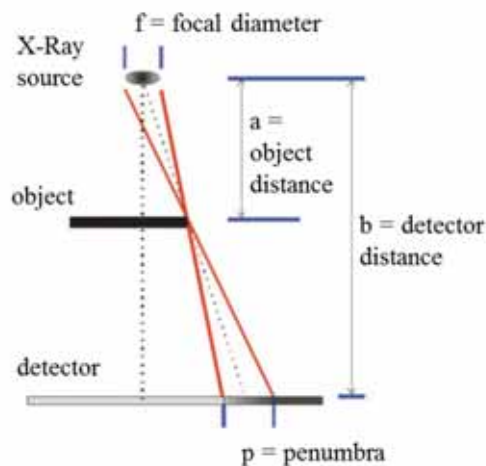


Figure 23. Multiline sample top. Alignment with partial penetration samples. The full penetration sample alignment was similar.

3.5 Parameter variables

Welding parameter set was designed to give results from a large parameter window and with multiple joint configurations. One variable at a time (OVAT) method was used, in which it is possible to examine the effect of one parameter at a time. In this manner it is possible to study the connections between different parameters, e.g. whether one parameter has similar effects on the process behaviour compared to another parameter. In addition, each weld can be studied separately and then compared to other combinations. Both thicknesses and joint types were welded with all parameter combinations. All welding parameters are presented in table 3. The four welds marked as “error” were false welds and no results of those welds were possible to acquire.

Table 3. Welding parameter table.

PARTIAL PENETRATION Joint type	Weldin g speed [m/min]	Focal point position	PARTIAL PENETRATION Joint type	Weldin g speed [m/min]	Focal point position	FULL PENETRATION Joint type	Weldin g speed [m/min]	Focal point position	FULL PENETRATION Joint type	Weldin g speed [m/min]	Focal point position
Bead on plate	5	2	I-butt joint	5	2	Bead on plate	5	2	I-butt joint	5	2
Bead on plate	5	0	I-butt joint	5	0	Bead on plate	5	0	I-butt joint	5	0
Bead on plate	5	-2	I-butt joint	5	-2	Bead on plate	5	-2	I-butt joint	5	-2
Bead on plate	5	-4	I-butt joint	5	-4	Bead on plate	5	-4	I-butt joint	5	-4
Bead on plate	5	-5	I-butt joint	5	-5	Bead on plate	5	-5	I-butt joint	5	-5
Bead on plate	5	-6	I-butt joint	5	-6	Bead on plate	5	-6	I-butt joint	5	-6
Bead on plate	4	2	I-butt joint	4	2	Bead on plate	4	2	I-butt joint	4	2
Bead on plate	4	0	I-butt joint	4	0	Bead on plate	4	0	I-butt joint	4	0
Bead on plate	4	-2	I-butt joint	4	-2	Bead on plate	4	-2	I-butt joint	4	-2
Bead on plate	4	-4	I-butt joint	4	-4	Bead on plate	4	-4	I-butt joint	4	-4
Bead on plate	4	-5	I-butt joint	4	-5	Bead on plate	4	-5	I-butt joint	4	-5
Bead on plate	4	-6	I-butt joint	4	-6	Bead on plate	4	-6	I-butt joint	4	-6
Bead on plate	3	2	I-butt joint	3	2	Bead on plate	3	2	I-butt joint	3	2
Bead on plate	3	0	I-butt joint	3	0	Bead on plate	3	0	I-butt joint	3	0
Bead on plate	3	-2	I-butt joint	3	-2	Bead on plate	3	-2	I-butt joint	3	-2
Bead on plate	3	-4	I-butt joint	3	-4	Bead on plate	3	-4	I-butt joint	3	-4
Bead on plate	3	-5	I-butt joint	3	-5	Bead on plate	3	-5	I-butt joint	3	-5
Bead on plate	3	-6	I-butt joint	3	-6	Bead on plate	3	-6	I-butt joint	3	-6
Bead on plate	2	2	I-butt joint	2	2	Bead on plate	2	2	I-butt joint	2	2
Bead on plate	2	0	I-butt joint	2	0	Bead on plate	2	0	I-butt joint	2	0
Bead on plate	2	-2	I-butt joint	2	-2	Bead on plate	2	-2	I-butt joint	2	-2
Bead on plate	2	-4	I-butt joint	2	-4	Bead on plate	2	-4	I-butt joint	2	-4
Bead on plate	2	-5	I-butt joint	2	-5	Bead on plate	2	-5	I-butt joint	2	-5
Bead on plate	2	-6	I-butt joint	2	-6	Bead on plate	2	-6	I-butt joint	2	-6
Bead on plate	1.5	2	I-butt joint	1.5	2	Bead on plate	1.5	2	I-butt joint	1.5	2
Bead on plate	Error		I-butt joint	Error		Bead on plate	1.5	0	I-butt joint	1.5	0
Bead on plate	1.5	-2	I-butt joint	1.5	-2	Bead on plate	1.5	-2	I-butt joint	1.5	-2
Bead on plate	1.5	-4	I-butt joint	1.5	-4	Bead on plate	1.5	-4	I-butt joint	1.5	-4
Bead on plate	1.5	-5	I-butt joint	1.5	-5	Bead on plate	1.5	-5	I-butt joint	1.5	-5
Bead on plate	1.5	-6	I-butt joint	1.5	-6	Bead on plate	1.5	-6	I-butt joint	1.5	-6
Bead on plate	1.1	2	I-butt joint	1.1	2	Bead on plate	1.1	2	I-butt joint	1.1	2
Bead on plate	Error		I-butt joint	Error		Bead on plate	1.1	0	I-butt joint	1.1	0
Bead on plate	1.1	-2	I-butt joint	1.1	-2	Bead on plate	1.1	-2	I-butt joint	1.1	-2
Bead on plate	1.1	-4	I-butt joint	1.1	-4	Bead on plate	1.1	-4	I-butt joint	1.1	-4
Bead on plate	1.1	-5	I-butt joint	1.1	-5	Bead on plate	1.1	-5	I-butt joint	1.1	-5
Bead on plate	1.1	-6	I-butt joint	1.1	-6	Bead on plate	1.1	-6	I-butt joint	1.1	-6

3.5.1 Welding speeds

The tested welding speeds were 1.1, 1.5, 2.0, 3.0, 4.0 and 5.0 m/min. The minimum welding speed, 1.1 m/min, was selected due to edge melting caused to the narrow sample when a slower speed was used. This means that the molten pool reaches the sample edge, which gives false results when examining the weld geometry from cross-sections. The maximum welding speed was used due to minimum sample thickness which was 4.9 mm and that the laser power was 5.0 kW in all tests according to the maximum usable laser power.

3.5.2 Focal point positions

The used focal point positions (FPP) were +2.0, surface (± 0.0), -2.0, -4.0, -5.0 and -6.0 mm. Minus sign FPPs were below the sample surface. Rayleigh length was 2.0 mm with the used optics and 2.0 mm focal point position (FPP) steps was selected due to Rayleigh length. Due to significant process behaviour change between -4.0 and -6.0 mm; one middle step was added and that was decided during the welding experiments.

3.5.3 Laser power

The laser power was kept constant at 5.0 kW in all tests, including all of the tracer experiments also. This was the maximum usable output laser power of the used laser, Trumpf TruDisk 5001.

3.5.4 Materials

Two types of austenitic stainless steels were selected and these were EN 1.4404 in all tests and EN 1.4301 with tracer tests and in pre-experiments to achieve optimal x-ray parameters. Selection of the material, stainless steel, was according to previous experiments and collaborations with stainless steel industry. Austenitic stainless steels EN 1.4404 and EN 1.4301 were selected due to easy acquire of the type and common use in several industry fields.

3.5.5 Sample thicknesses

Sample thicknesses of 4.9 and 7.8 mm were selected according to available maximum laser power, which was 5.0 kW, which would be sufficient to penetrate 4.9 mm thick steel plate and have partial penetration with 7.8 mm samples. 40 mm sample thickness (EN 1.4301) was also tested for testing the x-ray system to achieve optimal x-ray parameters and also for tracer experiments. This was performed due to simplicity of the setup with 40 mm thick samples.

3.5.6 Joint types

Two different joint types – bead on plate and I-butt joint – were used for both sample thicknesses. This resulted in four different joint configurations for all laser parameter combinations.

3.6 Tracer experiment parameters

The parameters for the tracer experiments are shown in table 4. These were selected after the welding sets were completed, consisting of four different joint geometries. The selection based on the visual examination and sufficient penetration with all sample types. The laser power was 5.0 kW and all optics were the same for every test set.

Table 4. Tracer experiment parameters, plate thickness 40.0 mm was EN 1.4301, BOP and BJ means Bead on Plate and I-Butt joint, respectively.

Weld number	Plate thickness [mm]	Joint type	Tracer type	Focal point position [mm]	Material [EN standard]	Welding speed [m/min]
1	40.0	BOP	Wire, Mo	-4.0	1.4301	2.0
2	40.0	BOP	Wire, Mo	-4.0	1.4301	2.0
3	40.0	BOP	Wire, Mo	-4.0	1.4301	2.0
4	40.0	BOP	Wire, Mo	-4.0	1.4301	2.0
5	40.0	BOP	Wire, Mo	-4.0	1.4301	1.0
6	40.0	BOP	Wire, Mo	-4.0	1.4301	1.0
7	40.0	BOP	Powder, W	-4.0	1.4301	2.0
8	40.0	BOP	Powder, W	-4.0	1.4301	4.0
9	7.8	BOP	Powder, W	-4.0	1.4404	2.0
10	7.8	BOP	Powder, W	-4.0	1.4404	2.0
11	7.8	IBJ	Wire, Mo	-4.0	1.4404	2.0
12	7.8	IBJ	Powder, W	-4.0	1.4404	2.0
13	7.8	IBJ	Wire, Mo	-4.0	1.4404	2.0
14	7.8	BOP	Powder, W	-4.0	1.4404	4.0
15	7.8	IBJ	Powder, W	-4.0	1.4404	4.0
16	4.9	IBJ	Powder, W	-4.0	1.4404	2.0
17	4.9	BOP	Powder, W	-4.0	1.4404	2.0

3.7 Visual weld evaluation

Weld quality evaluation was performed visually and from the macrographs according to EN-standard 13919-1. The main issues were cracks, lack of fusion, linear misalignment and incompletely filled groove, not in an order of importance or occurrence. Table 5 shows a list, and maximum values, for each main defect and for each quality level. Pores were roughly evaluated, if any were found, from the x-ray videos mainly for movement pattern and flow path, but not measured or counted.

Table 5. Quality levels by EN-standard 13919-1. (EN-Standard 1996)

Quality level	Stringent B	Intermediate C	Moderate D	Stringent B	Intermediate C	Moderate D
Plate Thickness [mm]	5.0	5.0	5.0	8.0	8.0	8.0
Defect type, values [mm]						
Cracks	Not permitted	Not permitted	Not permitted	Not permitted	Not permitted	Not permitted
Crater cracks	Not permitted	Not permitted	Local permitted	Not permitted	Not permitted	Local permitted
Pores	1.5	2.0	2.5	2.0	3.0	4.0
Distance between pores	2.5	2.5	1.3	4.0	4.0	2.0
Lack of fusion	Not permitted	Not permitted	1	Not permitted	Not permitted	1.0
Incomplete penetration	Not permitted	Not permitted	0.75	Not permitted	Not permitted	1.0
Undercut	0.5	0.5	1.0	0.5	0.5	1.0
Excessive bead	1.0	1.2	1.7	1.4	1.8	2.6
Excessive penetration, EP	1.0	1.2	1.7	1.4	1.8	2.6
Linear misalignment	0.5	0.8	1.3	0.8	1.2	2.0
Sagging	1.0	1.0	1.0	1.6	1.6	1.6
Incompletely filled groove	0.5	0.5	1.0	0.5	0.5	1.0
Spatter	Depends on application (spatter material is assumed to be identical to base material).					

3.8 Image processing

Figure 24 shows a simplified overview of the image processing phases. It also has a representation of image quality, meaning the visibility of features in general. Several methods were used to improve the quality of the images and videos during the image processing phase. Automatic calculations were mainly used to achieve the results, such as averaging and Kalman filtering. Different steps improves different areas on the image, minimum values helps to identify bubble flow path and average values results in most accurate image of average keyhole geometry. Kalman filtering was mainly used to track single bubbles in the melt and the molten metal movements. With Kalman filtering the time resolution is reduced slightly, but the visibility of the features increases, especially flow movement directions.

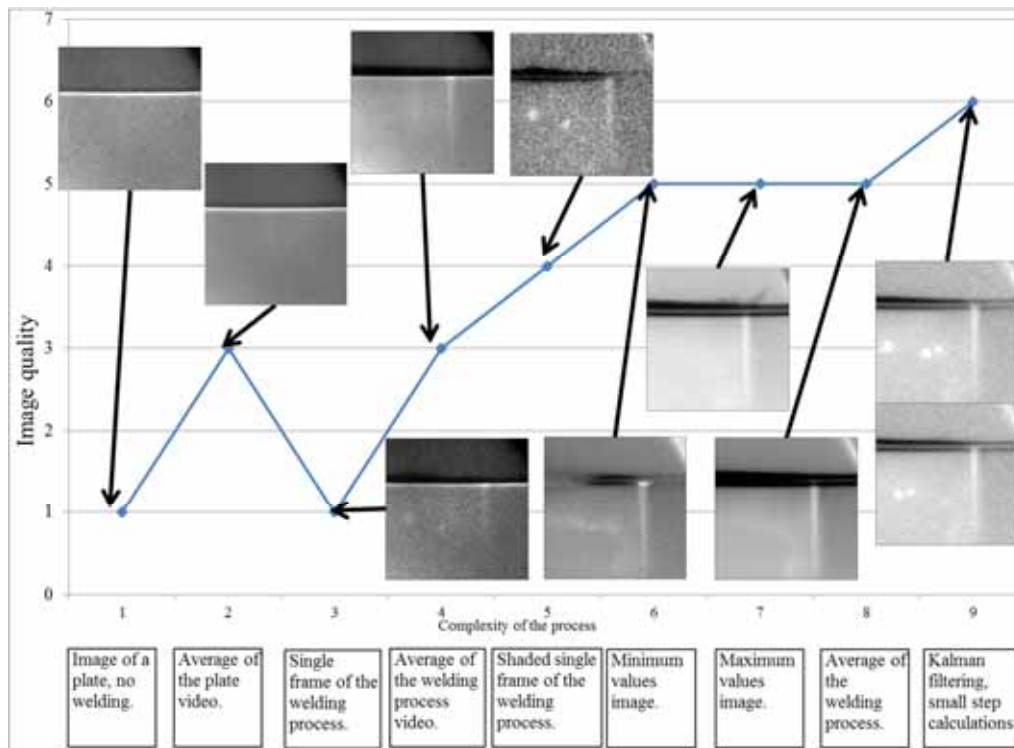


Figure 24. Overview of the image processing procedure of the x-ray videos.

Figure 25 shows a flow chart of the image processing. All mathematical parts were done with complete equations in the image processing program itself. The processing part consists of separate methods in addition to calculations, or taking photographs of the weld cross-sections. Appendix 25 presents a detailed explanation and examples of the image processing phases.

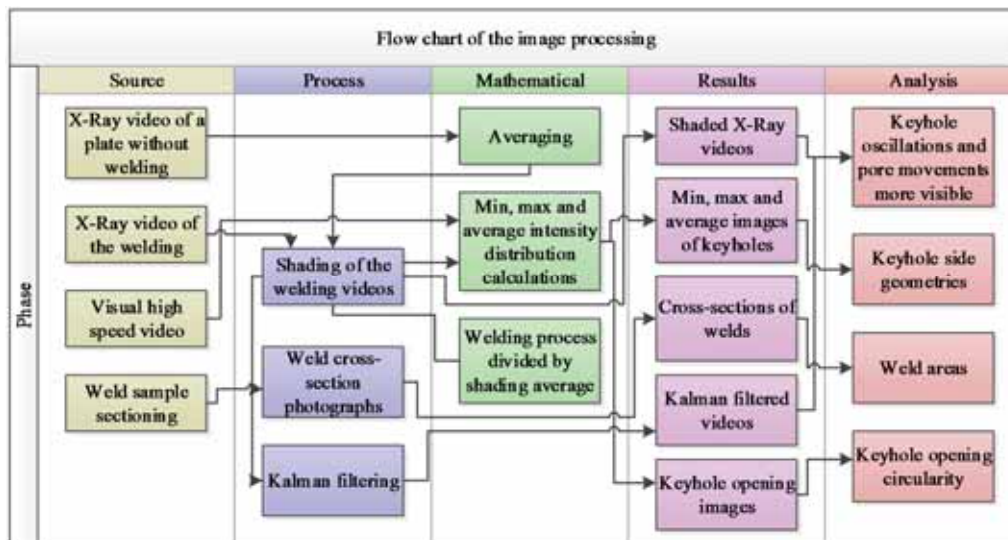


Figure 25. Flow chart of the image processing.

3.9 Sample top side high speed video processing methods

High speed videos were visually analysed, including checking of keyhole closures and circularity of the keyhole opening. The total keyhole volume was calculated in accordance to several measurements and one critical assumption was that the keyhole depth cross-section is circular. Another method was tested, and vapour volume results presented, so that the keyhole depth cross-section was the same as the geometry of the keyhole opening.

In the first test a circle or an ellipse was drawn on the edges of the keyhole and then checked for errors in the geometry. The ratio between longitudinal and transverse distances were measured and then transferred to the keyhole volume calculations. Figure 26 shows four frames 200 ms from each other from a random location along the stable welding and standard deviation, average, median and minimum intensity images. Also maximum intensity values image was used in the analysis. Standard deviation means variations from the average. Average means average intensity values of each pixel in a certain location through the whole video. Median is the middle value of all values, separating higher and lower halves of values, in this case intensity values of each pixel of certain location in an image through the whole video. Minimum and maximum intensity values are also of each pixel of certain location in the image through the whole video.

The area of the keyhole opening was measured with automatic area measurement feature of ImageJ program using tolerance of 15 with legacy method from standard deviation images. The method determines how the measurement takes into account surrounding pixels and how many. Legacy method does not take additional surrounding pixels into the area measurement. This measurement method does not always result in a circular or even an ellipse form, but can also be a random shape. Due to this the area measurement was not used for keyhole volume calculation. The used area measurement ignores the circularity, but preserves the average keyhole opening area by using intensity values of the standard deviation. With this method it is possible to take into account the keyhole opening variations and achieve an average opening area.

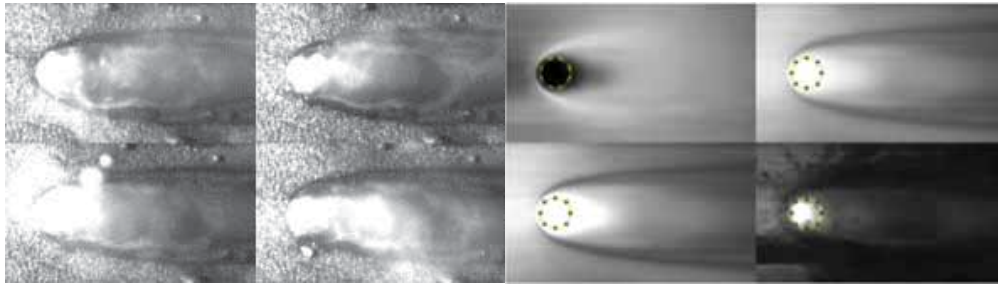


Figure 26. Four frames along the weld 200 ms on the left side and standard deviation, average, median and minimum intensity on the right clockwise from the upper left image.

The average and the standard deviation surface images were used to determine the circularity of the keyhole opening. All of the videos had considerable amount of additional high brightness reflections for example from the illumination laser via the molten surface. The KH (Keyhole) opening area was automatically measured, but the circularity was manually measured due to lack of proper and accurate method available.

3.10 Determining keyhole side view outline

In this thesis the x-ray videography was used to acquire the 3D-models of the keyholes. Partial penetration welds required also determination of the keyhole depth, which was calculated in Excel from the outlined average images. The assumption was that the keyhole bottom tip is near the keyhole centreline where the intensity of the x-ray in the image drops considerably, meaning that the molten pool or the solid sample starts. The intensity increases on the location of the keyhole due to smaller length of solid or liquid material the x-ray beam must penetrate. Metal vapour has much higher transparency to x-rays than liquid or solid steel. Automatic contrasting of the image was used and the keyhole side view was manually outlined, figure 27. The actual keyhole depth was calculated in an Excel sheet. Examples of keyhole side view geometry determination are presented in this chapter, partial and full penetration welding separately. The examples for the method explanations were randomly selected. The complete welding set was processed, measured and calculated in the Excel. The whole set of the cross-

sections of the keyholes in the welding direction are shown in appendices 3 and 4, also the keyhole side view outlines in appendices 17 and 18. The side view geometry was used to calculate the welding direction cross-section, depth and volume.

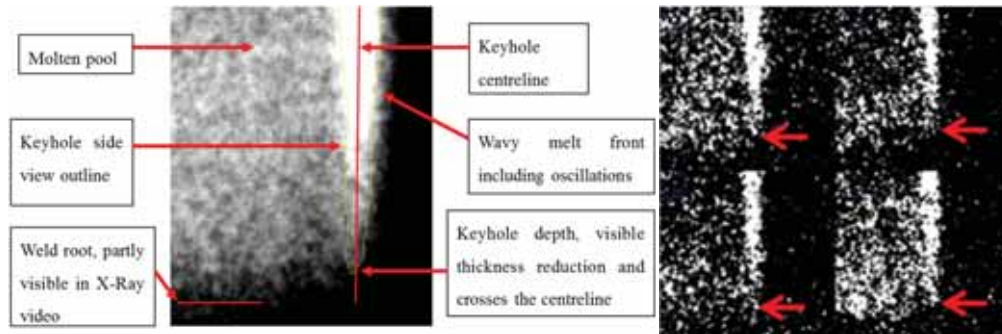


Figure 27. Two methods of measuring keyhole depth. Left side, the used method of determining the keyhole side view outline and on the right, a tested high contrast method.

The x-ray images and videos have noise which makes the recognition more difficult. A high contrast method was tested, shown in previous figure. The problem in the high contrast method is that it is possible to lose information due to extremely strong contrast adjustment. The accuracy is very good, few hundredths of a millimetre, but the possibility of lost information eliminates the usability of this method.

The keyhole side view outline is wavy and not each separate pixel was taken into account but rather a main form of the keyhole side view geometry. The edges of the keyhole are rather difficult to distinguish due to noise and very small thickness difference in the edge regions in the x-ray beam path. The keyhole average depth was determined, in which the keyhole stays most of the time. The location where the increased intensity (keyhole) crosses the keyhole's centreline is the average keyhole depth. The contrast was adjusted for each weld separately by automatic feature to prevent strong contrast which might in some cases cause loss of data. Figure 28 shows an average image of a keyhole and also minimum and a maximum intensity images. These were used in the determination of the side view outline. The minimum and maximum images give information of the fluctuations of the keyhole, and the molten front fluctuations. The averaged x-ray videos were used to measure also the keyhole front wall inclination angle where the beam hits the molten metal. The same Figure shows also an outline of one keyhole on the average, minimum and maximum images. The very top part of the keyhole is not as visible as the rest due to lead shielding plate that protects the scintillator from the excessive x-ray radiation. The minimum values image helps also to identify the keyhole opening outline.

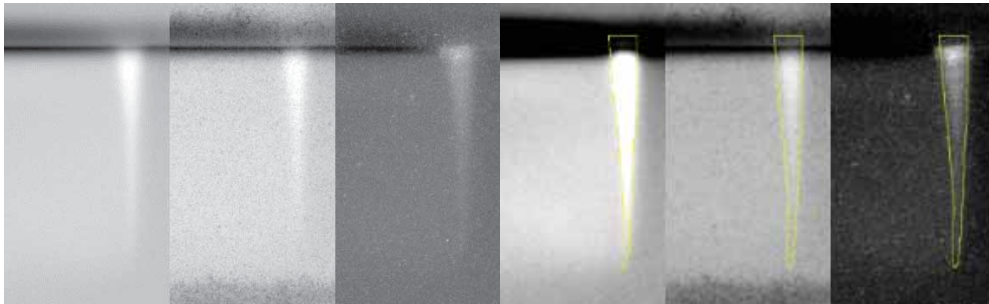


Figure 28. Average, minimum and maximum intensity images from x-ray videos and corresponding side view outline.

The sample thickness in the second set was 4.9 mm to allow full penetration with most of the parameters. The videos were processed and analysed similarly compared to samples of 7.8 mm thickness, except the keyhole bottom was mainly full penetration. The sample bottom was detected from the videos and this was used as keyhole bottom edge. In figure 29 there is one weld of 4.9 mm sample thickness shown as an example. The keyhole outline is shown also in the same figure. Minimum and maximum intensity images were used to help to identify the outline. The keyhole was penetrating completely through the weld sample.

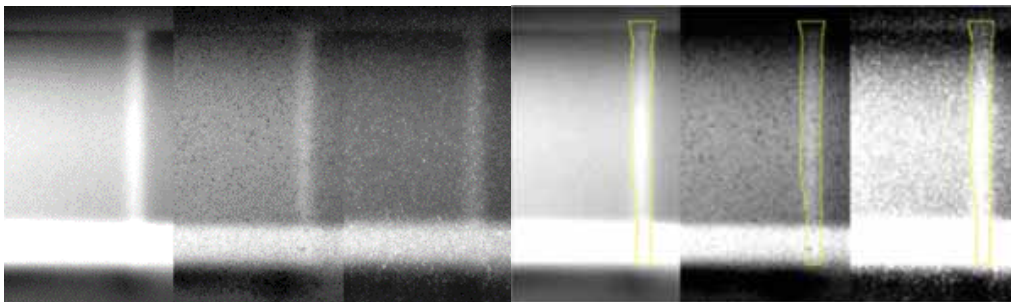


Figure 29. Average, minimum and maximum intensity value images for 4.9 mm sample thickness, BOP and corresponding side view outline.

Keyhole front inclination angles were measured from averaged images. The beam incoming angle affects the interaction angle between the laser beam and the molten wall. The interaction angle is determined by the beam incoming angle and the keyhole wall angle. Figure 30 shows the angles used in this thesis.

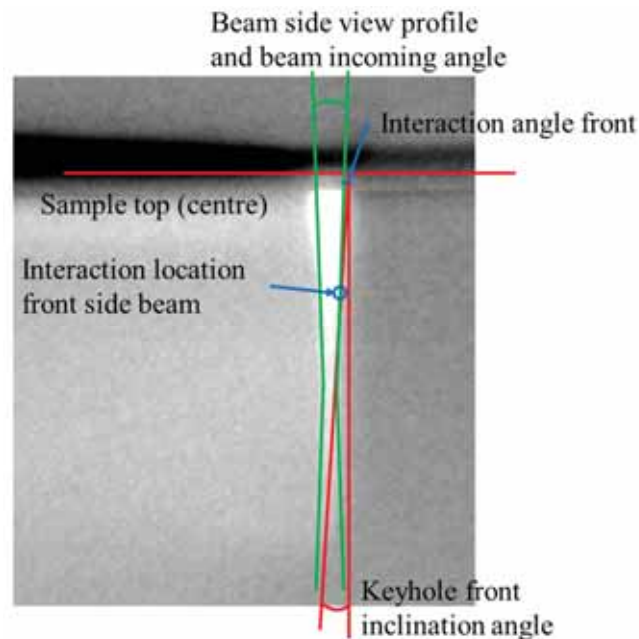


Figure 30. Representation of the angles used in this thesis. The red line represents the sample top in the centre, meaning the centre of the keyhole.

In the figure above, the interaction angle is marked to be an angle between the beam edge and the keyhole front inclination angle. This is only a simplified way of presenting the interaction angle and only one possible interaction location presented. The beam has several “small beams” inside that has slightly different angle when comparing to the keyhole front wall. For example a part of the keyhole back wall side beam has beam incoming angle towards the welding direction and a part of the keyhole front wall side of the beam has beam incoming angle towards the back of the process, towards the weld. Parts of the beam have beam incoming angle at 90 degrees to the welding direction in each case. These changes makes it impossible to completely explain the interaction angle in a simplified way. If the beam interaction angle are to be measured in all locations of the keyhole walls the beam must be separated into several sections and then perform beam tracing inside the keyhole. In this simplified way the interaction between the beam and the keyhole front wall is most likely to occur with the beam section that has beam incoming angle towards the keyhole centre, towards the weld. The further the observation area is from the keyhole front the deeper the interaction occurs with the keyhole front wall.

The interaction angle discussed in this thesis consists of the “interaction angle front”, which means the angle between the keyhole front wall and the beam front section. The interaction angles of multiple reflections are taken out of the results and discussions due to simplification of the phenomena in this study. Keyhole front angle is discussed in several sections and the interaction angle has been taken into account for some parts of the analysis and discussions.

3.11 Keyhole reconstruction and keyhole geometry calculation

Keyhole’s reconstruction was performed to calculate the keyhole volume and welding direction cross-sections. Several methods were tested to find the optimal, below is a list of tested methods, figure 31 shows one example of each:

1. MATLAB
2. Microsoft Excel
3. ImageJ, first method
4. ImageJ, second method

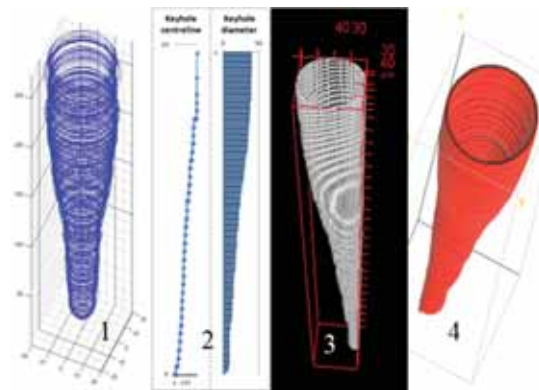


Figure 31. One example of each method, according to previous list.

The ImageJ method 1 was selected with some parts of the reconstruction done with Microsoft Excel. MATLAB was not sufficiently accurate and has complicated transfer to correct STL-model. Microsoft Excel did not result in a complete 3D-model of the keyhole and was used only partly. SolidWorks resulted in the most accurate, but smooth surfaced, model which was easy to transport to a mesh-model if required. The main problem with SolidWorks was the massive amount of manual work in the modelling of the keyhole.

Combination of ImageJ method 1 and Excel worked semi-automatically, meaning that the outlining of the keyhole was performed manually. ImageJ method 2 resulted in accurate 3D-model, but the transportation to a mesh-model was not possible and this method is mainly for visual aid. Figure 32 shows the process phases of a single weld. MeshLab simplification was performed due to large amount of faces (triangles in the mesh) in the original model, up to

200 000, which increases the loading times and causes the handling of the model to become slower in each phase. The work phases were:

1. Outlining of the keyhole
2. Removing background of the outlined image and filling the keyhole cross-section area
3. Transporting the visible image to a text-image
4. Importing the text image to Excel that calculates volume, depth and welding direction cross-section area
5. Importing a macro that Excel compiled, from the imported text image, to ImageJ
6. Visualisation of the welding direction cross-section of the keyhole
7. ImageJ transformation of Excel data to 3D-model of the keyhole
8. ImageJ transportation of the 3D-model to a mesh model
9. Mesh simplification with MeshLab.

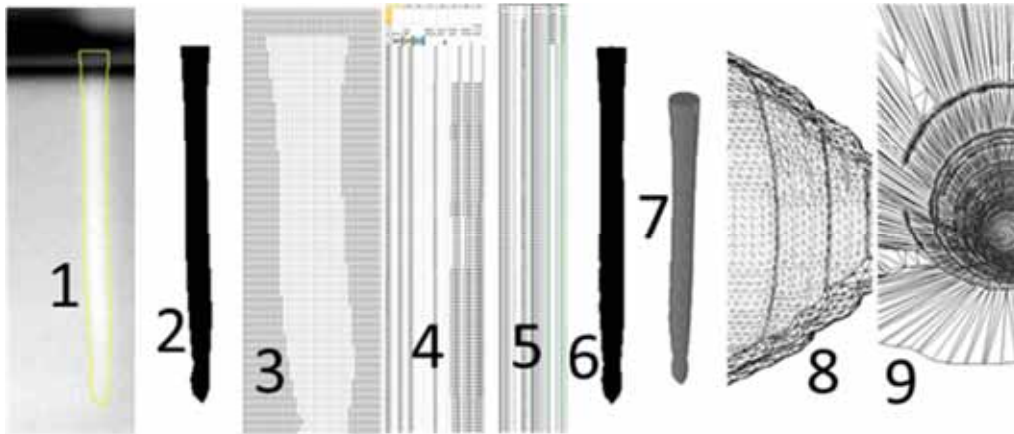


Figure 32. Images of the keyhole during the reconstruction phases mentioned in the list above.

The keyhole geometry, including the depth, the volume and the cross-section area in the welding direction, was calculated in the Excel sheet after importing the text-image. It was possible to calculate and extract the welding direction area with Excel back to ImageJ to construct the black and white image.

Some CAD programs such as SolidWorks allow importing of an image, which can be used as a base for the solid model, figure 33. An average image of the keyhole side view outline was imported into SolidWorks and that was used to draw the frame for the model. Circles were used as a guiding tool for lofted-boss feature which constructs the 3D-solid model out of the frame. This is a very accurate method and results in a solid model that can be transformed into the mesh model relatively easily or used almost in any other modelling or simulation program. The keyhole sides can be smoothed if needed, or a rougher surface can be done following the keyhole front and back walls, but still the final 3D-model is slightly smoothed.

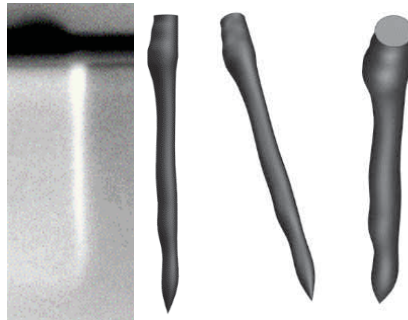


Figure 33. SolidWorks, 3D-solid model of the keyhole.

If a smoothed surface is used in the 3D-object, as shown in previous figure, the result can be slightly inaccurate due to molten metal flow and possible humps on the front and possibly also on the back keyhole walls. On the other hand, the humps are moving and this can affect to keyhole geometry in multiple ways, such as momentary spiking due to hump or volume changes due to hump volume. The positive features with SolidWorks are good control of the form and easily usable format of the 3D-model. The SolidWorks is widely used 3D-modelling program and the model format is well usable in many simulation programs. The downside of this method is the very large amount of manual work. Compared to other methods tested this was the most time consuming. Several features of the 3D-solid object model can be measured, such as volume, surface area, diameter and depth.

3.12 Melting efficiency

Melting efficiency was calculated using laser power, weld cross section area and the welding speed, resulting in mm^3/kJ as efficiency units. The cross section weld area was based on average of two macrographs of each weld to achieve the most common weld area for the used parameter combination. This calculation gives information how many cubic millimetres can be welded with 1 kJ and is independent from the penetration. The comparison between each combination can be done in one phase due to excluding joint type from the calculation.

3.13 Tracer material selection

According to the calculations in appendix 20 “Mass attenuation coefficient”, two tracer materials were selected, molybdenum and tungsten. Molybdenum was in a wire form of 1.0 mm in diameter and tungsten as a powder approximately of 10 μm particle size. These two materials showed to have higher mass attenuation coefficients than the base material and are visible in the x-ray videos. The molybdenum is easy to acquire in the wire form and due to similar properties acts similarly with the base material. Tungsten has significantly different material properties and due to that it was used as a powder form.

4 Results and analysis

The welding results were analysed using several methods, concentrating on the keyhole geometry and the changes in the geometry when the welding parameters and joint type are modified. The keyholes were outlined from the averaged x-ray side view images. The depth, welding direction cross-section of the keyhole and the volume was automatically calculated from the outlined images in an Excel sheet and then compared with the weld geometry. The different aspects of the keyhole geometry with the four types of joint geometries are presented.

Partial penetration welds from 4.9 mm sample thickness graphs were removed due to the goal of fully penetrating keyhole. The partial penetration in these graphs would cause inaccuracy due to dramatic geometrical change of the keyhole.

4.1 Keyhole and weld geometry

The keyhole geometry was calculated and concentrated on four different areas which were: keyhole volume, depth, welding direction cross-section area and front inclination angle. The depths and the areas were compared directly with the corresponding parameter combination weld depths and areas. Short terms of PP (Partial Penetration), FP (Full Penetration), BOP (Bead on Plate), IBJ (I-Butt Joint), KH (Keyhole) and FPP (Focal Point Position) are used in all graphs and the text.

4.1.1 Keyhole opening area

Keyhole opening was measured from the visual high speed videos, using the method described are shown in figure 34. The figure also shows the calculated beam area on the sample surface. The circles represent the largest keyhole opening areas.

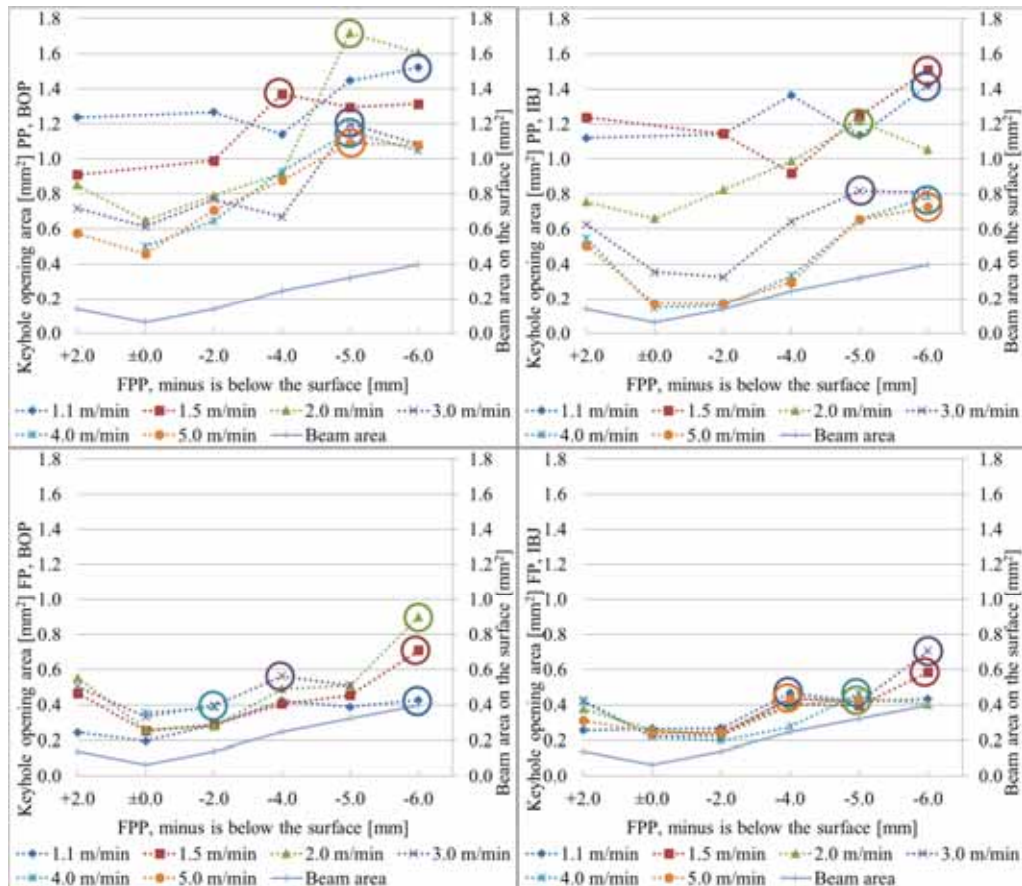


Figure 34. Keyhole opening areas. Calculated with a perfect circular keyhole depth geometry.

The smallest keyhole opening areas occurred with the smallest beam areas on the surface and the largest mainly with the largest beam areas on the surface. The connection between the keyhole volume and the keyhole opening is relatively clear with all welding parameters, especially with partial penetration samples. The cylinder mode is not directly visible in the comparison between the keyhole volume and the keyhole opening areas, the welding speed affects the mechanics, via vaporisation mass which is connected to keyhole opening also but not only that, and this causes the direct comparison with volume and opening irrelevant concerning cylinder mode. With PP samples the keyhole opening is considerably larger with slow welding speeds overall and the same phenomenon occurred with both BOP and IBJ types.

The dimension and shape of the keyhole in the X-Ray direction still remains unknown, but theoretical review supports circular shape. The ratio between the keyhole opening length and width was measured from standard deviation visual videos. The results are shown in figure 35.

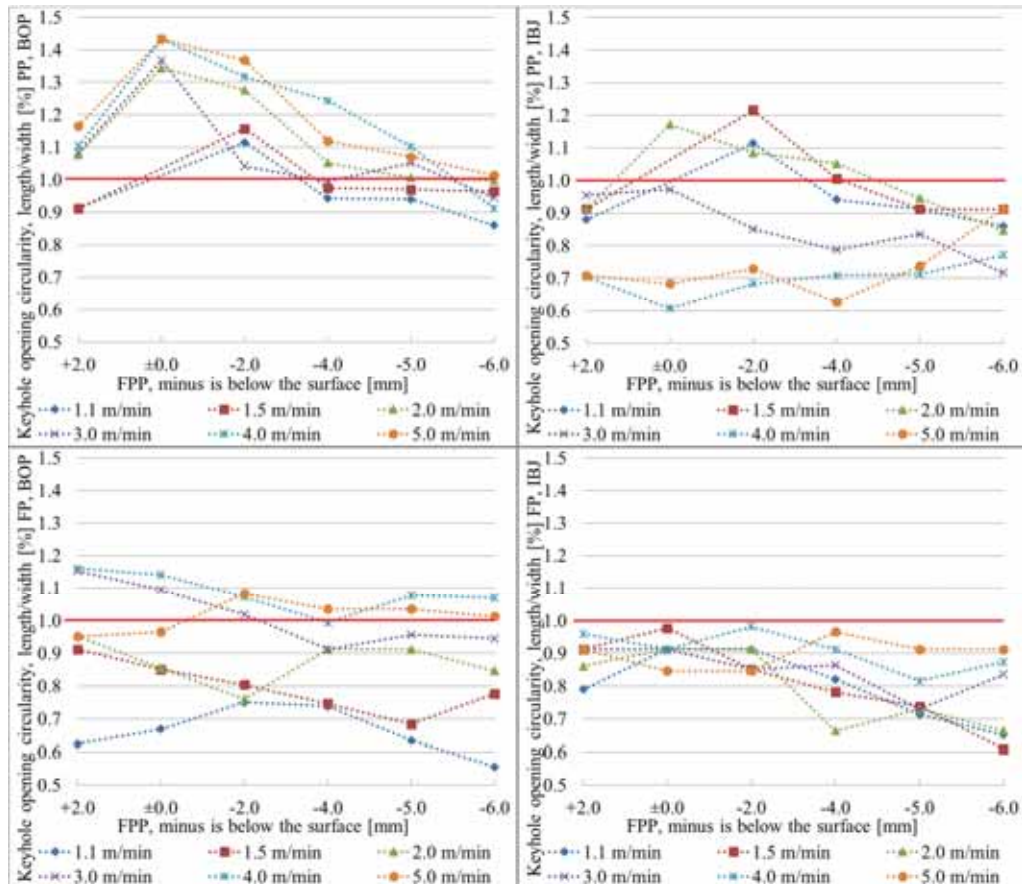


Figure 35. Keyhole opening circularity. Values above 1 means that the keyhole opening is longer in welding direction and values below 1 means that the keyhole opening is longer in transverse to the welding direction.

The FP samples on the other hand are not sensitive to welding speed, and all parameter combinations result in similar keyhole opening area. The opening size is larger with large beam areas on the surface and this increases keyhole volume clearly. The laser beams energy density was sufficient to maintain keyhole open on the whole area of the beam. This implies that all of the laser beam's energy is transported inside the keyhole and none of the energy is absorbed by the solid sample surface or the molten surface outside of the keyhole area. This shows that there is strong vaporisation present that increases KH opening significantly at low welding speeds. This is valid if the keyhole is circular or oval but if the keyhole opening is irregular, some interaction might happen with the solid sample also.

Full penetration showed that the keyhole is more likely wider when compared to keyhole opening length and especially with FP IBJ the keyhole was wider than the length of the opening. This is to be taken into account due to the joint being in longitudinal in welding direction, but the keyhole opening is still wider. In some cases the keyhole seemed to be irregular in form, figure 36, but still the width was larger and the keyhole is tend to open also in the joint direction. In the back side, the molten pool restricts the keyhole opening but it was free on the joint side. This is complicated to confirm especially due to strong reflections from the molten pool surface that occurred especially on the keyhole front area inside the bevel. As shown from the figure, the PP keyhole opening is more irregular in shape, but the bevel was also slightly larger in 7.8 mm thick samples.

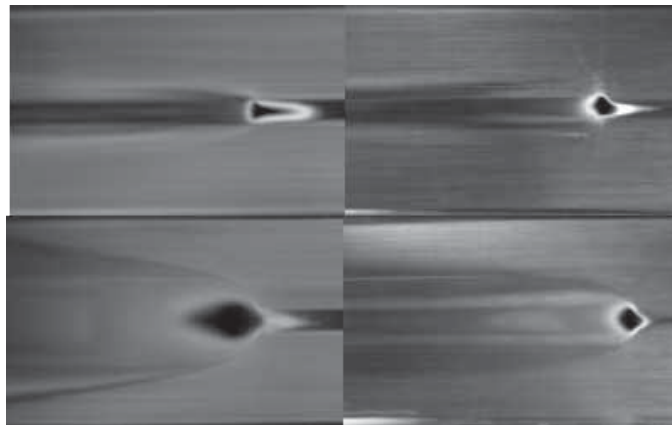


Figure 36. Irregular keyhole opening, on the upper left side PP IBJ with 4.0 m/min and -2.0 mm FPP and on the upper right same parameters with FP. Lower images have same FPP but welding speed of 1.5 m/min, PP on the left and FP on the right. Beam moving direction to the right.

As shown, the keyhole opening can be irregular especially with IBJ and the penetration type affects also. Full penetrating keyholes were less irregular when comparing to the partial penetration keyholes. It must be taken into account that the camera was in 60 degree angle and the keyhole might not have molten metal on the sample surface area, meaning that the keyhole does not have a front wall on the sample surface. This causes the keyhole to appear irregular due to missing material. The keyhole is formed deeper into the sample in some cases, this was also visible in the weld cross-sections by having underfilled groove. Figure 37 shows same parameters with BOP.

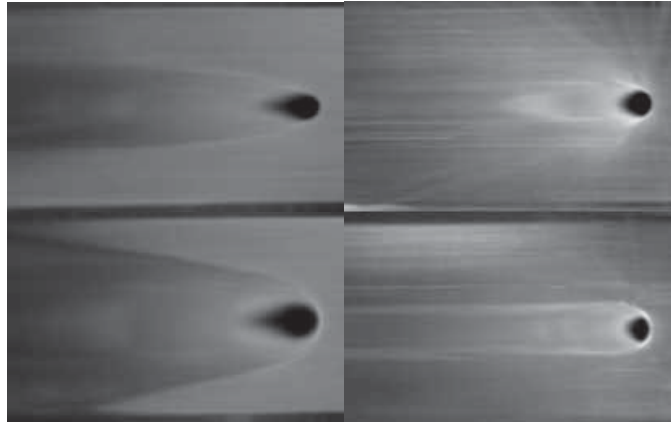


Figure 37. Irregular keyhole opening, on the upper left side PP BOP with 4.0 m/min and -2.0 mm FPP and on the upper right same parameters with FP. Lower images have same FPP but welding speed of 1.5 m/min, PP on the left and FP on the right. Beam moving direction to the right.

Bead on plate does not results in such irregular keyhole opening as the IBJ. The penetration type still affects and with FP the keyholes are more circular. Appendices from 19 through 22 shows all keyhole openings.

4.1.2 Keyhole volumes

Keyhole volumes for each parameter sets and joint types were calculated and are presented in figure 38. Maximum keyhole volumes are dash circled in corresponding colour and minimum are solid line circled.

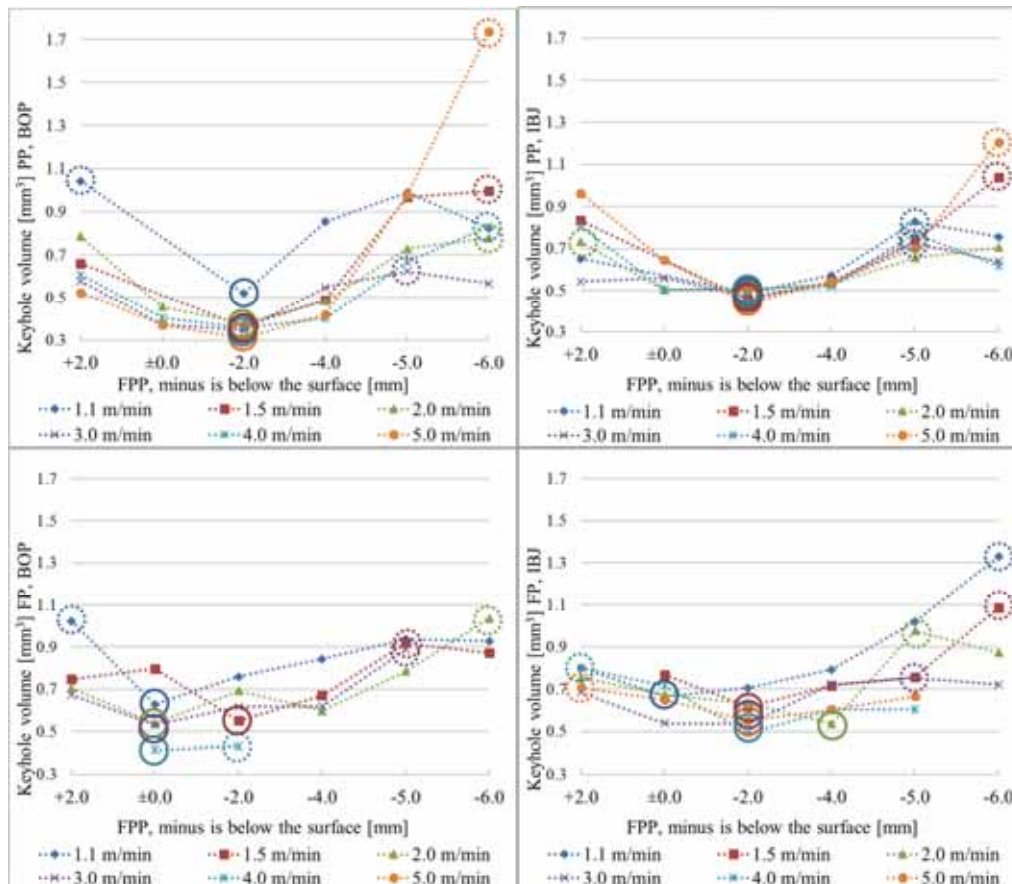


Figure 38. Keyhole volumes for each joint type with various welding speeds and focal point positions.

Both joint types in PP tests showed relatively uniform trends for each welding speed, the smallest volumes were calculated mainly for -2.0 mm FPP. The largest volumes had some variation, with the lowest welding speed of 1.1 m/min the largest volume occurred with +2.0 FPP with BOP. At higher welding speeds the largest vapour volumes were mainly with -6.0 FPP. Cylinder mode keyhole had the largest effect at 5.0 m/min welding speed. The large FPP was mostly the main cause of large keyhole volume, but exceptions also existed, mainly with the slowest welding speed of 1.1 m/min.

Full penetration samples resulted in relatively large variations with BOP, but there were clear similarities such as the area of minimum keyhole volume being ± 0.0 or -2.0 mm FPP. The FP IBJ behaved very similarly with PP welding process and a very similar trend can be seen in the graphs. The smallest keyhole volumes were achieved with -2.0 FPP and largest mainly at -6.0 FPP. This shows that the most optimal penetration parameters results mainly in the smallest keyhole volume, the energy is directed deeper into the material efficiently. With FP BOP, the smallest keyhole volumes were calculated mainly for the ± 0.0 FPP and only one for -2.0 FPP.

The second calculation was with the keyhole opening geometry being used throughout the whole KH depth. This means that the keyhole geometry is not a perfect circle but follow the keyhole opening shape. The results are in figure 39.

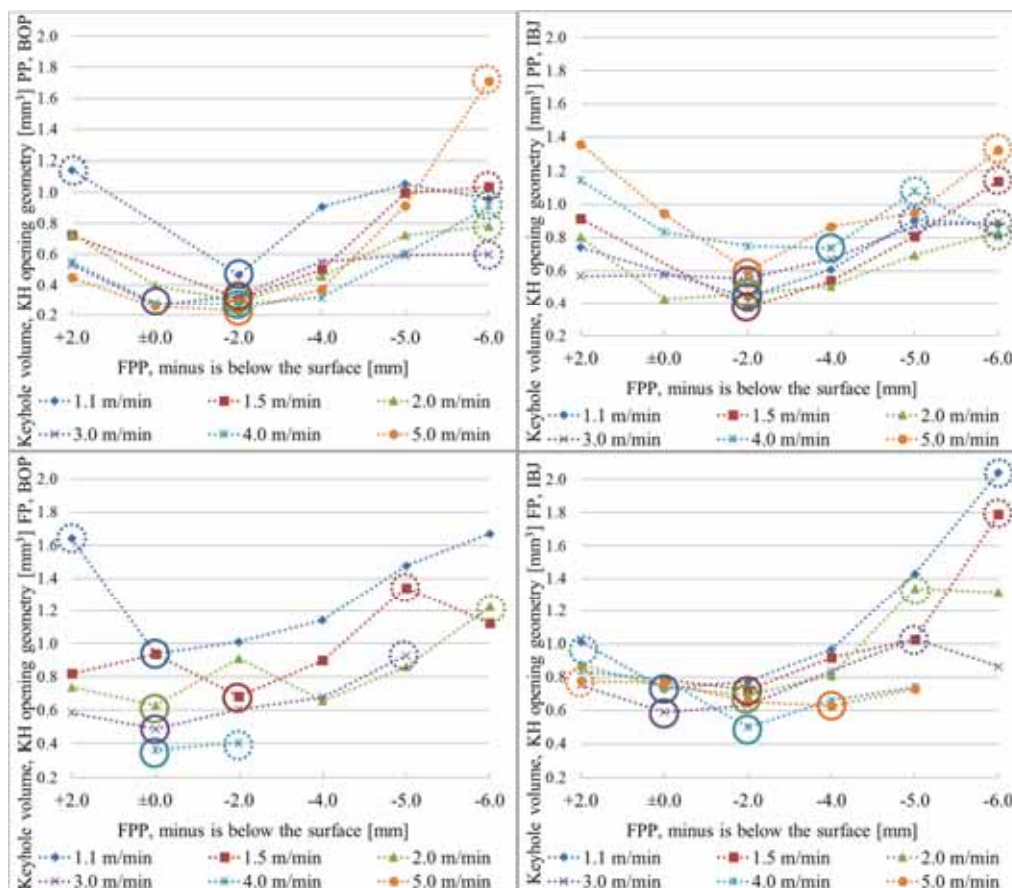


Figure 39. Keyhole volumes calculated with keyhole opening geometry.

When the keyhole opening geometry was taken into account the effect was varying for each weld set and largest differences occurred at full penetration bead on plate. Especially the full

penetration I-butt joint with slow welding speeds 1.1 and 1.5 m/min and -5.0 to -6.0 mm FPP the increase in keyhole volume was significant. This was due to wide keyhole opening when comparing to the keyhole opening length. The differences between the KH volumes of these two methods can be seen from figure 40.

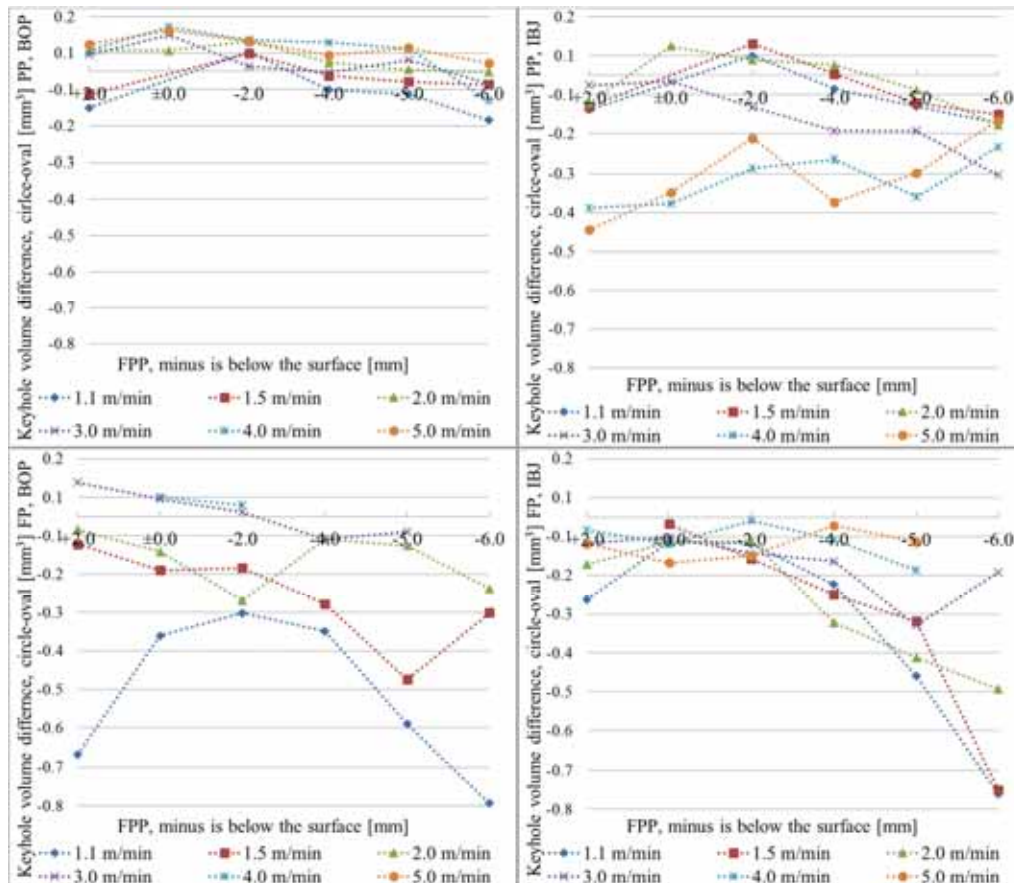


Figure 40. The differences of two different methods of calculating the KH volume, circular – KH opening geometry.

When the ratio value has minus sign the volume with KH opening geometry was larger than the volume calculated with the circular geometry. As can be seen the largest differences occurred at different welding speeds, depending on the joint type. The PP BOP resulted in the smallest differences between the methods and FP BOP very large difference with slow welding speeds of 1.1 and 1.5 m/min occurred. The PP IBJ had large increase in volume when calculated with KH opening geometry at high welding speeds of 4.0 and 5.0 m/min. The FP IBJ in the other hand has very large difference with almost all welding speeds at large -FPPs.

The main trend lines shows the same with both methods, that the minimum KH volumes occurred at -2.0 mm FPP and largest mainly at the -6.0 mm FPP. The full penetration bead on plate had large deviation in the measurements, unlike the partial penetration bead on plate welds.

4.1.3 Partial penetration keyhole and weld depths

Keyhole and weld depth comparison was performed for partial penetration welds, shown in figure 41, for both BOP and IBJ. The deepest penetration depths are marked with corresponding coloured circles in each graph. The weld depths were measured from two random locations and then an average of two was calculated.

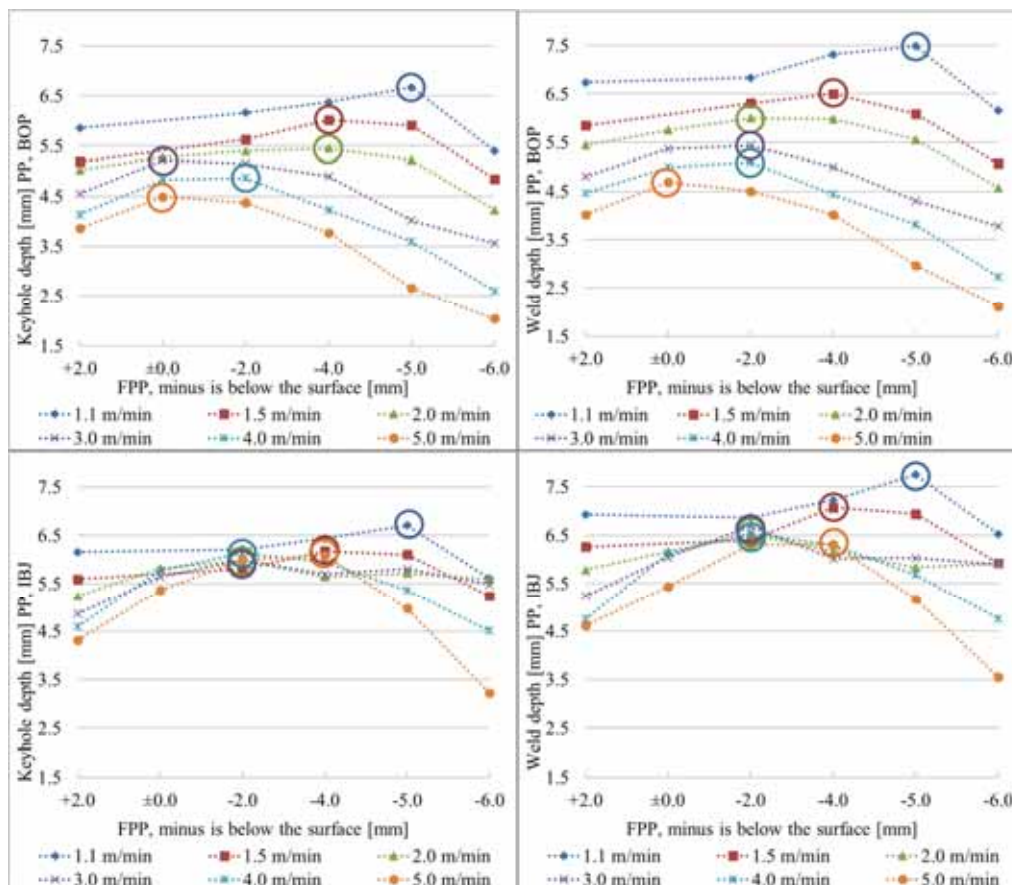


Figure 41. 7.8 mm sample thickness keyhole and weld depths with various welding speeds and focal point positions.

The keyhole maximum penetration, of 6.7 mm, was achieved with welding speed of 1.1 m/min and -5.0 FPP resulting in a weld of 7.5 mm in depth, averaged from two macrographs along the weld. The weld penetrated the whole sample thickness (7.8 mm) in several locations along the

weld length. The maximum penetration is dependent on the welding speed and also strongly on the FPP. This shows that the keyhole depth, on this laser power range, is not largest with the smallest beam area on the surface, which would result in the maximum intensity. The higher the welding speed the higher the surface intensity is needed to achieve deepest keyhole penetration possible. With 5.0 m/min the deepest keyhole penetration was achieved with the FPP on the surface, at the highest intensity.

With each parameter combination +2.0 FPP resulted in shallower penetration than -2.0 FPP, showing that the beam incoming direction at the sample surface changes the keyhole behaviour by changing the absorption angle of the beam onto the keyhole molten walls. The effect increases with the increase of welding speed, especially with IBJ.

When BOP and IBJ are compared, the keyhole depth was similar with low welding speeds of 1.1 and 1.5 m/min regardless of the considerable bevel on the top quarter. The deepest penetrations were also achieved with these low welding speeds and the BOP showed steady decrease in depth with increasing welding speed. IBJ behaves differently at higher welding speeds. The depth has increased significantly at and above 2.0 m/min with IBJ compared to BOP and the bevel also caused slight underfilling with most parameter combinations. This underfilling behaviour increased also the keyhole and weld depth due to missing molten front on the sample surface.

Keyhole depth divided by weld depth - ratios were calculated and are shown in figure 42. The largest molten pool depth in addition to KH depth was at the slowest welding speed of 1.1 m/min and this resulted in KH to weld ratio of 88 % in both bead on plate and butt joint. The smallest difference was found to be at highest welding speeds of 4.0 and 5.0 m/min. According to the keyhole to weld depth ratio the slower welding speeds resulted in deeper weld penetration when compared to keyhole penetration. In the case of higher welding speeds, of above 3.0 m/min, the molten metal flow and convection are smaller due to higher moving speed of the keyhole and significantly faster cooling rate of the molten metal, especially in the bottom of the molten pool. The keyhole was narrower in the bottom quarter with higher welding speeds when comparing keyhole geometries.

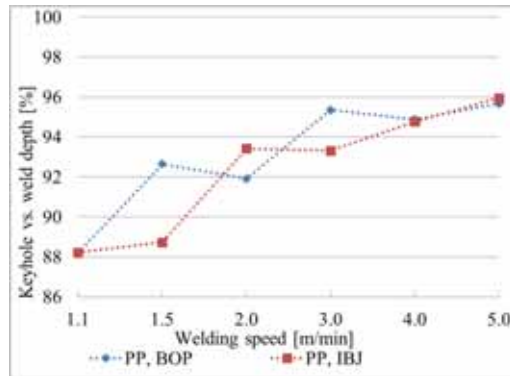


Figure 42. Keyhole depth divided by weld depth.

The graph shows approximation of the molten pool depth below the keyhole depth and thus should not be taken numerically but rather as a trend graph that the molten pool depth below the keyhole increases with slower welding speeds. This results that with higher welding speeds the keyhole depth determines the weld depth close to 100 % certainty. The largest and deepest molten pool below the keyhole occurred with the slowest welding speeds and the ratio steadily increased up to 5.0 m/min in which the ratio was at its highest. This suggests that there was a stronger molten pool flow on the bottom area at slow welding speeds. With higher welding speed the difference and the molten pool size below the keyhole decreased.

Keyhole depth per volume was calculated using the reconstructed geometry of the keyhole and is shown in figure 43. The units are arbitrary units. Both BOP and IBJ for PP are shown in the figure. This calculation was performed due to test to confirm the connection between the penetration and the volume.

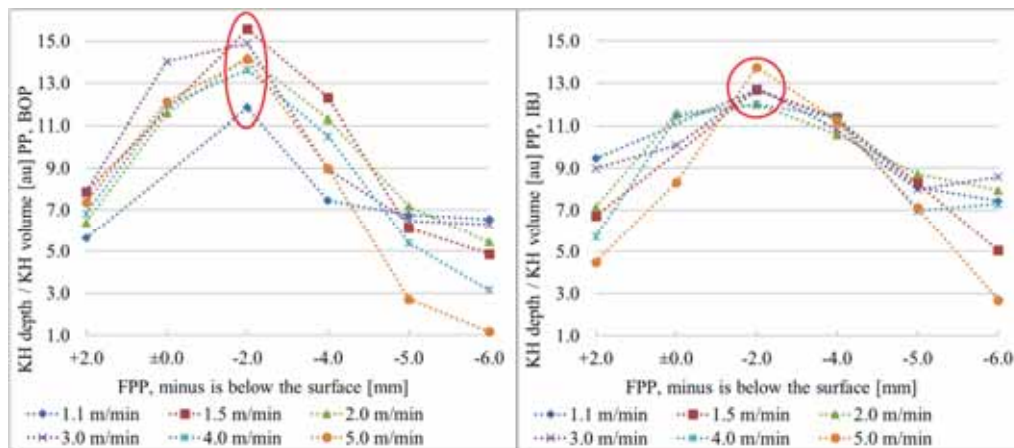


Figure 43. Keyhole depth per keyhole volume with various welding speeds and focal point positions.

When the keyhole opening increased the volume increased; in addition the penetration decreases. Both PP BOP and IBJ show a clear trend and even with the deepest keyhole achieved with -5.0 FPP with PP BOP, the KH depth per volume still showed the same -2.0 FPP to be most efficient in this comparison. This means that the smallest vapour volume is achieved with -2.0 FPP and resulting deep penetration with small amount of vapour volume.

4.1.4 Partial penetration keyhole and weld cross-section areas

The weld cross-section area comparison was performed for partial and full penetrations separately. Figure 44 shows PP welds for both BOP and IBJ. Keyhole cross-section areas are in the welding direction and are the largest areas to show the maximum vapour area in the welding direction. The cross-section is not a straight line like a weld cross-section, but rather a curved line following KH side view outline's middle section. The laser welding process at its best is stable and oscillations are minimal which results in stable keyhole geometry.

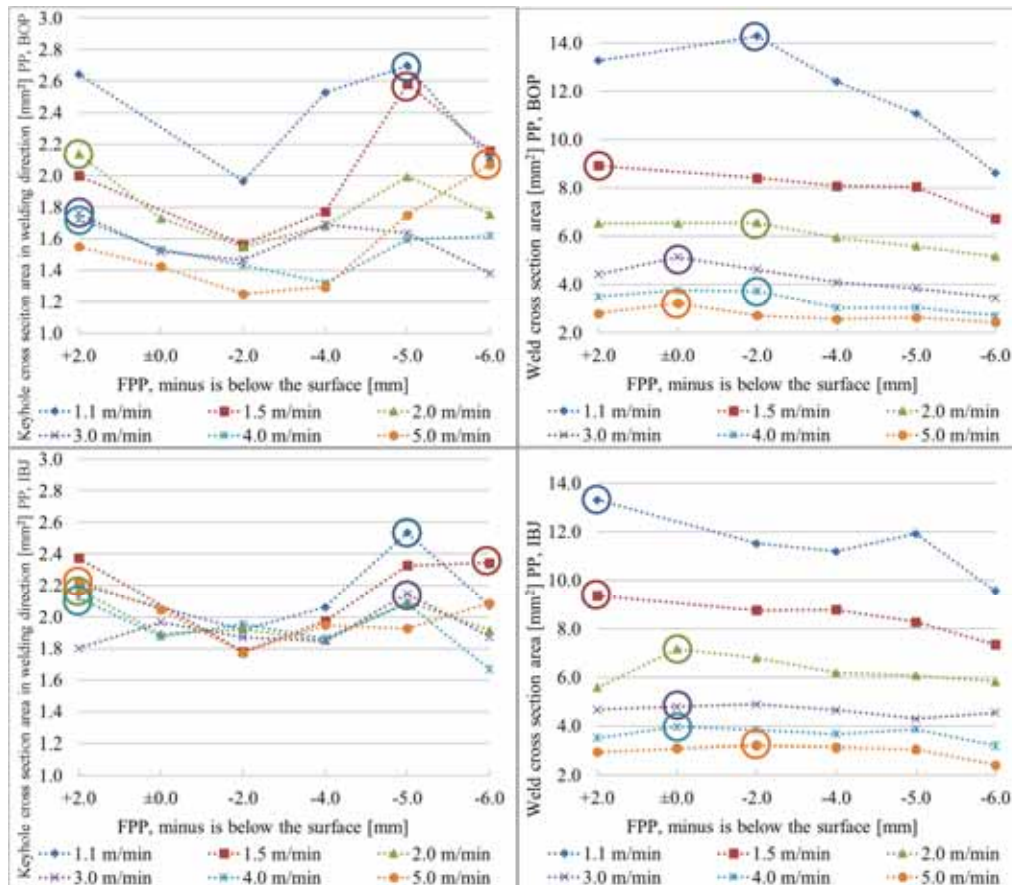


Figure 44. Keyhole (left side) and weld cross-section areas (right side) of 7.8 mm samples with various welding speeds and focal point positions.

The largest keyhole cross-section areas did not result in the largest weld cross-section areas and both joint types show the same main behaviour. The different keyhole behaviour between +2.0 and -2.0 FPP causes the +2.0 to generally have a larger keyhole cross-section area. The keyhole behaviour was not dramatically changed between these two FPPs, but the geometry of the keyhole changed such that the +2.0 FPP had significantly wider cross section on the top half. This shows that the absorption was higher on these due to larger vapour volume. This resulted in decreased depth for +2.0 FPP which affects the keyhole cross-sectional area directly. There were no clear relationships between keyhole area and the weld area due to considerable changes in the keyhole geometry.

4.1.5 Full penetration keyhole and weld cross-section areas

A similar comparison was performed for 4.9 mm thick samples, FP samples, as for the 7.8 mm samples, PP samples. Figure 45 shows keyhole cross-section areas in the welding direction and also the weld cross-section areas for both joint types. With FP samples the partial penetration welds were taken out of this comparison to compare only full penetration welds.

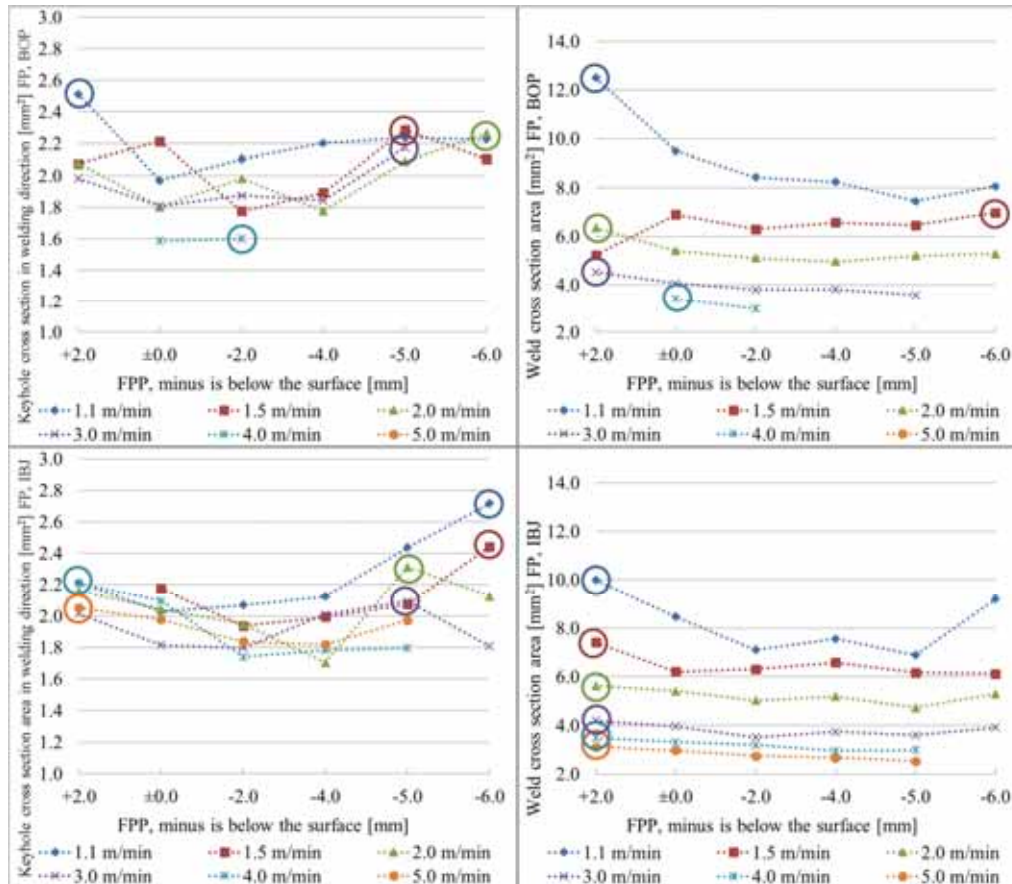


Figure 45. Keyhole (left side) and weld cross-section areas (right side) of 4.9 mm samples with various welding speeds and focal point positions.

Similar trends to those shown previously were found; the largest keyhole areas are mainly not corresponding with the largest weld areas. The keyhole or the weld depth was not affecting due to full penetration of the welds and the keyhole was always open on the root side. Even when there is no connection between these two areas, a clear main trend line can be seen with the keyhole volume. The +2.0 and -6.0 FPP shows slightly larger keyhole areas and still have full penetration. There is a relatively clear trend for weld areas between +2.0 and -2.0 mm FPPs. The weld is formed via other phenomena and the keyhole size is not the only phenomenon affecting the weld area.

4.1.6 Keyhole front inclination angles

The keyhole front inclination angle affects the interaction angle between the laser beam and the molten wall and also on the reflections inside the keyhole. The incoming beam direction of the laser beam is important for the process mechanics, especially when it changes from outwards to inwards. The laser beam absorbs onto the front and the keyhole walls, also reflects from it. The reflection is at its highest when the angle of incidence is close to 90 °, this angle is normal to the surface, and absorption maximum is approximately at 80 degrees, normal to the surface. The angle used in reflectivity graph is different than the angle used for keyhole front inclination angle. The keyhole front wall does not determine the actual interaction angle of the beam and the material by itself, but does affect together with the beam incoming angle and direction. With ± 0.0 FPP the beam angle on the sample surface is close to 0.0 degrees normal to the surface as an average, there are mixed beam paths and the centre is always perpendicular to the sample surface. With $-FPPs$, the incoming direction is mostly inwards, towards the centre of the beam, at the sample surface. This affects the interaction angle of the laser beam and the keyhole molten wall. With $+2.0$ FPP, the keyhole and the weld were larger on the top than with -2.0 FPP. See figure 30 for visual angle representation.

Figure 46 shows the keyhole front inclination angles for each parameter combination and joint type. The largest angles are circled with responding colours. These angles were measured from the averaged side view outlines and are angles between perpendicular line from the sample surface and the keyhole front wall. The average angle of the upper half was taken into account due to some keyholes being curved or the angle changes at some location.

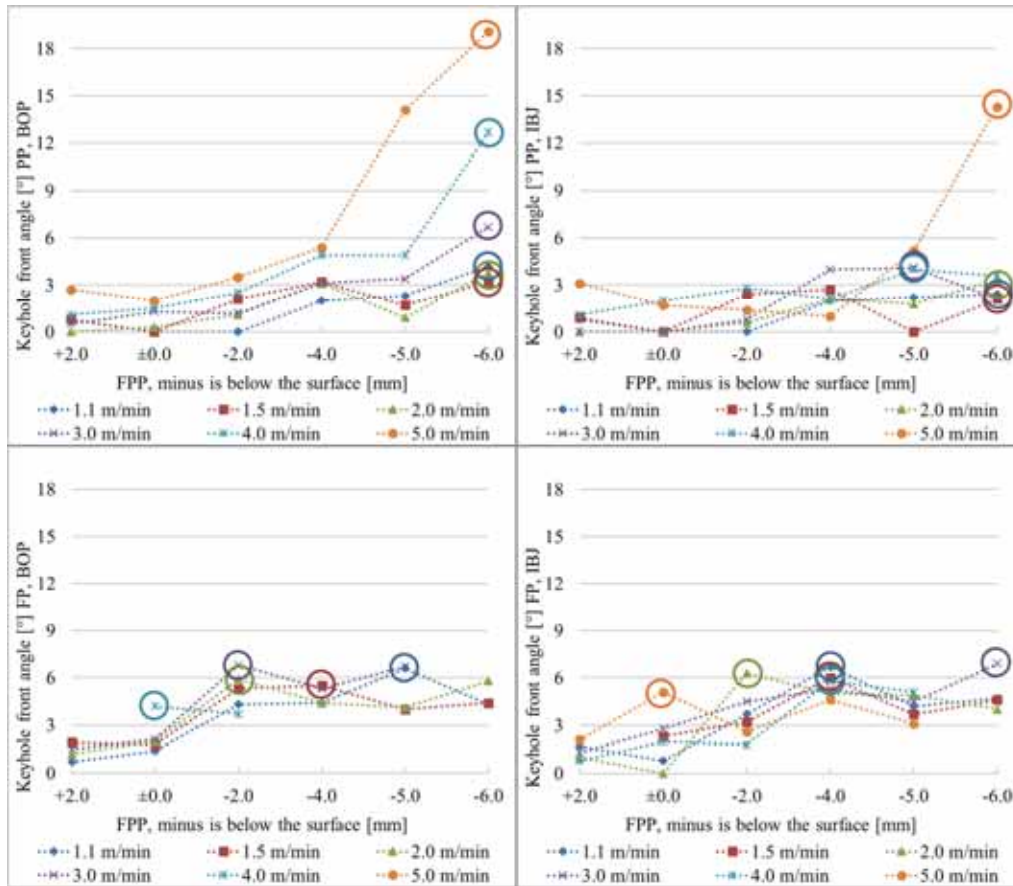


Figure 46. Keyhole front wall inclination angles.

PP BOP resulted in cylinder mode keyhole at angles above 12 degrees and this was visible with several parameter combinations and two joint types. In the cylinder mode area the keyhole was significantly shallower but also the welding speed affects the cylinder mode formation via vaporisation mass. The front angle increases relatively steadily with each parameter combinations, but the BOP 5.0 m/min shows the most significant increase after -4.0 FPP. The angle at PP IBJ 5.0 m/min and -6.0 FPP was large and caused cylinder mode keyhole, figure 47.

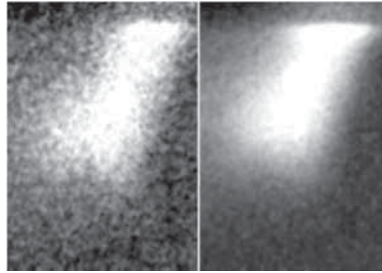


Figure 47. Keyhole side view from x-ray video. A cylinder mode, a single frame from a random location and an average on the right.

The differences between other parameter combinations with PP IBJ are smaller due to the bevel which changed the keyhole behaviour by increasing depth and reducing the molten metal in front the keyhole at the top surface.

The FPs are very similar due to each keyhole being full penetrating. The same cylinder mode occurred also with 4.9 mm thick samples but since the penetration was partial, the results are not presented in the graph. This causes the front angles be very similar within FP welds. The FPPs below -4.0 mm resulted in larger angle due to larger beam area on the surface and larger opening of the keyhole when compared to FPPs of +2.0, ± 0.0 generally and -2.0 FPP with IBJ.

4.1.7 Weld top surface bead widths

To compare +2.0 and -2.0 FPPs and the top surface bead widths, figure 48 shows top bead widths for all parameter combinations. From this figure the bead width comparison can be performed. The top half and the surface width is in the focus due to differences between +2.0 and -2.0 FPPs in which both have the same calculated beam area on the surface.

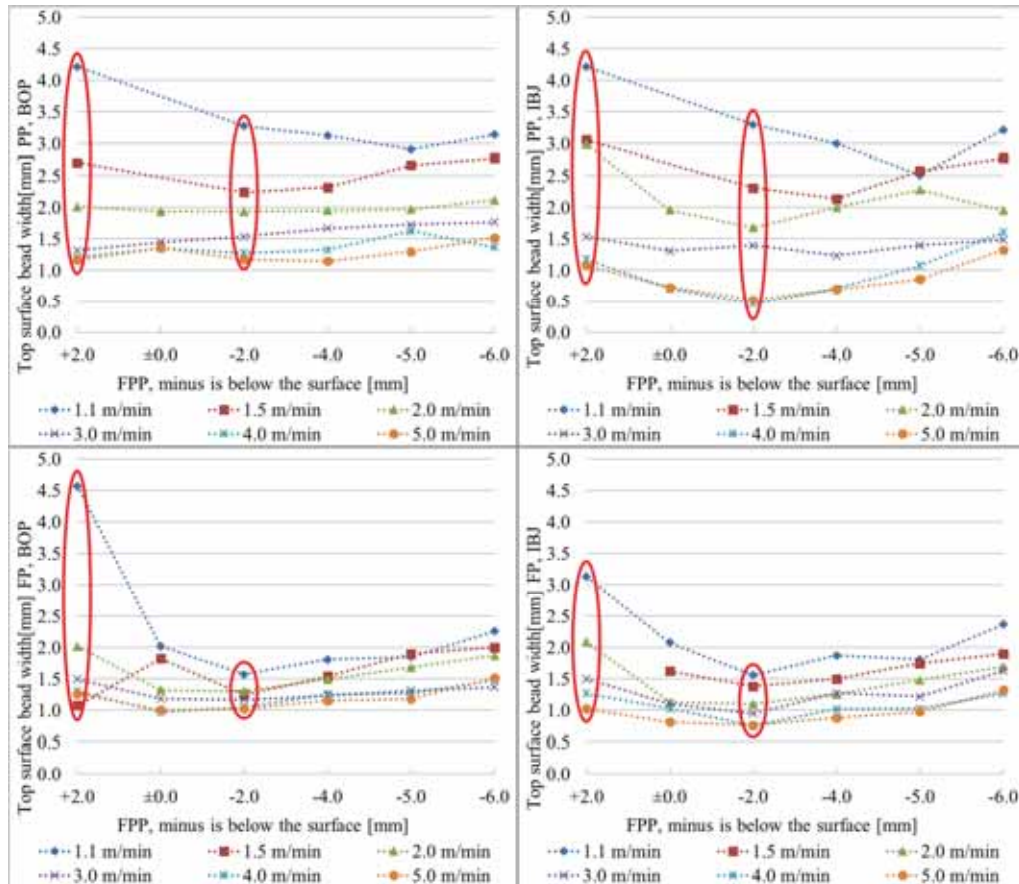


Figure 48. Top surface bead widths to compare +2.0 and -2.0 FPPs.

With most of the parameter combinations the +2.0 FPP shows considerably wider bead reinforcement. Only few parameter combinations resulted in wider top surface bead with -2.0 FPP, but the occurrence is low and those cannot be considered as conclusive results.

4.2 Keyhole modes

Three different stable keyhole main types, or modes, were detected, these are called:

- Trap (T) with subtypes of narrow and wide trap (NT and WT) and the narrow trap mode acts also in high and low welding speeds (hsNT and lsNT)
- Cylinder (C)
- Kaleidoscope (K), with subtypes of even width kaleidoscope (EK) and large opening kaleidoscope (LK). Kaleidoscope acts in full penetration mode. Another sub-mode is open cone, which is very similar to WT-mode but has a small opening on the root side.

Main characteristics and definitions are explained with example images acquired with the x-ray videography of corresponding keyhole modes. Within the sub-modes the keyhole acts similarly but the molten pool behaviour and formation of the weld geometry is slightly different between the sub-modes.

4.2.1 Trap mode (Keyhole T-mode)

Trap, or a light trap, is a closed cone shape and redirects the light deeper into the cone while absorbing part of the light throughout the depth. The molten metal wall around the keyhole acts as an absorber and a reflector and the interaction angle determines the reflectivity. The smaller the interaction angle is the higher the reflections are when considering an average absorption. Figure 49 shows narrow light trap mode at high welding speed. The keyhole front wall, the molten wall, is presented with green line and the keyhole front inclination angle is shown below each image. See figure 30 for explanation of the angle terms used. The trap mode has several sub-modes in which the keyhole itself acts similarly but the weld geometry and molten pool flow paths are different. Approximately 10 mm of the welding length was cut from the beginning due to keyhole formation and from the end due to keyhole collapse when the laser is gradually shut off.

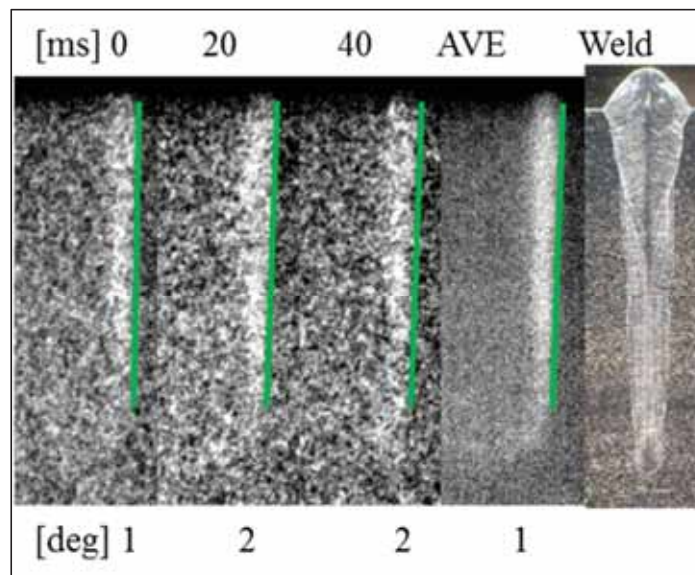


Figure 49. Narrow trap mode keyhole at high welding speed (hsNT). PP BOP, 5.0 m/min, ± 0.0 FPP. AVE means average image of the whole stable welding length.

The high speed narrow trap (hsNT) redirects light efficiently deeper into the sample. The weld geometry was in accordance with the keyhole geometry and the welding process and the keyhole behaviour was stable, only very small fluctuations occurred, such as front angle degree changes in the range of only one degree. The keyhole tip bends slightly backwards in the root area and no pores were visible in the x-ray videos. Even with the bending of the tip it had no visible effect on the weld geometry. The main features includes narrow even width keyhole to the last fifth of the KH, which is the root area.

The same type of keyhole occurs also with low welding speed, of 2.0 m/min in figure 50 (lsNT). The keyhole in narrow trap mode, acts similarly at low and high welding speeds. The molten metal behaviour on the other hand is slightly different on the upper half of the depth. The KH mode does not change the molten metal behaviour, the welding speed causes different type of molten metal flow and changes convection. This phenomenon increases the size of the weld on the upper half.

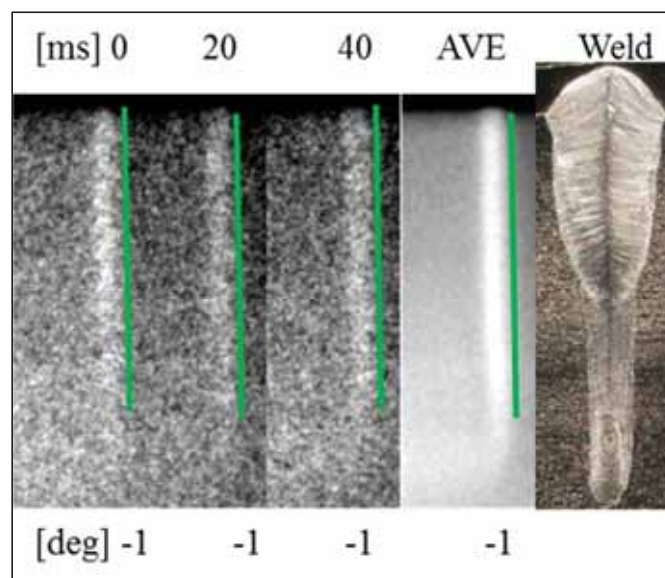


Figure 50. Narrow trap at low welding speed (lsNT). PP BOP, 2.0 m/min and ± 0.0 FPP.

As shown, the keyhole at both low and high speeds had the same geometry and oscillations were not visible. The main difference was the geometry of the weld, at low speed the molten pool was significantly larger on the upper half visible as a large weld area. The large molten pool near the top did not occur at high welding speed even when the keyhole behaviour was exactly the same. The main interest area is the sharp fusion line near the middle of the weld, both cases shows similarities in the solidification lines.

The Light trap mode has two subtypes, narrow and wide. The keyhole redirects the light deeper while absorbing more of the incoming energy near the top when absorption on the keyhole front is compared to NT-mode. With wide light trap the large beam diameter at the surface caused the keyhole opening to be large when compared to NT-mode. The ratio between KH opening and the middle section diameters was above 1.8 with wide trap mode. This caused the keyhole to be a wide cone shape that also affected the weld geometry considerably. Figure 51 shows wide trap mode and the corresponding weld.

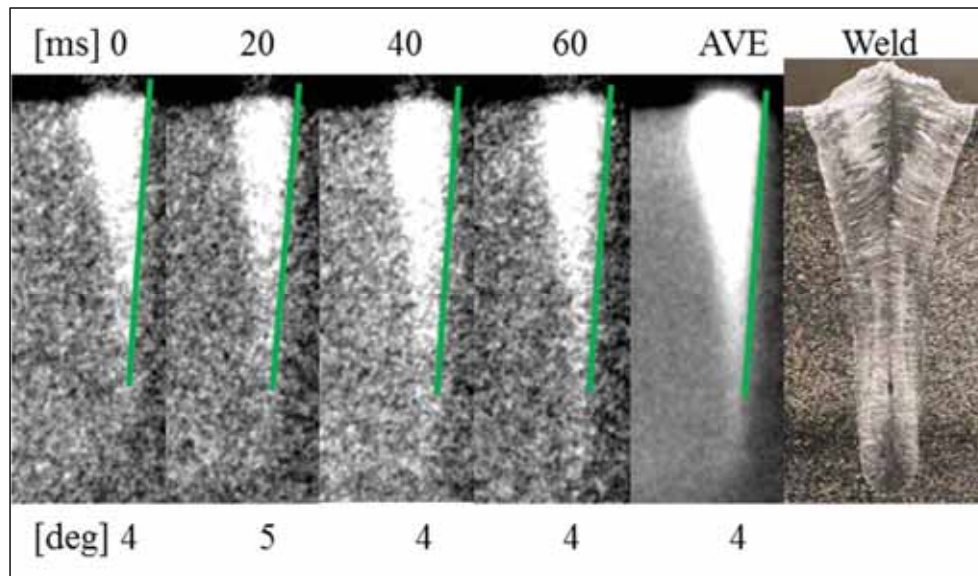


Figure 51. Wide trap. PP BOP, 2.0 m/min and -6.0 FPP.

With WT-mode the keyhole front wall angle was slightly larger when compared to the NT-mode. Still the increase in the front angle increased the absorption by changing the interaction behaviour of the beam and the molten wall, see the reflectivity graph figure 1, and this resulted in more energy on the upper half which changed the weld geometry. When the FPP changed down to -6.0 FPP the keyhole opening increased and changed the KH behaviour also causing the weld geometry to change. The main change was that the weld depth decreased and fusion line is smooth from top to bottom, eliminating the large molten pool near the upper half. The weld was large near the surface as in low speed narrow trap, but the middle area had smooth transition due to larger KH width in that specific area. This resulted in smooth fusion line throughout the whole depth. This keyhole mode was stable and welding process was also stable. The heating effect was larger on the surface, but more evenly distributed than in the narrow low speed light trap. The penetration in this mode was significantly smaller than in NT due to higher absorption on the upper half.

A transition zone was located between NT and WT but not defined as a separate mode due to having features of both narrow and wide trap modes, such as narrow keyhole from NT mode and smooth fusion line in weld depth from WT mode. The keyhole behaviour was similar as in all light trap modes, but the main difference was the weld middle section. The keyhole was larger only on the first quarter and this causes the weld to be slightly WT shape shown in figure 52. This mode had larger keyhole opening, but sufficient energy to form a deep vapour cavity and due to efficient self-focusing the keyhole started to get narrower near the top side compared to WT-mode, unlike WT-mode.

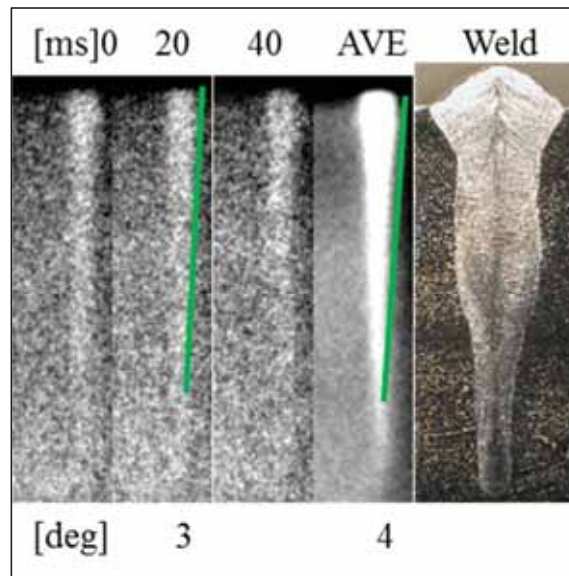


Figure 52. Trap mode, transition zone between wide and narrow. Bead on plate, 1.5 m/min and -4.0 FPP.

4.2.2 Cylinder (Keyhole C-mode)

The cylinder mode occurred at certain FPP range with certain welding speeds. The intensity range was from 1.3 to 1.6 W/mm² with 5.0 m/min and at 1.3 W/mm² with 4.0 m/min. With the laser and the optics used in this study the KH C-mode occurred at -5.0 and -6.0 FPP with welding speed of 5.0 m/min and -6.0 FPP with 4.0 m/min. The cylinder mode is presented in figure 53 and the molten front wall with a green line and the angle below each image. The blue arrows show the moving direction of the largest vapour volume.

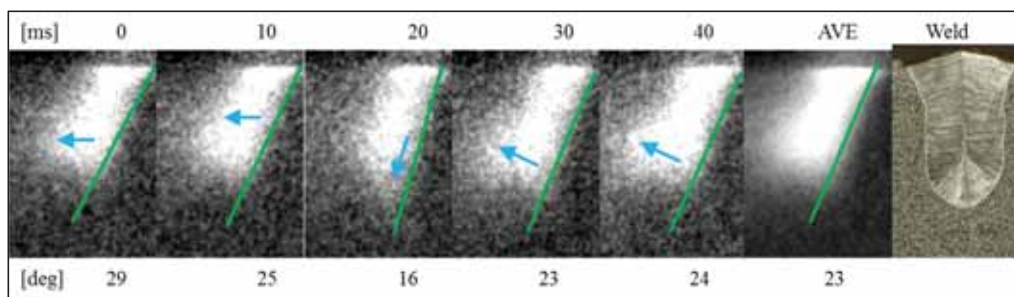


Figure 53. Shallow cylinder mode. PP BOP, 5.0 m/min and -6.0 FPP.

The features of the cylinder mode included a large keyhole front wall angle, the molten wall angle which increased absorption when compared to trap modes front wall angles of 1 to 4. The increased angle caused a peak in absorption and created more vapour near the sample surface, which in turn increased the keyhole volume near the top and formed a large keyhole.

These phenomena caused this keyhole mode to be shallow and can even form a small vapour cavity under the molten pool surface, a droplet shape. The keyhole in this mode was stable and the keyhole penetration was the same along the weld. When the angle was decreased to 16 degrees the keyhole slightly gets narrower but not noticeably deeper at 20 ms mark.

In figure 54 another example is shown in which the oscillations are slightly larger and the keyhole resembled wide trap mode. At 40 ms mark in the next figure the keyhole is steadily narrowing from the top and the front wall angle was only 10 degrees, still the absorption was high and the keyhole stayed in cylinder mode. Even with the oscillation the increased depth was negligible. At the 60 and 80 ms marks the keyhole is again completely in cylinder mode. This was close to the transition zone between trap and cylinder.

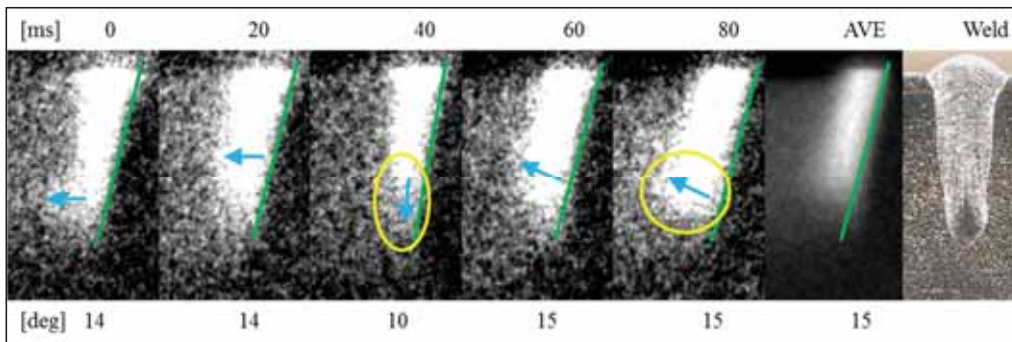


Figure 54. Shallow cylinder mode KH fluctuations. PP BOP, 5.0 m/min and -5.0 FPP.

4.2.3 Kaleidoscope (Keyhole K-mode)

Kaleidoscope mode is the most common stable mode for full penetration welding. In this mode, some of the laser beam's energy passed through the sample and the width of the keyhole stayed close to even width through the depth. The weld geometry is close to the keyhole geometry and the top side and the root side can even be the same width. Figure 55 shows an example of this keyhole mode, even width kaleidoscope (EK-mode).

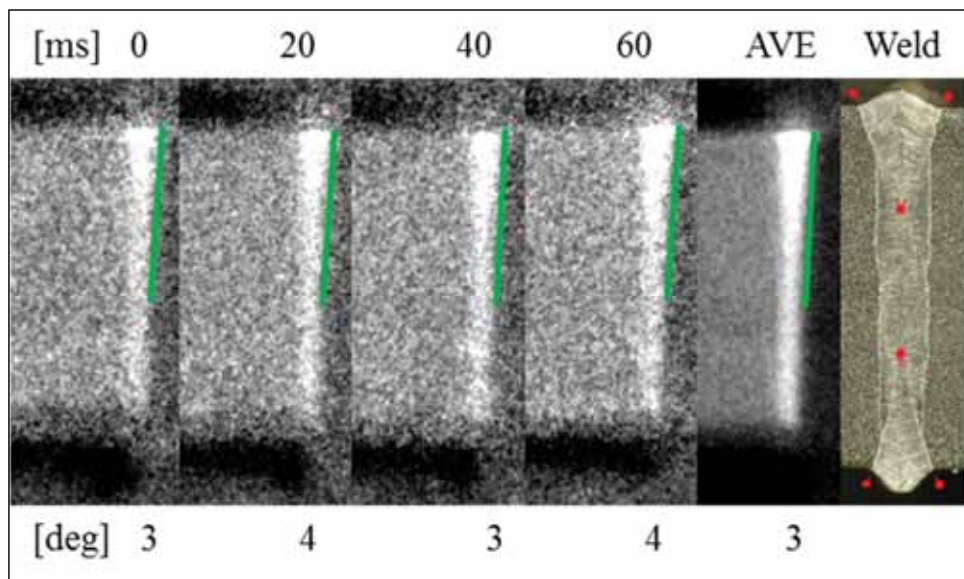


Figure 55. Kaleidoscope KH. FP BOP, 3.0 m/min and -2.0 FPP.

The front wall angle was small so the reflectivity was relatively large, redirecting the laser light effectively deeper into the material and some of it out of the root side. The basic keyhole behaviour differs from the trap mode by having an open bottom end, which caused larger root side relative to the top side when comparing to trap mode. From the weld point of view the differences are even greater, by having “twin top” geometry. This means that the root side has the same features as the top side, slightly larger surface width and similar solidification lines visible, shown as red circles with marks. The widening of the weld was caused by the sample edge, the air resulting in different heat transfer on the sample top and the root out of the weld area. It can be considered as an insulation, but no calculations of the heat transfer were performed. It can be concluded that the keyhole and the molten pool behaviour were very similar on both sides of the sample. The heat distribution along the weld depth was similar thus the top and the root sides have same heat input, which is beneficial for reducing the heat caused distortions.

Kaleidoscope can be also large opening (LK-mode), as shown in figure 56, which means that the keyhole opening is significantly larger compared to the root side opening. In this mode, the

laser energy was distributed mainly on the upper half which increased melting efficiency especially if the root side opening is extremely small. The keyhole in figure 50 is almost like a WT-mode, which in this case could be open cone-mode keyhole, which means that the efficiency is the same and the weld geometry is very similar with WT-mode. The LK-mode was an efficient and stable process, but the heat distribution was uneven along the weld depth. An even heat distribution is desirable for minimizing the heat caused distortions. On the other hand, if the most efficient process mode is used the lost energy is minimal due to reduced amount of laser beam energy that passes through the sample. The transition zone between EK- and LK-modes is relative large and the main differences are the ratio between the KH top and the bottom.

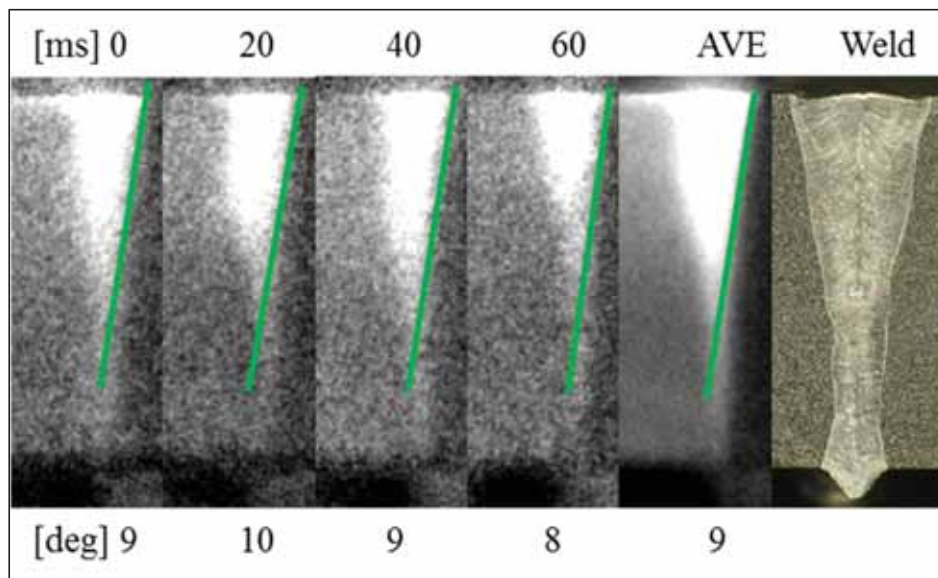


Figure 56. Full penetrating light trap mode, open cone mode. 4.9 mm sample bead on plate, 2.0 m/min and -6.0 FPP.

4.2.4 Modes table

The modes table was compiled from the x-ray data and is shown in table 6 for all joint types. In the graph the short names are used, NT (narrow trap), WT (wide trap), C (cylinder), EK (even width kaleidoscope) and LK (large opening kaleidoscope). The sub-modes are marked here to form a slightly more detailed table. The modes table presents, in simple form, the areas where each keyhole mode occurs. The blue areas are full penetration and other areas are partial penetration. The red area, C, is not desired except in joints and parts that are designed for cylinder mode keyhole and especially corresponding weld geometry. The grey areas are inconsistencies caused by technical problems in the data in question, for example corrupted data causing inconclusive image processing and analysis.

Table 6. Keyhole modes according to welding parameters.

PP BOP	Welding speed [m/min]						FP BOP	Welding speed [m/min]					
FPP [mm]	1.1	1.5	2.0	3.0	4.0	5.0	FPP	1.1	1.5	2.0	3.0	4.0	5.0
+2.0	NT	NT	NT	NT	NT	NT	+2.0	EK	EK	EK	EK	NT	NT
±0.0	Error	Error	NT	NT	NT	NT	±0.0	EK	EK	EK	EK	EK	NT
-2.0	NT	NT	NT	NT	NT	NT	-2.0	LK	LK	LK	LK	EK	NT
-4.0	NT	NT	WT	WT	WT	WT	-4.0	LK	LK	LK	LK	WT	NT
-5.0	NT	WT	WT	WT	WT	C	-5.0	LK	LK	LK	LK	WT	C
-6.0	WT	WT	WT	WT	C	C	-6.0	LK	LK	LK	LK	C	C

PP IBJ	Welding speed [m/min]						FP IBJ	Welding speed [m/min]					
FPP	1.1	1.5	2.0	3.0	4.0	5.0	FPP	1.1	1.5	2.0	3.0	4.0	5.0
+2.0	NT	NT	NT	NT	NT	NT	+2.0	EK	Error	EK	EK	EK	EK
±0.0	Error	Error	NT	NT	NT	NT	±0.0	EK	EK	EK	EK	EK	EK
-2.0	NT	NT	NT	NT	NT	NT	-2.0	EK	EK	EK	EK	EK	EK
-4.0	NT	NT	NT	WT	WT	WT	-4.0	LK	LK	LK	LK	LK	EK
-5.0	WT	NT	NT	WT	WT	WT	-5.0	LK	LK	LK	LK	LK	EK
-6.0	WT	WT	WT	WT	WT	C	-6.0	LK	LK	LK	LK	WT	C

The WT mode started to occur sooner with BOP due to the bevel in IBJ which changed the top side keyhole behaviour slightly. The effect of bevel can be seen also from -4.0 and -5.0 FPPs by allowing higher welding speeds to be in NT-mode. The bevel, in effect, lowered the surface location where the laser beam actually interacts with the surface allowing similar keyhole behaviour with larger FPPs below the surface. The keyhole is wide-mode when the ratio between the keyhole opening and the middle section of the keyhole is above 1.8. This also causes the weld to have smoother fusion line along the weld depth on the weld sides.

4.3 Tracer material and flow patterns in the molten pool

The parameter range for the tracer experiments was decided after the visual inspection of the previous weld sets, PPs and FPs. Three different welding speeds were tested, 1.0, 2.0 and 4.0 m/min and the laser power was kept constant at 5.0 kW as in all of the experiments. The FPP was -4.0 mm in each case and was selected based on the visual inspection of the welds without the tracer material. Two different types of tracers were used, fine tungsten powder of approximately 10 μm in diameter and 1 mm diameter 99.9 % molybdenum wire. Figure 57 shows the mixing depths of all tracer welds and the latter has the welds selected for flow pattern analysis.

The flow pattern analysis was performed to track the molten metal flow inside the molten pool. Both wire and powder tracers were tested and the welds were selected according to parameter range, to achieve results from several parameter sets. Partial penetration welds had also 40.0 mm thick EN 1.4301 samples in addition to 7.8 mm EN 1.4404 samples as in previous sets. Only powder tracer was used for 4.9 mm samples due to lack of samples at the time.

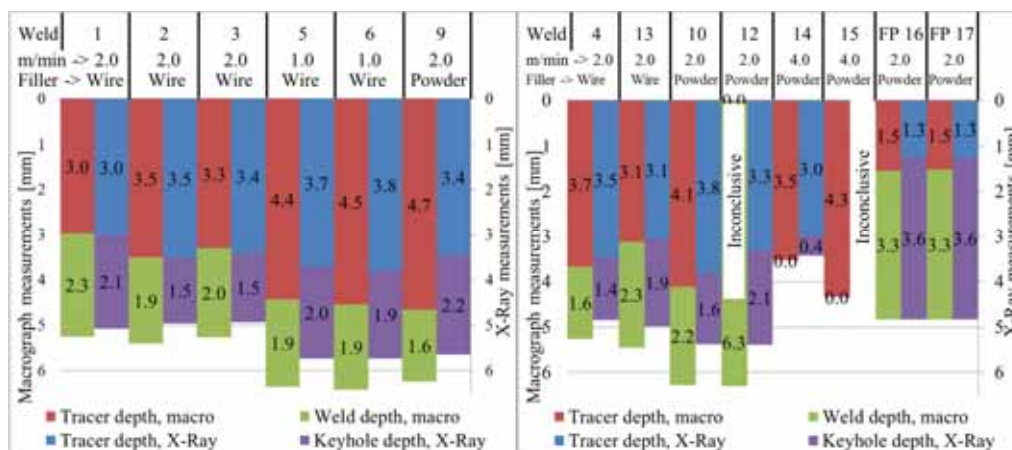


Figure 57. Weld, keyhole and tracer depths of tracer experiment welds.

The tracer was partially visible in the x-ray videos. The very bottom of the mixing depth can have only a small amount of particles and this would not be sufficient to cause a proper difference in the total mass attenuation coefficient (MAC). This effect can cause a slight inaccuracy between the x-ray and weld cross-section measurements. The tracer depth can be confirmed, in most cases, from the cross-section – x-ray comparison and flow patterns are visible in the x-ray videos. The average mixing depth was 60 % of the weld depth. The lowest mixing depth occurred with 4.9 mm thick samples when the process was full penetration welding. Some of the welds had inconclusive results and the mixing depth could not be determined properly. These welds are presented also in the appendices 15 and 16. The higher welding speed of 4.0 m/min resulted in very good mixing of the tracer according to macrograph

and also according to x-ray analysis. The PP IBJ at welding speed of 4.0 m/min x-ray measurement was inconclusive due to unknown imaging issues. The macro graphs showed full mixing of the tracer into the weld.

4.3.1 Tracer wire with partial penetration

The keyhole is visible as a light area below the millisecond (ms) value and tracer material, molybdenum wire, as a dark area on the left side in figure 58 that shows two 7.8 mm sample thickness welds, BOP upper and IBJ lower. The welding direction was on to the right. The tracer melted, but still the MAC (Mass Attenuation Coefficient) was different when comparing to the base material. The difference allows seeing the molten pool and the movements in it. In the molten pool there were no sufficiently large particles that would be visible as separate particles and the tracer is mixed well into the molten pool. The main areas to observe are the depth and the main flow path and the location of the melted tracer, as red arrows, and bubble flow direction, as blue arrows if present. The wire was stationary on the work piece surface thus resulting in stable tracer wire addition.

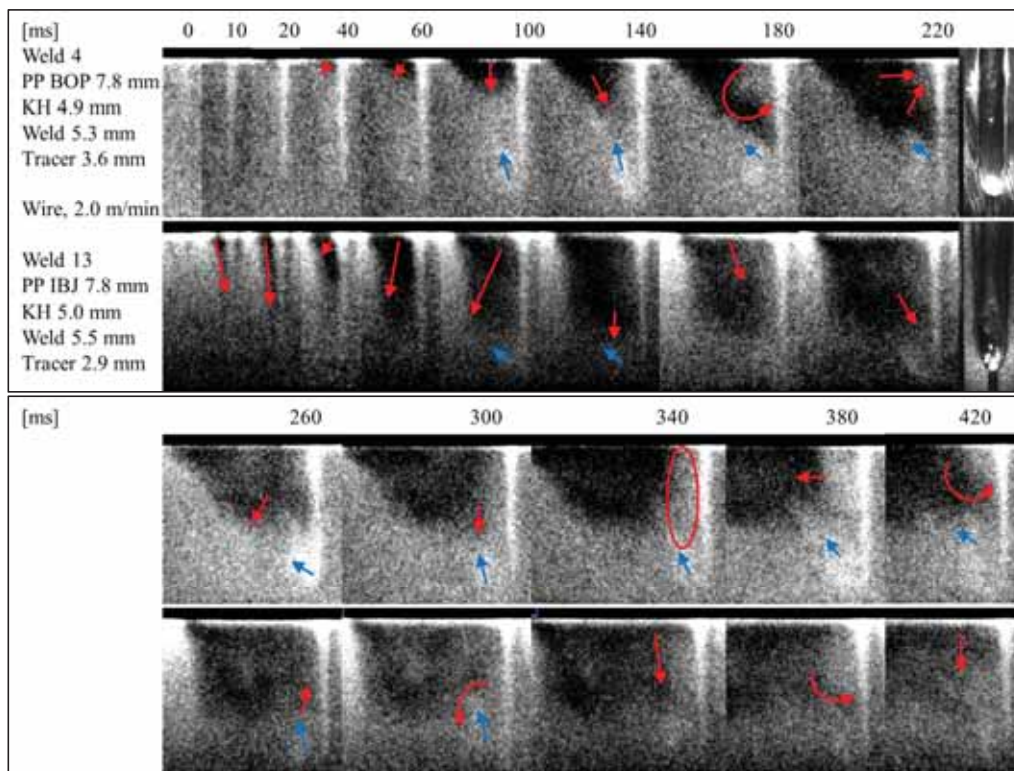


Figure 58. Tracer tests 4 and 13. Red arrows - molten metal flow direction and blue arrows - bubble flow direction.

The molten flow was stronger and occurred sooner with IBJ and achieved deeper penetration in the beginning. The stabilisation of the process changed the molten metal behaviour between BOP and IBJ. In the BOP weld, the tracer was mixed only slightly deeper on average. For IBJ, the mixing was slightly unstable and the mixing percent was 57 % of the penetration depth. The mixing percent for BOP was 69 % on average according to the weld cross sections. The main molten flow was from behind of the KH downwards and then started to circulate in the molten pool. For BOP the circulation was closer to the top and for IBJ the circulation started later in the process and was located deeper in the molten pool. The circulation direction was similar in both cases.

The circulation and surface mixing were periodic and these two phenomena were connected. The so called spiking of the molten metal towards the bottom of the molten pool was caused by this periodic circulation. Blue arrows show bubble flow but there were no pores visible in the solidification front and solid areas. On the other hand the solidification front was not clearly visible in these x-ray videos. The metal vapour inside the bubble creates pressure and when the vapour condenses onto the bubble walls, the bubble collapses and disappears completely.

The difference in the welding depth was 5.2 vs. 5.6 mm in BOP and IBJ respectively. Similar mixing depths could be noticed from both macrographs and from X-ray videos and also the molten pool size and weld geometry were similar for both cases (BOP and IBJ). Images of all welds are presented in appendices 15 and 16. The molten pool size and the weld geometry were similar in both cases. The bead reinforcement was slightly smaller for IBJ due to top side bevel of 0.3 mm². The tracer increased the amount of material the laser beam had to penetrate and the difference in penetration was significant. The keyhole depths were 5.5 vs. 4.9 mm for BOP without tracer and with tracer respectively. IBJ difference was 5.6 vs. 5.0 mm, without tracer and with tracer respectively. The weld depths were 6.0 vs. 5.3 mm for BOP, without tracer and tracer respectively and with IBJ 6.2 vs. 5.5 mm.

The main differences between the joints were that the IBJ seemed to mix deeper momentarily but the average mixing depth was deeper for BOP. The location of the circulation was deeper with IBJ and this caused the deeper mixing spikes for IBJ. The keyhole was stable in both cases.

4.3.2 Tracer powder with full penetration

The second set of tracer experiments consisted of 4.9 mm sample thickness FP welds, as shown in figure 59. The tracer was tungsten powder spread into a 1.0 mm thick layer above the sample surface. It was assumed that large vapour pressure from the keyhole might affect the powder behaviour, and therefore the same laser parameters were also tested with PP. The high speed top side videos showed that part of the tungsten particles are pushed away from the keyhole to all directions.

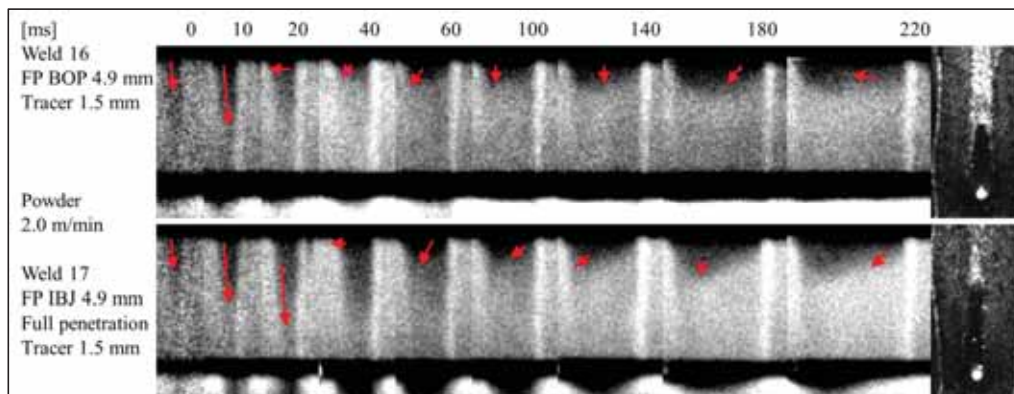


Figure 59. Tracer powder flow with 4.9 mm sample thickness.

The keyhole was penetrating the sample completely forming a full penetration weld. The tracer mixing with powder and 4.9 mm sample thickness was significantly shallower than with tracer wire and 7.8 mm samples. The flow direction was very straight forward, from behind of the keyhole downwards and slightly backwards due to sample movement. There were no circular movements of the tracer detected and the mixing was stable. In the beginning the flow downwards was extremely strong and almost achieved the bottom of the sample. After 100 ms the strong flow downwards towards the root side seized and mixing occurred only in the first third of the molten pool depth.

4.3.3 Tracer powder with partial penetration

To compare FP and PP welds with powder tracer and the effect of vapour pressure from the keyhole to tracer powder was tested by performing both welds with the same laser parameters. The PP powder welds with 7.8 mm sample thickness are presented in figure 60.

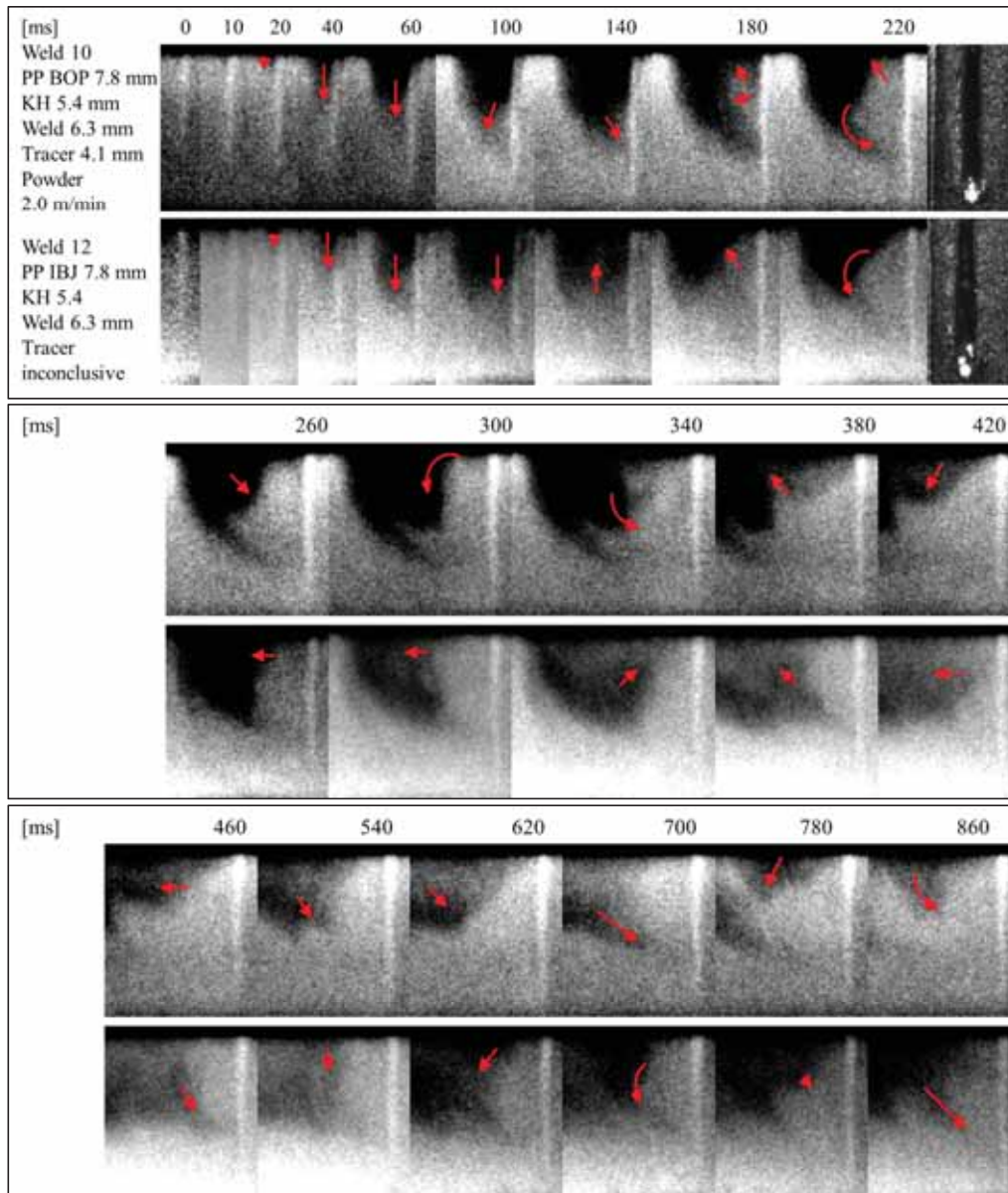


Figure 60. 7.8 mm sample, powder tracer.

As shown in previous figure, the tracer flow was similar compared to wire experiments and the main issue was the slightly instable tracer input into the molten pool behind the keyhole. The powder tracer got into the molten pool from the same location as the wire, just behind the keyhole. The flow pattern was relatively similar with both tracer types; the circulation was close to the same location, relatively close to the surface with BOP and slightly deeper with IBJ. In this case the IBJ samples also showed a slight circulation near the surface but the periodic circulation was located deeper. With IBJ the molten metal circulation was located deeper inside the molten pool as in the case of tracer wire. The powder experiment showed slightly straighter molten metal flow spiking, but also similar circulation. The frequency of the spiking and circulation was not sufficient to achieve 100 % mixing in the mixing depth, so there were “tracer spikes” shown in the x-ray videos.

The main differences compared to wire experiments were that the tracer mixing in to the molten pool was not as stable with powder. This caused slightly uneven mixing, but it was not visible in the weld cross sections. The tracer mixing depth with IBJ from weld cross section (weld 12) was inconclusive, but it seemed that it had full mixing. The x-ray videos did not show full mixing, but showed large momentary spiking of the tracer.

4.3.4 High speed partial penetration

High speed welding was also tested and the tracer flow is shown in figure 61. The figure shows the tracer flow direction from the start and also later in the process. The last single image marked 990 ms shows the main flow pattern of the tracer from phase I to phase III. The average x-ray image has a mark of the keyhole front angle which was 2 degrees.

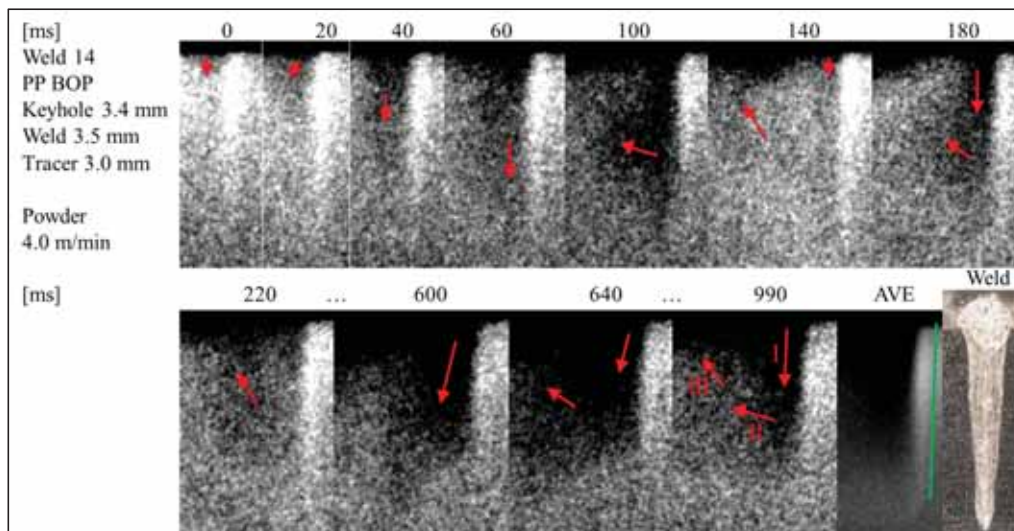


Figure 61. Welding speed 4.0 m/min PP BOP tracer powder flow pattern.

The tracer flow was through the whole depth of the weld during momentary periodic phase, marked phase I. In this phase the tracer flow was extremely strong from the backside of the keyhole to downwards and this took the tracer deep into the molten pool. In the phase II the tracer started to move backwards and in the last phase III, the tracer movement was upwards, but no forward movement could be seen. With slow welding speeds there were forward movement, so the tracer was moving faster than the welding speed to the welding direction. With high welding speed the tracer flow was simpler.

4.3.5 Random images and averages

Figure 62 shows single images of each welding process from the middle of the weld length to present a random location mixing of the tracer. Also x-ray video minimum image intensity values (minimum pixel grey value) are shown on the right side, this shows the average mixing depth of the tracer into the molten pool.

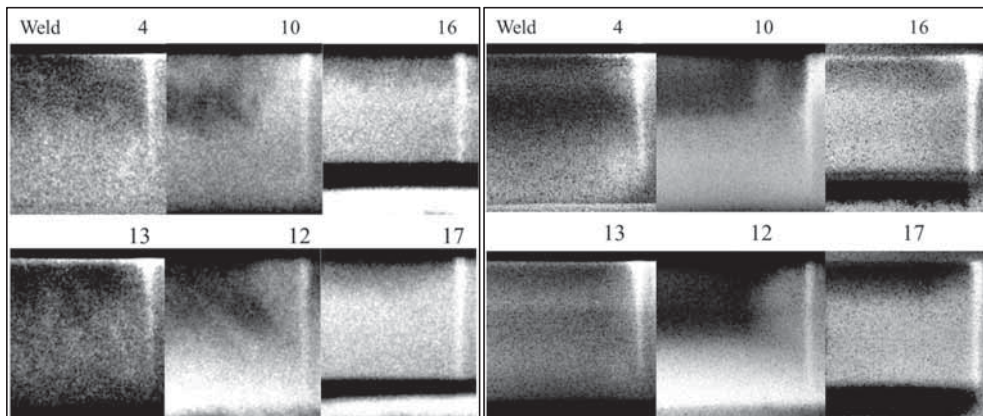


Figure 62. Left box presents single frames from a middle of the welding process of numbered tracer welds and the right box presents the minimum pixel intensity values of numbered welds.

This shows that the molten flow with IBJ oscillates slightly more, but on average the mixing depth is similar. The image contrast settings affects the visibility of features, but in this case the contrast was automatically adjusted in that way that the reliability was not affected. With powder tracer the mixing seemed to be slightly stronger with IBJ and was visible in minimum intensity images on welds 12 and 17.

4.4 Melting efficiency and filling capability

The weld geometry was averaged from two cross-sections from random locations for both PP and FP. The PP cross-sections were taken near the middle part, but further from each other than the FP welds and from a random location that had a stable welding process phase. Weld geometry was compared with the keyhole geometry and those are shown in section 4.1 Keyhole and weld geometry and melting efficiency and filling capability are presented in this section.

The melting efficiencies were calculated for each weld and are shown in figure 63. The welds having one edge melted, when the molten pool reaches the edge of the sample melting the whole edge which affects the molten pool behaviour, were removed from the graphs due to abnormal molten pool behaviour. The same rule applies here also as in other graphs that the partial penetration welds with 4.9 mm samples were removed due 4.9 mm samples were designed to have full penetration welding process, marked as FP. The melting efficiency is a value of how many cubic mm is possible to melt with 1 kJ into the process.

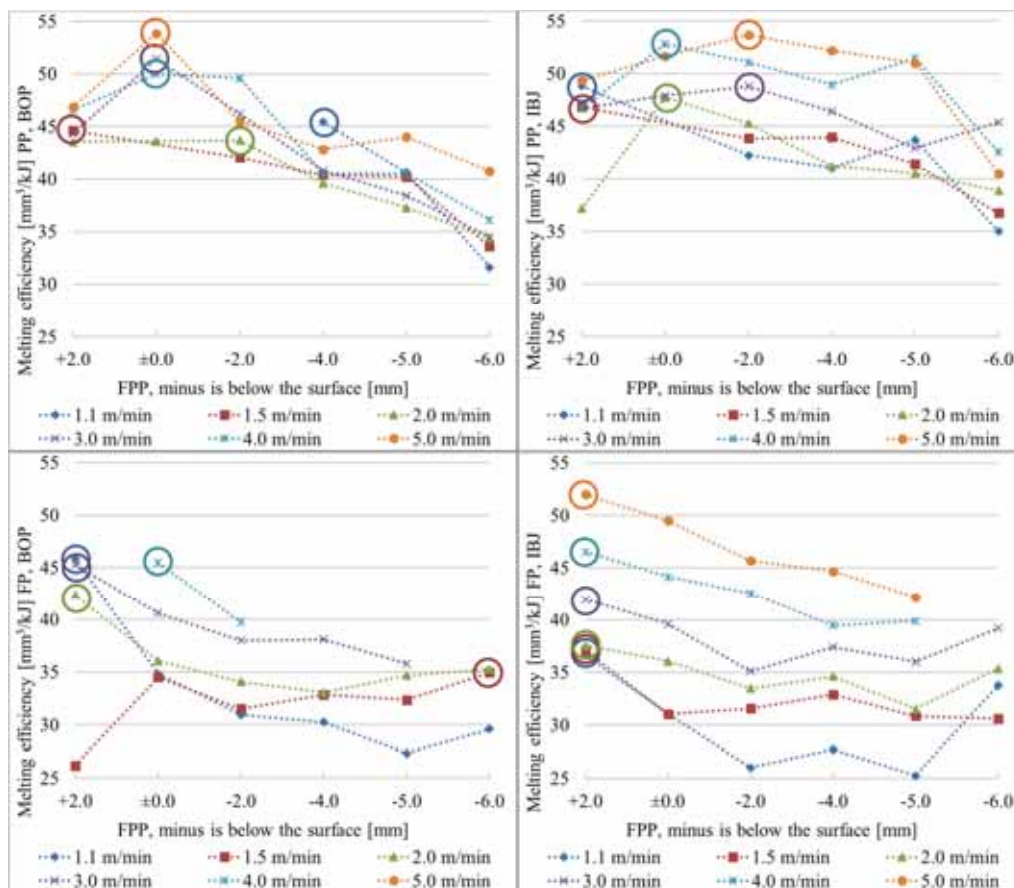


Figure 63. Melting efficiency graphs.

It can be noticed from the figure 57 that as the portion of the laser energy passes through the keyhole during full penetration welding, the melting efficiency drops. For partial penetration, the melting efficiency was mainly connected to keyhole penetration depth at high welding speeds of 2.0 to 5.0 m/min. The deeper the keyhole the higher the melting efficiency was in this region. The slower welding speeds of 1.1 and 1.5 m/min resulted in a slightly different behaviour and showed that at slow welding speeds with PP BOP the keyhole and the molten pool behaviour near the surface affects the most, especially with 1.5 m/min. The absorption changed when the incoming beam angle changed and optimal absorption angle was outwards at the sample surface. The change in the incoming angle increased the absorption and also increased the weld width on the uppermost third of the weld. The +2.0 FPP might not be the most optimal parameter combination penetration wise, but resulted mainly in the highest efficiencies.

For PP IBJ the trend was similar as for PP BOP – the welding speed of 2.0 m/min and above resulted in the highest melting efficiencies and the deepest penetrations. Slower welding speeds (1.1 and 1.5 m/min) resulted in the highest melting efficiencies at +2.0 FPP, almost at the lowest penetration depth. This also shows that the large keyhole and large molten pool near the surface increases efficiency, meaning that the absorption is higher due to larger keyhole width in upper half with +2.0 FPP especially when comparing to -2.0 FPP.

The filling capability means how well a certain laser parameter combination can fill up the bevel and still form bead reinforcement. Filling of the weld bead is important due to possible bevel and inaccuracies caused by cutting processes in general. Inaccuracies and defects can be caused for example by impurities in the optics, vibrations, accumulating wear of the mechanical systems or use of cutting parameters which are not optimal. Small defects are not always noticed and a small bevel usually is not a problem, especially if the plate is going to be welded with a conventional welding process, such as GMA-welding which has filler wire. Figure 64 shows bead reinforcements for BOP and filling capability for IBJ for both samples thicknesses.

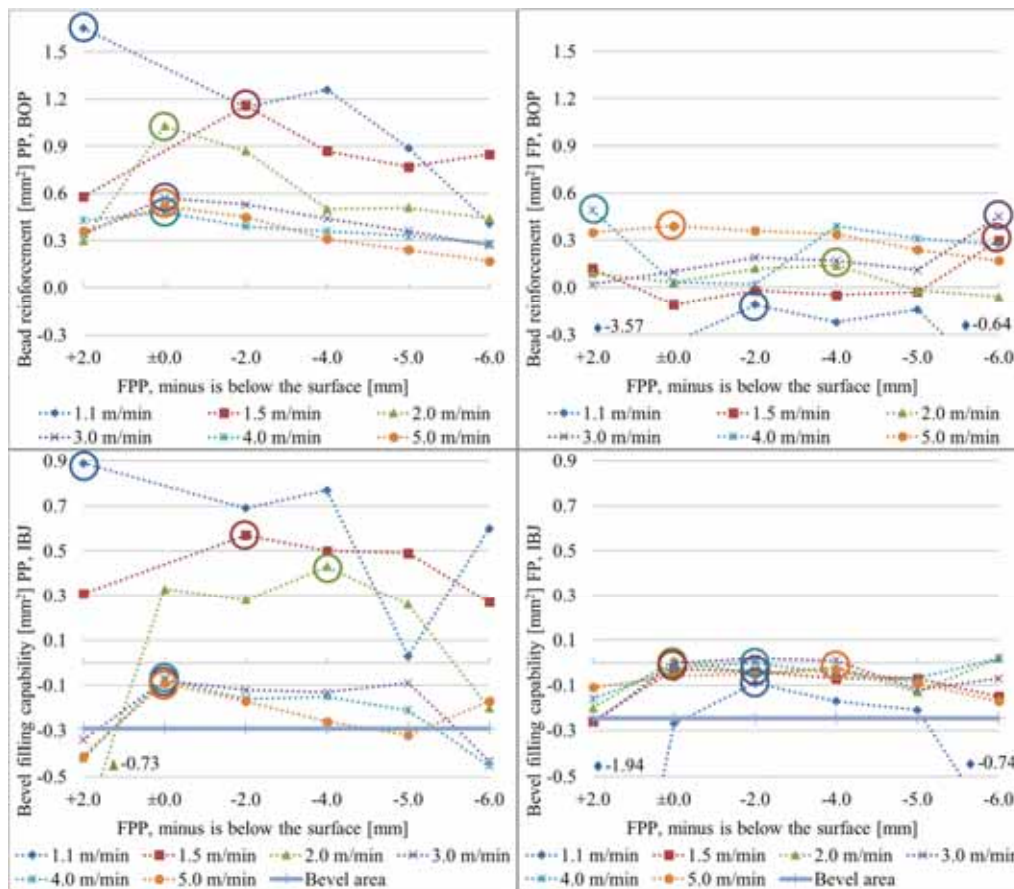


Figure 64. Bead reinforcement with bead on plates and bevel filling capability for butt joints.

PP BOP showed sufficient bead reinforcement as there was no bevel and the weld cannot sag due to partial penetration. The only effect that could cause underfilled bead, in this case, would be excessive spattering. However, as the welding parameters resulted in relatively stable welding processes, excessive spattering did not occur. The reason for the largest bead reinforcement with 1.1 m/min welding speed and +2.0 FPP, was the edge melt. The molten pool reached the edge of the sample and this caused part of the sample edge to melt. The air around the sample conducts heat significantly slower and less efficiently and the heat is directed towards the sample bottom at the side. This slightly increased the molten pool size for the time it was on the edge. The same occurred with 1.1 m/min and -2.0 FPP. The bead area was larger with +2.0 FPP which also suggests that larger portion of the laser beam's energy was absorbed by the top part of the keyhole. This effect also increased the efficiency due to increased molten pool. In these two cases the process was efficient, but not favoured due to abnormal molten pool behaviour with this sample width, however, with larger sample it is not a problem. On the other hand, the smallest bead reinforcement with 1.1 m/min was caused by full penetrating weld, this caused the weld to drop slightly.

Three of the FP BOP 1.1 m/min welds cracked from the centre, but the cracked area was not taken into the bead reinforcement and filling capability measurements. As with the PP, FP samples showed sufficient bead reinforcement and no significant spattering occurred that could have caused underfilling at welding speeds above 1.5 m/min. For FP BOP welds, the bead reinforcement graph did not show any significant trend line of the effect of FPP.

IBJs showed similar behaviour at high welding speeds with PP and FP types due to similar bevel. In the lower welding speed range the behaviour was different, especially the molten pool on the upper half or third was significantly larger than with the high speed. PP IBJ showed very good bevel filling capability up to 2.0 m/min and slightly worse at 3.0 m/min and above. The molten pool had time to grow with low speeds resulting in more molten metal on the top, this with the increased heat input brought the material from the bottom to the surface via the periodic circulation.

With optimal parameter combinations the filling capability was sufficient with all welding speeds. Achievable filling capability at high welding speed was -0.1 mm^2 with 3.0, 4.0 and 5.0 m/min at ± 0.0 FPP, this means that these laser parameters filled the bevel 0.2 mm^2 or 0.1 mm^2 depending on the sample thickness. -0.1 mm^2 underfilling is negligible and classifies in stringent B-quality. The FP IBJ mainly did not show proper filling (bead reinforcement) with slow welding speeds, but the optimal FPP range was from ± 0.0 to -4.0 FPP, in which all welding speeds achieved underfilling less than 0.1 mm^2 or complete filling with welding speeds of 2.0, 3.0 and 4.0 m/min.

5 Discussion

5.1 Keyhole geometry and efficiency

The keyhole depth mainly determines the weld penetration depth. The measurements performed in this thesis had two assumptions and one of them was the keyhole depth measurement method. The keyhole was assumed to end on the location where the keyhole centreline crossed the intensity drop of the x-ray beam, in some cases some bending occurred and if the bending was clearly visible it was taken into account. This method is relatively accurate, but the keyhole tip is very likely extremely narrow and this, probably, was not visible in the x-ray videos or images due to image noise. The possible problem in this video- and image processing method is the human factor. All of the measurements were based on the manually outlined keyhole side view geometry. The contrast difference between the solid and the liquid versus the vapour was not sufficient to perform automatic outlining of the side view. This human factor might affect the results, but in most cases, for example when comparing the keyhole depths on different joint types, there were clear trend lines and the differences in most cases were significant. The keyhole depth was also compared with the weld depth and this showed relatively good trend lines also. The keyhole vs weld depth has been studied before and the keyhole seemed to be very close to the weld depth. The outlines were drawn on average images in which the signal-to-noise ratio is higher. This does not reduce the inaccuracy, but does result in valid comparison. The main point in the keyhole volume study was to ignore separate and exact keyhole values and look at the complete comparison between all parameter combinations.

The geometry of the keyhole changed when the laser parameters were modified and the FPP had a connection with the keyhole opening and the volume. The larger keyhole opening resulted in larger keyhole volume and this also affects the keyhole front wall area and the vaporisation mass. If the laser beam had insufficient power to vaporise the mass to form a deep vapour cavity the result was an inclination of the keyhole front. This inclination increases absorption on the upper half reducing reflections deeper into the material. The beam incoming angle also slightly changed the interaction angle and in some cases must be taken into account if measuring or calculating exact absorption values in the future.

There was also a possibility of humps on the keyhole wall which can affect the interaction angle. In the x-ray videos, hump like features can be seen in which the keyhole front wall is not straight, but more like a slightly wavy irregular surface. The keyhole is a 3-dimensional structure and likely a rotational symmetric and the x-ray images and videos are constructed of this 3-dimensional form into a 2-dimensional image. The waves, humps on the keyhole wall affects, even if they are on the side and not on the front wall. This is more affecting with the trap mode keyhole due to keyhole C-modes larger interaction area on the front. It seems that T- and K-modes absorption behaviour is through the wavy surface and not through the front wall average angle. One must remember that this discussion is mainly about the first interaction area

and the multiple reflections inside the keyhole were not taken into account due to lack of beam tracing calculations inside the keyhole. The front wall that was visible in the x-ray images was very small due to this rotational symmetric form and due to this the humps might be easier to see but the vapour thickness was small in the x-ray beam path on this front wall and this reduced the visibility. To know the complete set of interaction angles inside the keyhole a beam tracing calculations must be performed, but it was not possible during this study.

The keyhole was assumed to be rotational symmetric in depth wise and on the second calculations a keyhole opening geometry was used throughout and this affected the keyhole geometry. Another assumption was the average keyhole geometry, which does affect the time resolution and this method should not be used with very fluctuating keyholes. If the keyhole fluctuates strongly then the weld is irregular, which is not desired generally due to keyhole mode and geometry mainly determining the weld geometry. Most of the keyholes were stable and these stable keyholes were taken into the keyhole mode analysis. The differences in the KH volumes between the circular and KH opening geometry were partly significant and partly the same due to almost circular KH opening. The main differences were with the PP IBJ and with slow welding speeds.

The beam diameter mainly determined the keyhole opening and this determined mainly the keyhole volume, the vapour volume. Within these experiments the keyhole volume was calculated with a circular geometry. This assumption is critical, but only trend lines were observed and not each individual volume value. It is not possible to achieve an accurate 3D-geometry of the keyhole with one x-ray system, additional systems are required to achieve the complete 3D-geometry without any assumptions. From the x-ray videos it was not possible to measure what the keyhole geometry was below the surface in the x-ray beam path direction and this had to be assumed.

The keyhole opening geometry had an effect on the second calculations of the keyhole volume. The circularity was considered and a somewhat oval shape was used. The main problem in some of the keyhole opening measurements was the fact that the camera was in an angle and if there was no molten front on the sample top the camera also showed the inside of the keyhole visible as a keyhole opening. This was considered and removed in cases it was noticeable.

The keyhole depth divided by the keyhole volume resulted in interesting trend, each welding speed resulted in the highest depth to volume ratio at -2.0 FPP. This was also the main area for the deepest penetrations at most of the welding speeds. This might point out the most efficient reflection area, in which the penetration is at its highest. Even though the -2.0 FPP resulted in highest depth per volume ratios, the smallest interaction angles occurred with ± 0.0 FPP. This points out that the incoming angle probably affected the reflections due to beam incoming angle is inwards with -2.0 FPP and relatively 90 degrees to the surface with ± 0.0 FPP. Which means that if the keyhole inclination angle is near 0 degrees the laser beam incoming angle is parallel

to the keyhole walls. ± 0.0 FPP also resulted in the deepest penetration at several high welding speed parameter combinations and to the smallest keyhole front inclination angles. This suggests that the FPP on the surface is optimal for reflectivity and penetration at higher welding speeds. On the other hand, if the reflections are highest, what energy vaporises the material on the upper half of the keyhole? The reflectivity was high due to the beam being almost parallel to the keyhole front, but this is the case of open keyhole, not during the formation of the keyhole. The explanation is the wavy surface that affects the interaction angle and vaporises the material throughout the depth while other parts of the KH wall reflects the beam strongly downwards. This might be explained partly by the vapour pressure from the keyhole bottom half that pushed high temperature particles also upwards. Also the material is directed towards the beam by the movement of the beam vaporising it in the beams way. This occurs near the sample surface and along the keyhole depth on the front, as moving humps that are visible as irregularity on the keyhole front wall. Due to the high intensity of the beam, a relatively small part of the beam's energy can vaporise the steel due to high laser power allowing deep penetration.

For IBJ the effect is slightly different due to the bevel and FPPs below the sample surface resulted in deeper penetration due to different behaviour of the molten pool on the surface. This is probably caused by the decreased amount of vaporised mass on the surface.

Although the ± 0.0 to -2.0 FPP area was the most efficient laser parameter combination when taking into account the penetration capability, the melting efficiency was not at its highest. Likely the efficiency is dropped due to energy taken by the vaporisation process creating a deep vapour cavity. This partly suggests that there might be a significant amount of high temperature metal vapour formation inside the keyhole that is pushed upwards from the keyhole bottom half. The 1030 nm wavelength does not interact considerably with plasma unless the amount of photons is sufficient that photon - free electron interaction causes increased plasma formation. With optimal reflection angles between the laser beam and the molten wall, between 0 to 5 degrees, the laser beam's intensity on the bottom half increases while increasing the possibility of photon - free electron interaction that creates more plasma. Plasma has generally very high temperatures and if formed this could increase vaporisation of the molten wall on the upper half of the keyhole through radiation and free electron collision. Although it is unlikely that plasma formation occurs. One of the affecting phenomena could be refraction of photons in the dense high temperature metal vapour changing slightly the beam path along the keyhole depth, but this is not clearly visible as changed keyhole form, the KH remains as trap mode in these high intensity cases. It might be that the vapour pressure in this case is considerable and the pressure takes particles out of the keyhole at high rate. Plausible explanation for reduced efficiency could be that these particles also absorb a part of the laser power. Due to these effects the penetration is deep but the total melting efficiency is slightly dropped.

The highest melting efficiencies occurred near ± 0.0 FPP with PP BOP, $+2.0$ FPP with PP IBJ, near ± 0.0 FPP with FP BOP and at $+2.0$ FPP with FP IBJ. With FP IBJ $+2.0$ FPP melting

efficiency is likely caused by the incoming angle of the beam combined with the bevel. Another issue is the depth of the bevel that partly lowers the surface – beam interaction location allowing larger FPPs below the surface to achieve similar results when comparing to BOP without a bevel. Even though this could be the case, the melting efficiency acts slightly differently due to the bevel in IBJ.

FP BOP also resulted in highest efficiency with +2.0 FPP in few cases. +2.0 FPP should have large amount of multiple reflections due to the beam travel direction is outwards at the surface. This shows that the melting efficiency and keyhole process efficiency, the penetration per volume, are not directly connected, but affects maximum penetration and the efficiency together.

5.2 Flow patterns

Filler wire is a crucial addition in many welding processes and this applies also for the laser welding for some applications that must have additional material for the weld or to fill a groove. The mixing depth of the filler is of high importance and must be known. It is also beneficial if filler flow and mixing is known due to question of stability of the mixing. In the laser welding process, as shown, the mixing was mainly not stable and some spiking movements occurred, except with full penetration welding. This difference was considerable and mixing depth was only half with FP when compared to PP.

In the case of PP, the circulation is located on the upper half and rotates counter clockwise periodically. This might be explained by combination of the keyhole and the phenomena on the surface. It can be seen that the molten metal flows on the molten pool surface, which might be increased by the vaporisation pressure inside the keyhole and especially on the keyhole opening in addition to the main cause of increased molten metal flow on the keyhole sides. This increase would be caused by the fact that the area in which the molten metal flows is smaller than behind the keyhole and when the same amount of volume must move the flow speed would be higher on the smaller area, the keyhole sides. The pressure from the keyhole also likely pushed the molten metal backwards creating slightly more flow. This same flow affects also deeper inside the molten pool creating same directional flow. Due to the molten pool geometry, the stable periodic flow is limited on the “larger” area of the molten pool in the case of T-mode keyhole.

In the case of full penetration the tracer flow was limited on the uppermost third. In the first states of the process when the keyhole starts to penetrate the material, the tracer mixes very deep into the molten pool. After the first phase is over and the keyhole is open on the root side and molten metal movements occurs on both sides preventing the filler mixing deeper into the molten pool due to one sided filler input.

Another interesting issue is the high welding speed mixing, which penetrated through the weld depth on the whole welding length. The reason could be the molten metal behaviour due to high

moving speed. The molten metal is pushed strongly downwards and this also takes the tracer deep into the molten pool. This might be caused by the extremely high molten metal flow on the sides of the keyhole which creates a fast flow behind the keyhole also directing flow downwards. The different flow between low and high welding speeds was not connected to keyhole geometry. The keyhole was NT-mode in the 4.0 m/min tracer experiment and the keyhole was stable. The weld geometry also showed the same behaviour as without the tracer and narrow trap mode.

5.3 Keyhole modes

Three main types of keyhole modes were detected, trap mode (T-mode), cylinder mode (C-mode) and kaleidoscope (K-mode). Different keyhole modes have not been defined in the literature before by other authors. Two of these main modes have sub-modes, narrow and wide trap (NT- and WT-modes) and kaleidoscope has even width and large opening kaleidoscopes (EK- and LK-modes). NT-mode has different molten pool behaviour at low and high welding speeds but the keyhole itself acts similarly. Each of these modes have their own stable characteristics, which affects the keyhole geometry and also the molten pool behaviour and the geometry of the weld. The changes between the modes were laser parameter dependent and likely connected to for example keyhole opening geometry, reflectivity factor of the molten front and laser power.

In the case of the wide trap keyhole, the beam diameter at the surface was large and also the keyhole opening. This did not necessarily, or likely, reduce the total vaporisation rate but increased the vaporisation mass. This caused the keyhole volume to be larger and this changed the keyhole front angle due to insufficient vaporisation rate for that particular mass. When the angle increased the absorption increased and larger portion of the laser energy was absorbed in the upper half reducing the portion that was redirected deeper into the material. Overall this effect reduced penetration which was dependent on the welding speed, at low welding speeds the process had more time to vaporise the material and the keyhole opening did not have that large effect. At high welding speeds the process was more vulnerable to “amount of mass”-effects, which in this case caused the keyhole tilting.

The vaporised metal has particles which also absorb and reflect the photons of the laser beam. This might be plasma in some cases, but single photon absorption at 1 μm wavelength does not ionise the metal, multiphoton absorption can ionise the metal but the occurrence is unknown. It cannot be confirmed by the experiments and the results of this thesis whether plasma did or did not occur. Plasma or metal vapour particle absorption might affect the energy distribution along the keyhole depth and this could bring more heat on the top half. The effects of these phenomena are unknown and so are their possible effects on the keyhole, its behaviour and absorption in the metal vapour.

In the narrow trap mode, a very small angle was formed on the molten front, the keyhole front wall and this reflects the laser beam efficiently deeper into the material. The small angle was partly caused by the small diameter of the beam and high intensity of the beam. The absorption on the molten front was likely relatively small and similar throughout the whole depth, creating metal vapour from the keyhole front wall at steady rate. Low and high speed trap modes mainly acted similarly, but the molten flow was different. The slow welding speed molten pool did have more heat input on the upper half. The surrounding air has significantly lower heat transfer than the metal and this likely formed an insulation on the sample surface. This was a likely the phenomenon that increases the molten pool size on the surface especially with slow welding speeds. The convection difference was visible with the tracer experiments, at slow welding speed the molten metal flow was stronger increasing the effect of convection on the upper half via circular molten metal movement.

One additional factor was the vaporisation mass, the volume the laser beams energy had to vaporise to form the keyhole. It could've been possible that the keyhole was not circular below the surface and the current assumption might cause inaccuracy. The keyhole geometry below the surface affects the vaporisation mass by possible changes in the keyhole width. The difference between trap mode and cylinder mode occurred at FPPs at far below the surface, with a large beam diameter at the surface of above 600 - 700 μm , slightly depending on the welding speed and the joint type, this increased the width of the keyhole and the vaporisation mass, the amount of metal that needs to be vaporised. The vaporisation rate might be approximately the same in all cases, but the vaporisation mass makes the differences. The vaporisation mass was not calculated but could be included in the further studies.

The higher the welding speed the lower the penetration, but the vaporisation rate could've been the same and evenly distributed along the keyhole walls. This was the case especially with NT-mode when the keyhole opening was small and the intensity high which was sufficient to form NT-mode even with high welding speeds. With WT-mode the mass to be vaporised caused the cylinder mode at very high welding speeds of 5.0 m/min. In these cases the phenomena are probably the same, but the intensity and the "amount of mass"-effect caused the differences.

5.4 General

All these aspects are connected to each other and some assumptions were made during the analysis which might had an effect on the results. The assumptions likely did not have an effect on the keyhole mode analysis due to clear differences on the keyhole behaviour and due to the fact that the calculated numerical values such as volume did not have an effect on the keyhole mode analysis. The risk of assumptions being wrong was considered small and separate values were not analysed individually, but rather in groups. The laser parameters determined the geometry, which affected the keyhole mode, which affected the weld geometry which all mainly depended on the welding speed.

Spatter is a problem in some applications, but it is not defined in standards and is application dependent. Most of the welds had some spatter, but also surface spatter free welds was possible to achieve. The most of the spatter formed on the root side with full penetration welds. The topic of spatter formation and prevention on the root side very likely requires other observation methods and analysis tools. The spatter formation was not clearly visible in the x-ray videos and due to limitations of the fixtures it was not possible to film the root side. Filming of the root side would have the possibility to see the locations in which the spatter detaches from the molten pool. This study had only minor concentration on the spatter due to lack of visibility of the root side due to fixture and the selected observation methods. Spatter free surfaces were achieved with all penetration and joint types but spatter formation and cause requires further studies and could not be covered in this thesis due to lack of imaging of the root side required to understand thoroughly the spatter formation and finally the prevention.

6 Conclusions

The main finding of this study was the definitions of the keyhole modes, in which the keyhole behaves differently and also the molten pool has own characteristic features. To conclude the results, analysis and discussion:

- Trap mode (T-mode) results in large depth to width ratio welds with highest penetration possible. The -2.0 FPP resulted in the largest reflectivity so the laser energy was directed deeper into the material increasing penetration. This keyhole mode worked at high and low speeds and the keyhole geometry and the behaviour was the same in both of these cases.
 - Wide trap mode, a sub-mode of the trap mode, had the middle section to keyhole opening width ratio above 1.8 and this changed the weld geometry removing sharp fusion lines from the weld cross-section. The keyhole behaviour itself was the same with narrow trap mode.
- Cylinder mode (C-mode) results in a shallow and wide weld. The keyhole itself was stable but the melting efficiency suffers strongly from this keyhole mode. There was also a small risk of oscillations of the keyhole if the parameters were not optimal.
- Kaleidoscope (K-mode) occurs at full penetration, in this mode the keyhole is of almost uniform width throughout its depth (EK-mode in more detail) and this created an even weld through the whole thickness. The melting efficiency dropped with this mode noticeably. The main benefit of this mode was the even weld which caused an even heat distribution along the depth reducing heat caused distortions, which causes the bending of the welded sample.
 - Large opening kaleidoscope (LK) occurs also at full penetration mode and the root to top width ratio was above 1.8. This increased the top side weld width caused by increased heat input on the upper half of the keyhole depth. The benefit is that the LK mode increases the melting efficiency compared to EK-mode.

Another important finding was the differences of the keyholes and the welds between bead on plate (BOP) and I-butt joint (IBJ) and the process behaviour. The keyhole mode changed in some cases when the joint type changed. With IBJ there was a small bevel on the first quarter which, in some cases, changed the keyhole behaviour by removing or reducing the molten front of the keyhole on and near the sample surface allowing the keyhole opening to be located deeper into the material reducing the effects of -FPP. The joint also affected the bead reinforcement and filling capability. The maximum welding speed to obtain a bead reinforcement with such a bevel was 2.0 m/min. An even surface or almost filled bead, which means the underfilling was

less than 0.1 mm^2 , was possible using welding speeds up to 5.0 m/min. These are classified as B-class welds according to the EN standard 13919-1.

The molten metal flow, tracer flow in this case, inside the molten pool is important especially when welding special steels. This is one reason for examining the flow patterns inside the melt pool to understand more of the behaviour. The flow analysis summarises as:

- High speed trap mode results in periodic spiking of the tracer from the backside of the keyhole resulting in complete mixing depth to the root side but there is a risk of mixing being periodic and not complete through the whole weld length.
- Low speed trap mode results in periodic circulation of the tracer, which mixes the tracer efficiently into the weld, but only on the two thirds of the depth.
- Kaleidoscope mode results in the lowest tracer mixing depths likely due to two separate molten metal spiking's, one from the surface and one from the root side.

In some applications spatter might be undesired. The acceptable amount of spatter is not directly limited in the used standard, spatter was not taken into account when qualifying the welds. The prevention of spatter is important for some applications, but the analysis of the spatter formation is another topic. Some parameter combinations resulted in less spatter, such as welding speeds over 1.5 m/min with FPPs between ± 0.0 and -4.0 mm for partial penetration bead on plate and with all welding speeds with FPPs between ± 0.0 and -2.0 mm with partial penetration butt joint.

The full penetration welds had surface spatter free welds with all welding speeds between FPPs of 0.0 to -4.0 mm with both joint types. The smallest amount of root side spatter with FP bead on plate was with -6.0 mm FPP at 2.0 m/min (LK-mode, more specifically Open Cone mode), -4.0 FPP at 3 m/min and -2.0 mm FPP at 4.0 m/min, but on the latter two some droplet formation occurred. Butt joints showed similar trend, -6.0 mm FPP at 2.0 m/min had the least spatter on the root side with $+2.0$ mm FPP at 4.0 m/min, which also had some droplet formation on the root side.

7 Future work

Future studies could include several new subtopics that were not included into this thesis, such as another joint type, higher laser power and heat transfer simulations based on the actual keyhole geometry. It also would be interesting to compare a high quality machined edge with laser cut edge, because machining is in wide use in industry and also for preparation of joint edges. This type of an edge is also common but unfortunately it could not be included in this study.

One relatively important experiment, the molten pool behaviour with C-mode and WT-mode was missing from the thesis due to observations of the keyhole geometry and the molten pool behaviour during the analysis phase in Lappeenranta. The original plan was to perform limited amount of tracer experiments to achieve molten pool behaviour on certain parameter window. This is one experiment to be planned for later date to confirm the molten pool behaviour and usability of this keyhole mode with filler wire.

The average keyhole geometry was constructed into a 3D-model, but not used for simulations or in the comparison between simulation results and the actual keyhole geometry measured and calculated in this work. It would be very interesting to start simulation experiments with the calculated keyhole geometry acquired with x-ray videography. Now when there is a large database of the geometries it would be useful to add these to simulation program and compare with the weld geometry.

Third would be increasing the laser power and perform similar experiments with 15+ kW solid state laser. Would that power level have the same keyhole modes and behaviour and corresponding weld geometry? I assume that the modes are the same, but of course everything scales up with the increased laser power.

Bibliography

Abt, F & Boley, M 2011, 'X-Ray In-Situ Diagnostics of Laser based Processes', *13th International Workshop Process diagnostic and control in laser beam welding and cutting*, IFSW Universität Stuttgart, Hirschegg.

Abt, F, Boley, M, Weber, R & Graf, T 2011, 'X-ray videography for investigation of capillary and melt pool dynamics in different materials', *Proc of the Int. Congress on Applications of Laser & Electro-Optics*, Laser Institute of America, Orlando.

Abt, F, Boley, M, Weber, R & Graf, T 2012, 'X-Ray videography for investigation of capillary and melt pool dynamics in different materials', *14th International Workshop on Process diagnostic and control in laser beam welding and cutting - II*, Institut für Strahlwerkzeuge, Universität Stuttgart, Hirschegg.

Abt, F, Boley, M, Weber, R, Graf, T, Popko, G & Nau, S 2011, 'Novel X-ray System for in-situ Diagnostics of Laser Based Processes – First Experimental Results', *Physics Procedia*, vol 12, no. A, pp. 761-770.

Abt, F, Weber, R & Graf, T 2010, 'Novel high-speed space-resolver X-Ray system for in-situ diagnostics of laser based processes', *Proc of the Int. Congress on Applications of Laser & Electro-Optics*, Laser Institute of America, Anaheim.

Ambrosi, P, Bohm, J, Hilgers, G, Jordan, M & Ritzenhoff, K 1996, 'A photon spectrometer to investigate the energy spectrum and the angular distribution of photon radiation incident on a personal dosimeter', *1996 international congress on radiation protection. Proceedings. Volume 4*, International Radiation Protection Association, Vienna.

Arata, Y, Abe, E & Fujisawa, M 1976, 'A Study on Dynamic Behaviours of Electron Beam Welding (Report I) : The Observation by a Fluoroscopic Method', *Transactions of Japan Welding Research Institute*, vol 5, no. 1, pp. 1-9.

Arata, Y, Abe, N & Oda, T 1985, 'Fundamental Phenomena in High Power CO2 Laser Welding (Report I)', *Transactions of Japan Welding Research Institute*, vol 14, no. 1, pp. 5-11.

Arata, Y, Abe, N & Oda, T 1985, 'Fundamental Phenomena in High Power CO2 Laser Welding (Report II)', *Transactions of Japan Welding Research Institute*, vol 14, no. 2, pp. 17-22.

Beck, M & Dausinger, F 1989, 'Modelling of Laser Deep Welding Processes', *Proceedings of European Scientific Laser Workshop on Mathematical Simulation*, Sprechsaal Publishing Group, Lissabon.

Berger, P 2011, 'Understanding Pore Formation in Laser Beam Welding', *Physics Procedia*, vol 12, no. A, pp. 241-247.

Berger, P & Hügel, H 2013, 'Fluid dynamic effects in keyhole welding an attempt to characterize different regimes', *Physics Procedia*, vol 41, pp. 216-224.

Berger, P, Hügel, H & Graf, T 2011, 'Understanding Pore Formation in Laser Beam Welding', *Physics Procedia*, vol 12, pp. 241-247.

Bergström, D, Powell, J & Kaplan, A 2007, 'A ray-tracing analysis of the absorption of light by smooth and rough metal surfaces"', *J. of Applied Physics*, vol 101, pp. 113504/1-11.

Boley, M, Abt, F, Weber, R & Grat, T 2013, 'X-Ray and optical videography for 3D measurement of capillary and melt pool geometry in laser welding', *Physics Procedia*, vol 41, pp. 488-495.

Bushberg, J, Seibert, J, Leidholdt, E & Boone, J 2012, *The Essential Physics of Medical Imaging*, 3rd edn, Lippincott Williams & Wilkins, Philadelphia.

Chotas, H, Dobbins, J & Ravin, C 1999, 'Principles of digital radiography with large-area, electronically readable detectors: a review of the basics', *Radiology*, vol 210, pp. 595-599.

Courtois, M, Carin, M, Le Masson, P, Gaeid, S & Balabane, M 2014, 'Heat and fluid flow modeling of keyhole laser welding', *16th International Workshop on Process fundamentals of laser welding and cutting*, Institut für Strahlwerkzeuge, Universität Stuttgart, Hirshegg.

Courtois, M, Carin, M, Le Masson, P, Gaied, S & Balabane, M 2014, 'A complete model of keyhole and melt pool dynamics to analyze instabilities and collapse during laser welding', *Journal of Laser Applications*, vol 26, no. 4, pp. 042001-1-9.

Daneshkhah, R, Najafi, M & Torabian, H 2012, 'Numerical simulation of weld pool shape during laser beam welding', *Journal of Applied and Basic Sciences*, vol 3, no. 8, pp. 1624-1630.

David, S, Khan, P & Debroy, T 1988, 'Laser Beam Welding Of High-Manganese Stainless Steels-Examination of Alloying Element Loss and Microstructural Changes', *Welding Journal*, vol 67, no. 1, p. 7.

Dowden, J 2001, *The Mathematics of Thermal Modeling, An Introduction to the Theory of Laser Material Processing*, 1st edn, Chapman & Hall/CRC, Boca Raton.

Dowden, J, Postacioglu, N, Davis, M & Kapadia, P 1987, 'A keyhole model in penetration welding with a laser', *Journal of Physics D: Applied Physics*, vol 20, no. 1, pp. 36-44.

Dragoset, R, Musgrove, A, Clark, C & Martin, W 2013, 'Atomic Properties of the Elements', Periodic Table, Physical Measurement Laboratory, NIST, NIST, Gaithersburg.

Einstein, A 1916, 'Strahlungs-Emission und Absorption nach der Quantentheorie', *Verhandl. D. Deutch. Phys. Ges.*, vol 18, pp. 318-323.

EN-Standard 1994, 'EN 462-1:1994-03: Non-destructive testing; image quality of radiographs; part 1: image quality indicators (wire type); determination of image quality values', *EN ISO*, 1994.

EN-Standard 1994, 'EN 462-2: Non-destructive testing; image quality of radiographs; part 2: image quality indicators (step/hole type); determination of image quality value', *EN ISO*, 1994.

EN-Standard 1996, 'EN ISO 13919-1:1996. Welding. Electrons and laser beam welded joints. Guidance on quality levels for imperfections. Part 1: Steel.', *EN ISO*, 1996, p. 19.

Erhard, S, Giesen, A, Karszewski, M, Rupp, T, Stewen, C, Johannsen, I & Contag, K 2000, 'Novel pump design of Yb:YAG thin disc laser for operation at room temperature with improved efficiency', *OSA Trends in Optics and Photonics*, vol 34, pp. 38-44.

Erhard, S, Karszewski, M, Stewen, C, Contag, K, Voss, A & Giesen, A 2000, 'Pumping schemes for multi-kW thin disk lasers', *OSA Trends in Optics and Photonics*, vol 34, p. 78.

Eriksson, I, Gren, P, Powell, J & Kaplan, A 2010, 'New high-speed photography technique for observation of fluid flow in laser welding', *Optical Engineering*, vol 49, no. 10, pp. 1-3.

Eriksson, I, Powell, J & Kaplan, A 2013, 'Melt behavior on the keyhole front during high speed laser welding', *Optics and Lasers in Engineering*, vol 51, no. 6, pp. 735-740.

Fabbro, R 2010, 'Melt pool and keyhole behaviour analysis for deep penetration laser welding', *Physics D: Applied Physics*, vol 43, pp. 445-501.

Giesen, A, Hügel, H, Voss, A, Wittig, K, Brauch, U & Opower, H 1994, 'Scalable Concept for Diode-Pumped High-Power Solid-State Lasers', *Journal of Applied Physics, B*, vol 58, pp. 365-372.

Giesen, A & Speiser, J 2007, 'Fifteen Years of Work on Thin-Disk Lasers: Results and Scaling Laws', *IEEE Journal of Selected topics in quantum electronics*, vol 13, no. 3, pp. 598-609.

Halmshaw, R 1997, *Introduction to the Non-Destructive Testing of Welded Joints*, 2nd edn, Woodhead Publishing Ltd.

Hecht, E 2002, *Optics*, 4th edn, Addison-Wesley Longman, Incorporated, Boston.

Heß, A 2012, *Vorteile und Herausforderungen beim Laserstrahlschweißen mit Strahlquellen höchster Fokussierbarkeit*, Universität Stuttgart, Stuttgart.

Honda, H, Tsukamoto, S, Kawaguchi, I & Arakane, G 2010, 'Keyhole behavior in deep penetration CO2 laser welding', *Journal of Laser Applications*, vol 22, no. 2, pp. 43-47.

Hubbell, J 1969, *Photon Cross Sections, Attenuation Coefficients, and Energy Absorption Coefficients From 10 keV to 100 GeV*, National Bureau of Standards, Washington, D.C.

Hubbell, J 1999, 'Review of photon interaction cross section data in the medical and biological context', *Physics in Medicine and Biology*, vol 44, pp. R1-R22.

Hubbell, J & Seltzer, S 2004, 'Tables of X-Ray Mass Attenuation Coefficients and Mass Energy-Absorption Coefficients', National Institute of Standards and Technology, Gaithersburg.

Hügel, H 2000, 'New solid-state lasers and their application potentials', *Optics and Lasers in Engineering*, vol 34, pp. 213-229.

Hügel, H & Dausinger, F 1999, 'Interaction phenomena and energy coupling in laser treatment processes', in D Schuöcker (ed.), *Euro laser Academy*, 2nd edn, Chapman & Hall, Stuttgart.

Jin, X, Li, L & Zhang, Y 2002, 'A study on fresnel absorption and reflections in the keyhole in deep penetration laser welding', *Journal of Physics D: Applied Physics*, vol 35, p. 2304.

Jokinen, T 2004, *Novel ways of using Nd:YAG laser for welding thick section austenitic stainless steel*, VTT Industrial Systems, Lappeenranta.

Jokinen, T & Kujanpää, V 2003, 'High power Nd:YAG laser welding in manufacturing of vacuum vessel of fusion reactor', *Fusion Engineering and Design*, vol 69, pp. 349-353.

Jung, R, Nickles, P, Sander, W, Schoennagel, H, Stiel, H, Tümmeler, J & Will, I 2009, 'Disk laser with high pulse energy', *5th International workshop on fiber lasers*, Fraunhofer IWS, Dresden.

Kaplan, A, Mizutani, M & Katayama, S 2002, 'Keyhole Laser Spot Welding', *Proc of the Int. Congress on Applications of Laser & Electro-Optics*, Laser Institute of America, Scottsdale.

Katayama, S & Kawahito, Y 2009, 'Elucidation of Phenomena in High Power Fiber Laser Welding, and Development of Prevention Procedures of Welding Defects', *Proc. of SPIE*, vol 7195, no. 71951R, pp. 1-9.

Katayama, S, Kawahito, Y & Mizutani, M 2007, 'Collaboration of physical and metallurgical viewpoints for understanding and process development of laser welding', *Proc of the Int. Congress on Applications of Laser & Electro-Optics*, Laser Institute of America, Orlando.

Katayama, S, Seto, N, Mizutani, M & Matsunawa, A 2001, 'X-Ray Transmission In-Situ Observation of Keyhole during Laser Spot Welding and Pulse-Shaping for Prevention of Porosity', *Proc. of the Int. Congress on Applications of Laser & Electro-Optics*, Laser Institute of America, Jacksonville.

Kawahito, Y, Matsumoto, N, Abe, Y & Katayama, S 2011, 'Relationship of laser absorption to keyhole behavior in high power fiber laser welding of stainless steel and aluminum alloy', *J. of Materials Processing Technology*, vol 211, pp. 1563-1568.

Kinoshita, K, Mizutani, M, Kawahito, Y & Katayama, S 2006, 'Phenomena of welding with high-power fiber laser', *Proc of the Int. Congress on Applications of Laser & Electro-Optics*, Laser Institute of America, Orlando.

Körner, M, Weber, C, Wirth, S, Pfeifer, K-J, Reiser, M & Traitl, M 2007, 'Advances in Digital Radiography: Physical Principles and System Overview', *Radiographics*, vol 27, no. 3, pp. 675-686.

Lappalainen, E, Unt, A, Sokolov, M, Vänskä, M & Salminen, A 2013, 'Laser welding with high power laser: The effect of joint configuration', *14th Conference on Nordic Laser Materials Processing (NOLAMP)*, Luleå tekniska universitet, Gothenburg.

Leo, W 1987, *Techniques for Nuclear and Particle Physics Experiments*, Springer-Verlag, Berlin.

Li, S, Chen, G, Zhang, M, Zhou, Y & Zhang, Y 2014, 'Dynamic keyhole profile during high-power deep-penetration laser welding', *Journal of Materials Processing Technology*, vol 214, pp. 565-570.

Lippold, J & Kotecki, D 2005, *Welding metallurgy and weldability of stainless steels*, 1st edn, John Wiley & Sons, New Jersey.

Maiman, T 1960, 'Stimulated Optical Radiation in Ruby', *Nature*, vol 187, no. 4736, pp. 493-494.

MaTeck GmbH 2008, 'MaTeck's Periodic Table of the Elements', Table, MaTeck GmbH, Juelich.

Matsumoto, N, Kawahito, Y, Mizutani, N & Katayama, S 2008, 'Laser absorption in high-power fiber laser welding of stainless steel and aluminium alloy', *Proc. of the Int. Congress on Applications of Lasers & Electro-Optics*, Laser Institute of America, Temecula.

Matsunawa, A 2002, 'Science of Laser Welding - Mechanisms of Keyhole and Pool Dynamics -', *21st International Congress on Applications of Lasers & Electro optics*, Laser Institute of America, Scottsdale.

Matsunawa, A, Kim, J-D, Seto, N, Mizutani, M & Katayama, S 1998, 'Dynamics of keyhole and molten pool in laser welding', *Journal of Laser Applications*, vol 10, no. 6, pp. 247-254.

Matsunawa, A & Semak, V 1996, 'The simulation of front keyhole wall dynamics during laser welding', *Journal of Physics D: Applied Physics*, vol 30, no. 5, pp. 798-.

Naito, Y, Mizutani, M & Katayama, S 2006, 'Effect of oxygen in ambient atmosphere on penetration characteristics in single yttrium aluminum garnet laser and hybrid welding', *Journal of Laser Applications*, vol 18, no. 1, pp. 21-27.

Nariyama, N, Umetani, K, Shinohara, K, Kondoh, T, Kurihara, A & Fukumoto, M 2011, 'Micro-Scale Dose Distribution of Microplanar X Rays from Synchrotron Radiation: Measurement and Monte Carlo Calculation', *Progress in NUCLEAR SCIENCE and TECHNOLOGY*, vol 2, pp. 312-317.

Olsen, F 2011, 'Laser cutting from CO2 laser to disc or fiber laser - possibilities and challenges', *30th International Congress on Applications of Lasers & Electro-optics*, Laser Institute of America, Orlando.

Prokop, M & Schaefer-Prokop, C 1997, 'Digital image processing', *European Radiology*, vol 7, no. 3, pp. 73-82.

Rai, R 2008, *Modeling of heat transfer and fluid flow in keyhole mode welding*, Pennsylvania State University, State College.

Salminen, A, Lehtinen, J & Harkko, P 2008, 'The effect of welding parameters on keyhole and melt pool behaviour during laser welding with high power fiber laser', *Proc. of the Int. Congress on Applications of Lasers & Electro-Optics*, Laser Institute of America, Temecula.

Schawlow, A & Townes, C 1958, 'Infrared and Optical Masers', *Physical Review*, vol 112, no. 6, pp. 1940-1949.

Semak, V, Bragg, W, Damkroger, B & Kempka, S 1999, 'Transient model for the keyhole during laser welding', *Journal of Physics D: Applied Physics*, vol 32, pp. L61-L64.

Shimokusu, Y, Fukumoto, S, Nayama, M, Ishide, T, Tsubota, S, Matsunawa, A & Katayama, S 2002, 'Application of 7 kW class high power yttrium-aluminum-garnet laser welding to stainless steel tanks', *Journal of Laser Applications*, vol 14, no. 2, pp. 68-72.

Sokolov, M, Salminen, A, Somonov, V & Kaplan, A 2012, 'Laser welding of structural steels: Influence of the edge roughness level', *Optics and Laser Technology*, vol 44, no. 7, pp. 2064-2071.

Trincavelli, J & Castellano, G 2008, 'The prediction of thick target electron bremsstrahlung spectra in the 0.25–50 keV energy range', *Spectrochimica Acta Part B*, vol 63, pp. 1-8.

Tsukamoto, S, Arakane, G, Kawaguchi, I & Honda, H 2003, 'Keyhole Behaviour in High Power Laser Welding of Thick Steel Plates - Formation Mechanism And Suppression of Weld Defects -', *Proc. of the 22nd International Congress on Applications of Lasers & Electro-Optics*, Laser Institute of America, Jacksonville.

Tünnemann, A, Zellmer, H, Schöne, W, Giesen, A & Contag, K 2000, *New concepts for diode-pumped solid-state lasers*, Springer-Verlag, Berlin.

Van Grieken, R & Markowicz, A 2002, *Handbook of X-Ray Spectrometry*, 2nd edn, Marcel Dekker Inc., New York.

Weberpals, J & Dausinger, F 2008, 'Fundamental understanding of spatter behaviour at laser welding of steel', *Proc. of the Int. Congress on Applications of Lasers and Electro-Optics*, Laser Institute of America, Temecula.

Weberpals, J, Hermann, T, Berger, P & Singpiel, H 2011, 'Utilisation of Thermal Radiation for Process Monitoring', *Physics Procedia*, vol 12, no. A, pp. 704-711.

Webster, P, Wright, L, Mortimer, K, Leung, B, Yu, J & Fraser, J 2011, 'Automatic real-time guidance of laser machining with inline coherent imaging', *Journal of Laser Applications*, vol 23, no. 2, pp. 1-6.

Weldingh, J & Kristensen, J 2001, 'Very deep penetration laser welding - techniques and limitations', *8th Conference on Nordic Laser Materials Processing (NOLAMP)*, Technical University of Denmark, Copenhagen.

Westin, E 2010, *Microstructure and properties of welds in the lean duplex stainless steel LDX 2101*, Royal Institute of Technology, Stockholm.

Westin, E & Fellman, A 2010, 'Effect of laser and laser hybrid welding on the corrosion performance of a lean duplex stainless steel', *Journal of Laser Applications*, vol 22, p. 13.

Volpp, J 2012, 'Investigation on the influence of different laser beam intensity distributions on keyhole geometry during laser welding', *Physics Procedia*, vol 39, pp. 17-26.

Vänskä, M, Abt, F, Weber, R, Salminen, A & Graf, T 2012, 'Investigation of the keyhole in laser welding of different joint geometries by means of X-Ray videography', *Proc of the Int. Congress on Applications of Laser & Electro-Optics*, Laser Institute of America, Anaheim.

Vänskä, M, Abt, F, Weber, R, Salminen, A & Graf, T 2013, 'Effects of welding parameters onto keyhole geometry for partial penetration laser welding', *Physics Procedia*, vol 41, pp. 199-208.

Vänskä, M, Abt, F, Weber, R, Salminen, A & Graf, T 2014, 'Effects of welding parameters and joint geometry to keyhole geometry and vapour volume', *16th International Workshop on Process fundamentals of laser welding and cutting*, Institut für Strahlwerkzeuge, Universität Stuttgart, Hirschegg.

Vänskä, M & Salminen, A 2012, 'Laser welding of stainless steel self-steering tube-to-tube joints with oscillating mirror', *Proc. of the Institution of Mechanical Engineers, Part B: Journal of Engineering Manufacture*, vol 226, pp. 632-640.

Yasuaki, N, Mizutani, M & Katayama, S 2003, 'Observation of Keyhole Behavior and Melt Flows during Laser-Arc Hybrid Welding', *Proc of the Int. Congress on Applications of Laser & Electro-Optics*, Laser Institute of America, Jacksonville.

Zhang, X, Ashida, E, Katayama, S & Mizutani, M 2008, 'Development of ultra deep penetration welding with 10 kw fiber laser', *Proc of the Int. Congress on Applications of Laser & Electro-Optics*, Laser Institute of America, Temecula.

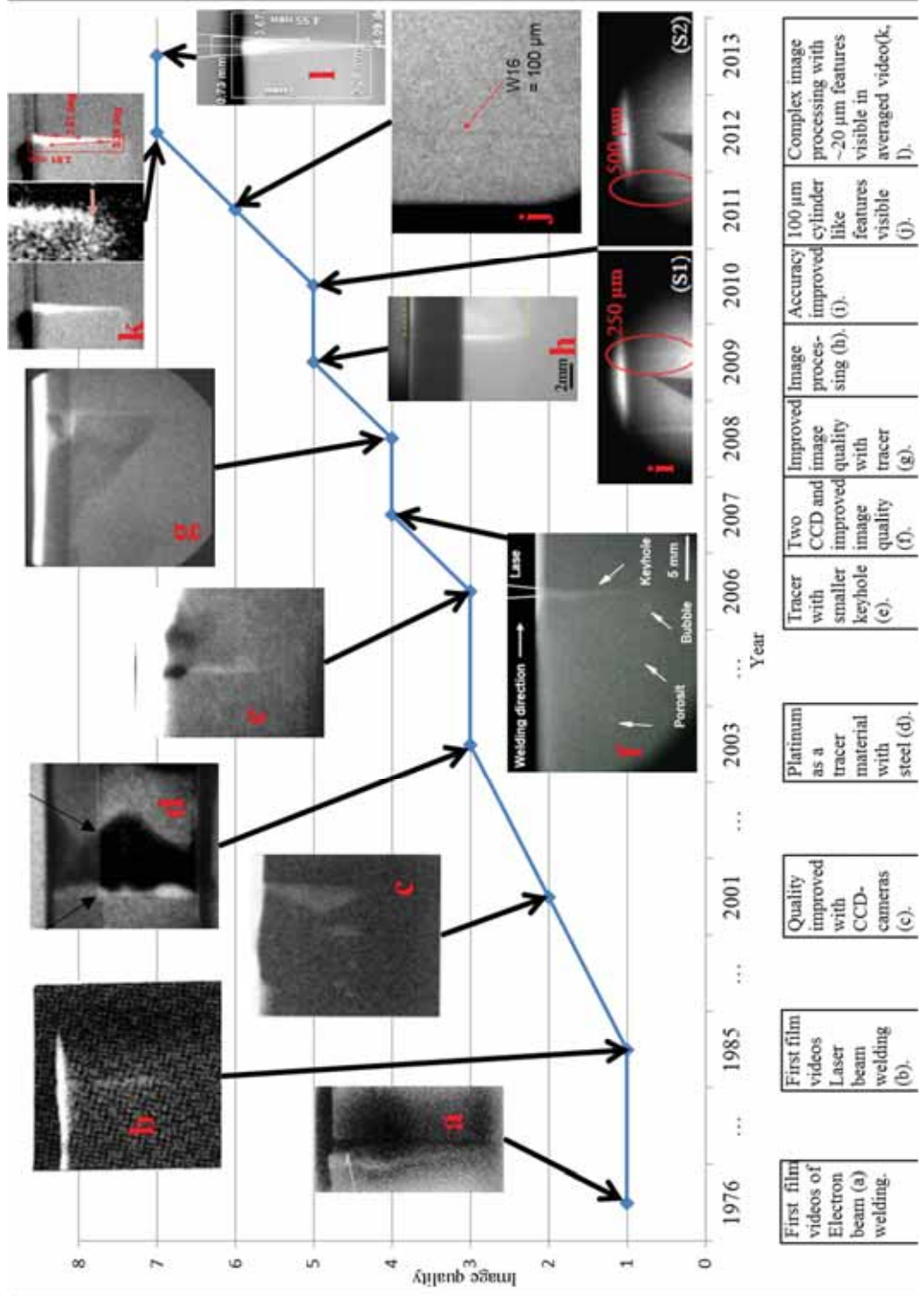
Zhang, X, Ashida, E, Tarasawa, S, Anma, Y, Okada, M, Katayama, S & Mizutani, M 2009, 'Welding of thick stainless steel plates up to 50mm with high brightness lasers', *Proc of the Int. Congress on Applications of Laser & Electro-Optics*, Laser Institute of America, Orlando.

Zhao, L, Tsukamoto, S & Arakane, G 2009, 'Influence of oxygen on weld geometry in fibre laser welding', *Proc of the Int. Congress on Applications of Laser & Electro-Optics*, Laser Institute of America, Orlando.

Appendices

Appendix 1. History of x-ray imaging in laser welding.....	1
Appendix 2. Image quality and image processing complexity.....	3
Appendix 3. Keyhole cross-section areas in the welding direction, PP.....	4
Appendix 4. Keyhole cross-section areas in the welding direction, FP.....	5
Appendix 5. PP samples, bead on plate weld cross-sections.....	6
Appendix 6. PP samples, butt joint weld cross-sections.....	7
Appendix 7. FP samples, bead on plate weld cross-sections.....	8
Appendix 8. FP samples, butt joint weld cross-sections.....	9
Appendix 9. PP samples, bead on plate weld top sides.....	10
Appendix 10. PP samples, thickness butt joint weld top sides.....	11
Appendix 11. FP sample's bead on plate weld top sides.....	12
Appendix 12. FP sample's bead on plate weld root sides.....	13
Appendix 13. FP sample's butt joint weld top sides.....	14
Appendix 14. FP sample's butt joint weld root sides.....	15
Appendix 15. Tracer weld cross-sections and weld top sides.....	16
Appendix 16. Tracer weld cross-sections and weld surfaces.....	17
Appendix 17. PP samples, keyhole side view outlines.....	18
Appendix 18. FP samples, keyhole side view outlines.....	19
Appendix 19. Keyhole openings, PP BOP.....	20
Appendix 20. Keyhole openings, PP IBJ.....	21
Appendix 21. Keyhole openings, FP BOP.....	22
Appendix 22. Keyhole openings, FP IBJ.....	23
Appendix 23. Laser beam generation and modern disk lasers.....	24
Appendix 24. Mass attenuation coefficient.....	25
Appendix 25. Image processing procedure with examples.....	29

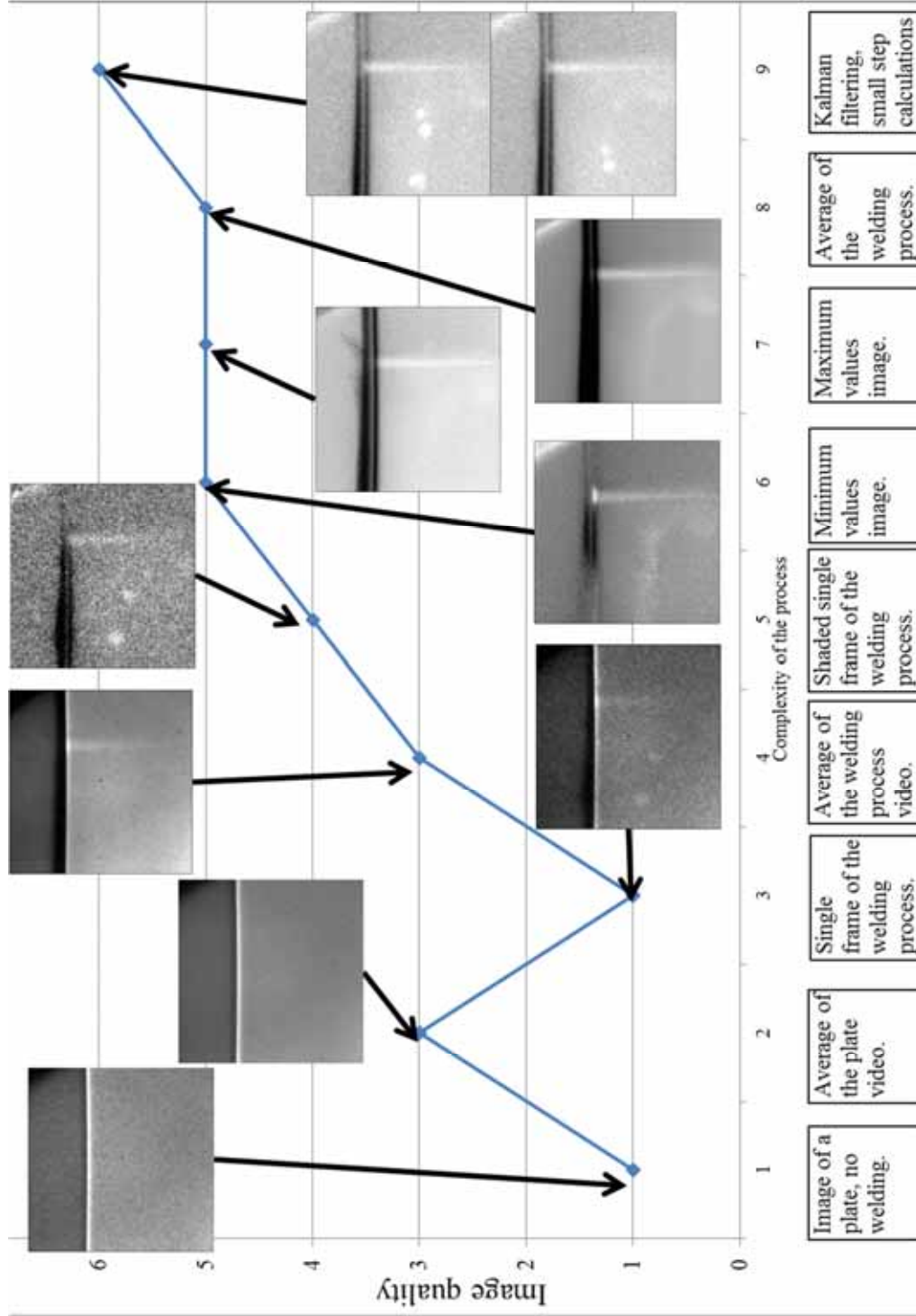
Appendix 1. History of x-ray imaging in laser welding



References for the previous figure.

- a. (Arata, Abe & Fujisawa 1976)
- b. (Arata, Abe & Oda 1985)
- c. (Katayama et al. 2001)
- d. (Tsukamoto et al. 2003)
- e. (Kinoshita et al. 2006)
- f. (Katayama, Kawahito & Mizutani 2007)
- g. (Zhang et al. 2008)
- h. (Zhang et al. 2009)
- i. (Abt, Weber & Graf 2010)
- j. (Abt et al. 2011)
- k. (Vänskä et al. 2012)
- l. (Vänskä et al. 2013).

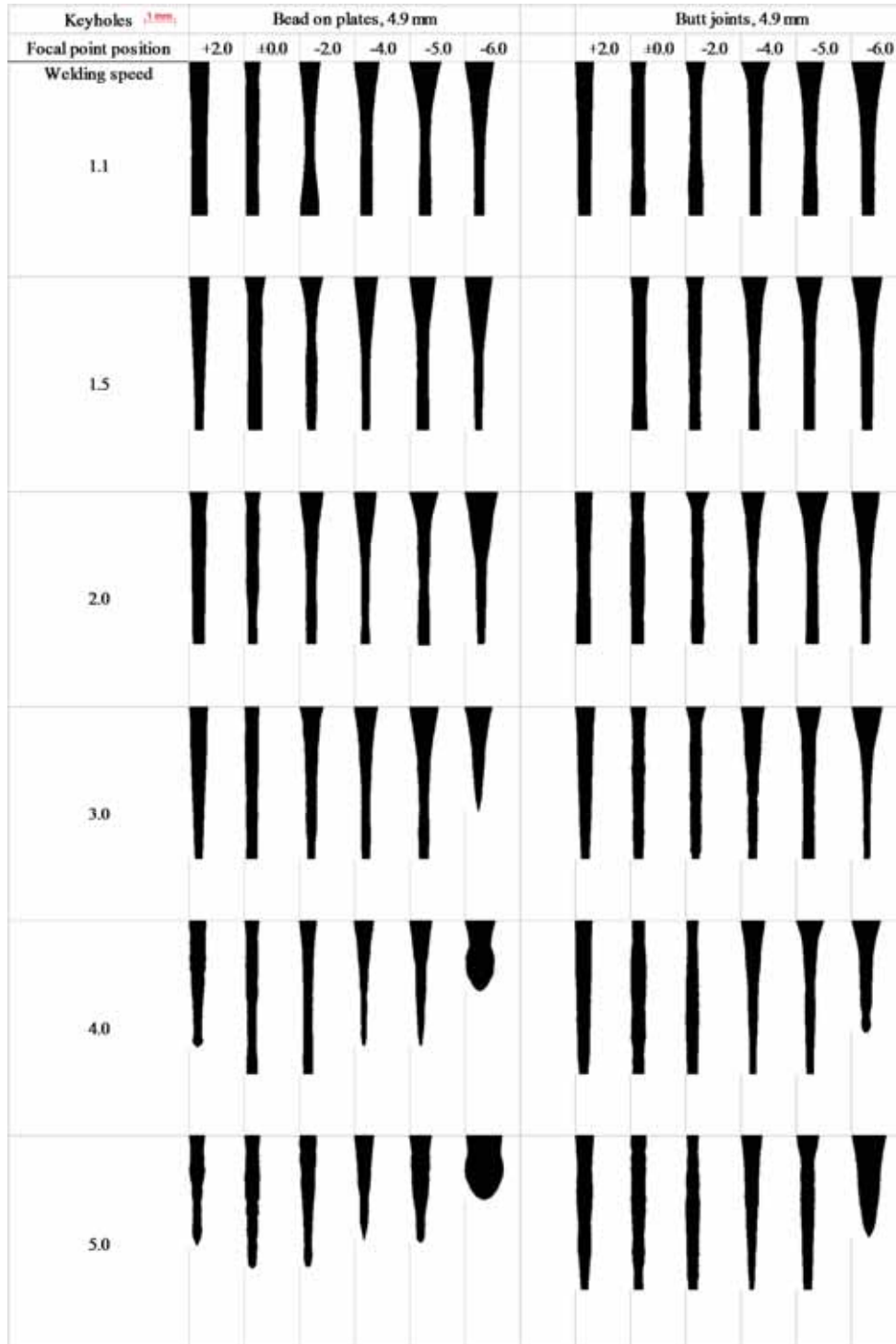
Appendix 2. Image quality and image processing complexity



Appendix 3. Keyhole cross-section areas in the welding direction, PP

Keyholes <small>1 mm</small>	Bead on plates, 7.8 mm						Butt joints, 7.8 mm					
Focal point position	+2.0	+0.0	-2.0	-4.0	-5.0	-6.0	+2.0	+0.0	-2.0	-4.0	-5.0	-6.0
Welding speed												
1.1												
1.5												
2.0												
3.0												
4.0												
5.0												

Appendix 4. Keyhole cross-section areas in the welding direction, FP



Appendix 5. PP samples, bead on plate weld cross-sections

Welds <small>1mm</small>		Bead on plates, 7.8 mm					
Focal point position	+2.0	+0.0	-2.0	-4.0	-5.0	-6.0	
Welding speed							
1.1							
1.5							
2.0							
3.0							
4.0							
5.0							

Appendix 6. PP samples, butt joint weld cross-sections

Welds <small>1mm</small>		Butt joints, 7.8 mm					
Focal point position	+2.0	+0.0	-2.0	-4.0	-5.0	-6.0	
Welding speed							
1.1							
1.5							
2.0							
3.0							
4.0							
5.0							

Appendix 7. FP samples, bead on plate weld cross-sections

Welds		Bead on plates, 4.9 mm					
Focal point position		+2.0	±0.0	-2.0	-4.0	-5.0	-6.0
Welding speed							
1.1							
1.5							
2.0							
3.0							
4.0							
5.0							

Appendix 8. FP samples, butt joint weld cross-sections

Welds 		Butt joints, 4.9 mm					
Focal point position		+2.0	±0.0	-2.0	-4.0	-5.0	-6.0
Welding speed							
L1							
1.5							
2.0							
3.0							
4.0							
5.0							

Appendix 9. PP samples, bead on plate weld top sides

Top sides		Bead on plates, 7.8 mm					
Focal point position	+2.0	+0.0	-2.0	-4.0	-5.0	-6.0	
Welding speed							
1.1							
1.5							
2.0							
3.0							
4.0							
5.0							

Appendix 10. PP samples, thickness butt joint weld top sides

Top sides	Butt joints, 7.8 mm					
Focal point position	+2.0	+0.0	-2.0	-4.0	-5.0	-6.0
Welding speed						
1.1						
1.5						
2.0						
3.0						
4.0						
5.0						

Appendix 11. FP sample's bead on plate weld top sides

Top sides	Bead on plates, 4.9 mm					
Focal point position	+2.0	±0.0	-2.0	-4.0	-5.0	-6.0
Welding speed						
1.1						
1.5						
2.0						
3.0						
4.0						
5.0						

Appendix 12. FP sample's bead on plate weld root sides

Root sides	Bead on plates, 4.9 mm					
Focal point position	+2.0	±0.0	-2.0	-4.0	-5.0	-6.0
Welding speed						
1.1						
1.5						
2.0						
3.0						
4.0						
5.0						

Appendix 13. FP sample's butt joint weld top sides

Top sides	Butt joints, 4.9 mm					
Focal point position	+2.0	±0.0	-2.0	-4.0	-5.0	-6.0
Welding speed						
1.1						
1.5						
2.0						
3.0						
4.0						
5.0						

Appendix 14. FP sample's butt joint weld root sides

Root sides	Butt joints, 4.9 mm					
Focal point position	+2.0	+0.0	-2.0	-4.0	-5.0	-6.0
Welding speed						
1.1						
1.5						
2.0						
3.0						
4.0						
5.0						

Appendix 15. Tracer weld cross-sections and weld top sides

Weld	1	2	3	4	5
I 1 mm Cross-section					
Cross-section II					
I 1 mm Top sides					
Weld	6	7	8	9	10
Cross-section					
Cross-section II					
Top sides					

Appendix 16. Tracer weld cross-sections and weld surfaces

Weld	11	12	13	14	15
I 1 mm Cross-section					
Cross-section II					
I 1 mm Top side					
Weld	16	16, root	17	17, root	
Cross-section					
Cross-section II					
Top/root sides					

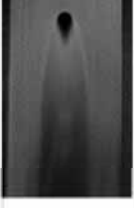
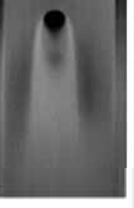
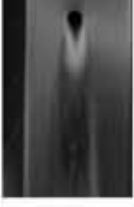
Appendix 17. PP samples, keyhole side view outlines

Keyhole side view	Bead on plates, 7.8 mm						Butt joints, 7.8 mm					
Focal point position	+2.0	+0.0	-2.0	-4.0	-5.0	-6.0	+2.0	+0.0	-2.0	-4.0	-5.0	-6.0
Welding speed 1.1												
1.5												
2.0												
3.0												
4.0												
5.0												

Appendix 18. FP samples, keyhole side view outlines

Keyhole side view	Bead on plates, 4.9 mm						Butt joints, 4.9 mm					
Focal point position	+2.0	+1.0	-2.0	-4.0	-5.0	-6.0	+2.0	+1.0	-2.0	-4.0	-5.0	-6.0
Welding speed 1.1												
1.5												
2.0												
3.0												
4.0												
5.0												

Appendix 19. Keyhole openings, PP BOP

Key openings		Bead on plates, 7.8 mm					
Focal point position	+2.0	+0.0	-2.0	-4.0	-5.0	-6.0	
Welding speed							
1.1							
1.5							
2.0							
3.0							
4.0							
5.0							

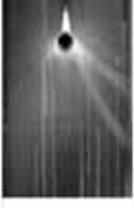
Appendix 20. Keyhole openings, PP IBJ

KII openings	I-butt joints, 7.8 mm					
Focal point position	+2.0	+0.0	-2.0	-4.0	-5.0	-6.0
Welding speed						
1.1						
1.5						
2.0						
3.0						
4.0						
5.0						

Appendix 21. Keyhole openings, FP BOP

Key openings		Bead on plates, 4.9 mm					
Focal point position	+2.0	+0.0	-2.0	-4.0	-5.0	-6.0	
Welding speed							
1.1							
1.5							
2.0							
3.0							
4.0							
5.0							

Appendix 22. Keyhole openings, FP IBJ

KII openings	I-butt joints, 4.9 mm					
Focal point position	+2.0	+0.0	-2.0	-4.0	-5.0	-6.0
Welding speed						
1.1						
1.5						
2.0						
3.0						
4.0						
5.0						

Appendix 23. Laser beam generation and modern disk lasers

The process starts with a pump light (940 nm wavelength photons) in the case of a disk laser and this pump light is absorbed by the laser active atoms (actually an electron in an atom orbit). When the atom absorbs the pump photon, the electron in the atom orbit is excited, meaning that it rises to a higher energy level state from the ground state (higher orbit in the atom, the further the electron is in the atom orbit the higher the energy state is). Then a spontaneous emission happens, which means that the electron is moved back to the lower energy state, by itself, releasing a photon of certain wavelength connected to the atom properties. In the case of Yb:YAG-laser, a disk laser, the emitted photon wavelength is 1030 nm. Spontaneous emission has a random direction of travel, so the photons can travel any direction inside the resonator. When these emitted photons (1030 nm) collides with already excited atoms a same wavelength, same direction and same phase photon is emitted and the electron returns to ground state; and the result is two photons of same wavelength, direction and phase. The high intensity of a laser is based on the back and front mirrors of the resonator. During the process of generating the laser beam most of the 1030 nm photons travel in the direction of these back and front mirrors. The back mirror is high reflective mirror (HR) and front mirror is partly reflecting, also called as output coupler. The result is a one wavelength, one phase and one main travel direction laser beam which has high intensity. The light, the photons travels a straight path are electromagnetic radiation and the electromagnetic field direction is according to a sine wave. This means that when the photon moves, the electromagnetic force field direction it emits changes according to the sine wave form, figure 1, right image. (Einstein 1916) (Schawlow & Townes 1958) (Maiman 1960) (Hecht 2002)

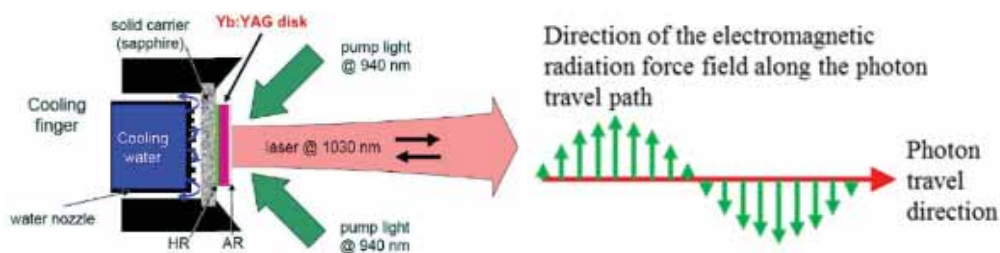


Figure 1. Basic principle of a disk laser and photon travel. (Jung et al. 2009) (Hecht 2002)

The principle of a thin disk laser was introduced first time in the beginning of 1990's by Giesen et al. from University of Stuttgart. (Giesen et al. 1994) The main component in a disk laser resonator is the Yb:YAG-disk, ytterbium in yttrium aluminium garnet, the YAG mixture is a synthetic crystal material which is doped with ytterbium atoms to act as laser active medium. The disk is usually around 100-200 μm thick and diameter several millimetres and is connected to a heat sink which keeps the crystal at optimal temperature. Figure 2 shows the principle of a pumping system of the crystal. The pumping can be performed axially or radially, this eliminates the need to design the system according to the pumping method, which allows more

freedom in design (Hügel 2000). Thin disk method results in temperature gradient mainly in coaxial direction and axial temperature distribution is almost uniform. This type of temperature distribution only affects slightly to beam propagation through the disk and results in high beam quality. Multiple pump beam passes are used to increase the absorption of the active elements thus increasing the maximum achievable laser power from one disk. For example with 32 pump-beam passes through the disk result in pump power absorption level of 90 %. Also the multiple passes allow use of a thinner disk and lower doping concentration. (Giesen & Speiser 2007) (Erhard et al. 2000) (Erhard et al. 2000) (Tünnemann et al. 2000)

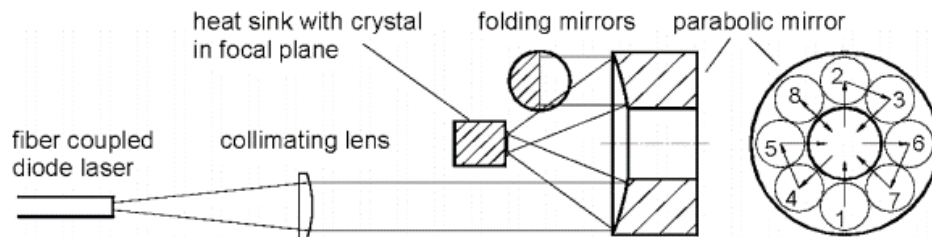


Figure 2. Pumping principle of a thin disk laser with 16 pump beam passes. (Giesen & Speiser 2007)

Appendix 24. Mass attenuation coefficient

Mass attenuation coefficient (MAC) (absorption or scattering probability when photons are travelling a layer of a material with density dependence removed) μ/ρ is the quotient of dN/N divided by $\rho \times dl$, dN/N is the fraction of particles that does interact when travelling a distance of dl in a material that has the density of ρ , and this is valid for uncharged particles. This results in an equation 1 as the mass attenuation coefficient in m^2/kg . When taking the equation apart to understand more of the mass attenuation coefficient, the μ is linear attenuation coefficient [$1/m$] and the probability that a particle is interacting in the material layer of thickness dl is μ divided by dl . μ is also depending on the density ρ . This dependency is mainly neglected by using mass attenuation coefficient. (Hubbell 1969) (Hubbell 1999)

$$\frac{\mu}{\rho} = \frac{1}{\rho \times dl} \frac{dN}{N} \quad (1)$$

The x-ray spectrum does not have a single wavelength, but rather a broadband emission of photons at different energies. The photon energy is connected to the wavelength, which determines the spectrum for x-ray-term. In most cases, the x-rays are at or below approximately 1 \AA (Ångström) in length, which is 0.1 nm . The minimum wavelength is determined by the x-ray machine properties, mainly the potential difference. The equation for calculating the short-wavelength limit is given in equation 2. (Van Grieken & Markowicz 2002)

$$\lambda_{min} = \frac{hc}{eV_0} \quad (2)$$

λ_{min} is the short-wavelength of the x-ray system in nanometres, h is the Planck's constant in Js, c is the speed of light in m/s, e is the electron charge in coulombs and V_0 is the potential difference in the tube in voltages. The short-wavelength limit for the used x-ray system according to equation 2 is 0.00886 nm . This has an effect on the attenuation; the higher the photon energy is the easier it penetrates the material. In other words, shorter wavelengths penetrate the material more efficiently and the material type itself has smaller effect on the penetrability difference. This is valid for photon energies in the x-ray region and UV, visible and infra-red photon energy ranges acts differently. The photon penetration throughout the whole electro-magnetic radiation spectrum is not linear and photoelectric absorption edges causes even more disturbance to the interaction probability.

The photon energy can be calculated using equation 3. The mass attenuation coefficient tables have been calculated for different photon energies and so the min-max range of the x-ray emission is needed to convert to eV form. (Hubbell & Seltzer 2004)

$$E = \frac{hc}{\lambda} \quad (3)$$

E is the photon energy in eV. By these two equations the electron volt range for the used x-ray tube is 13.78 to 139.94 keV. In figure 1 is shown iron and molybdenum mass attenuation coefficients and also for iron and tungsten. The dip and sudden increase in molybdenum at 20 keV is caused by photoelectric absorption edge. The edge is caused by K-shell binding energy; the electron more likely absorbs a photon just above the binding energy level than a photon just below the binding energy level. Although the drop is significant, it has only a small effect in x-ray videography due to large emission band of the x-ray tube and small portion of the band is affected by the photoelectric absorption edge. (Bushberg et al. 2012) To compare the photon energies of different wavelengths few examples are given. Blue light with a wavelength of 445 nm has the photon energy of 2.8 eV and a laser beam from a disk laser with 1030 nm wavelength has photon energy of 1.2 eV. The x-ray beams average photon energy is around 80 000 eV. Gamma rays, which are emitted from radioactive atoms are picometre range in wavelength and so has photon energies around 1 200 000 eV. The electro-magnetic radiation is always absorbed in metals, tissue and all materials, but the mechanic and depth is changed according to emitted photon energies.

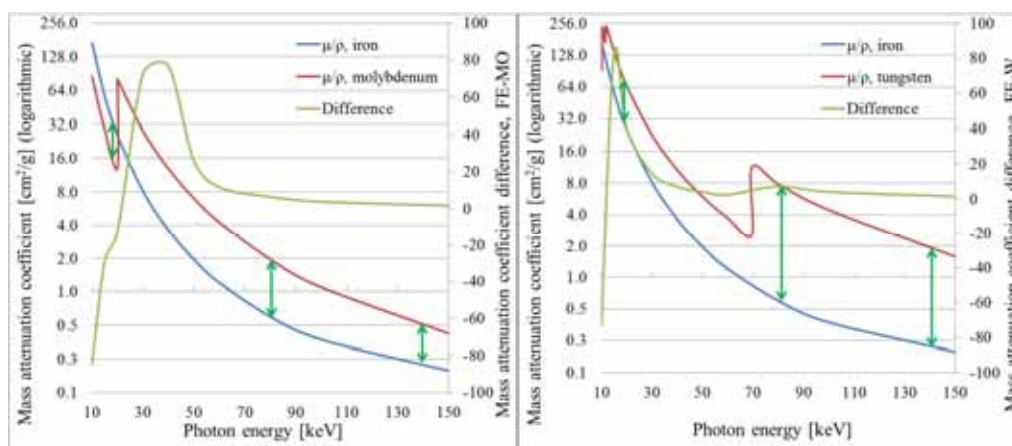


Figure 1. Mass attenuation coefficients. Green arrows points minimum, average and maximum photon energies.

The average attenuation difference for molybdenum vs iron is 22.3, maximum 76.9 and minimum 0.3. The average for iron vs tungsten is 8.9, maximum 81.8 and minimum 1.4. The minus marked values were removed due to insignificance to the visibility of the filler in that area. According to these graphs the tungsten has an advantage of acting as a tracer material due to higher difference at maximum emission area of the x-ray tube at around 80 keV. Even though the MAC difference is higher with tungsten, it has few disadvantages such as considerably higher melting temperature than iron, 3410 vs 1535 °C, for tungsten and iron respectively. If tungsten would be used as a wire, the melting behaviour would be significantly different due to possibility of unmelted wire in the molten pool. The boiling temperature difference is 5657 and 2750 for tungsten and iron respectively. These differences make the usability of a tungsten wire

questionable. Due to high attenuation at low energy levels the photon energy range below 20 keV, for all materials, should not have any effect to image contrast. There is very little information of the photon energy distribution from the x-ray tube, but few studies were found. Figure 2 shows relative x-ray beam intensity behind a 3 mm copper plate. The x-ray voltage was not described, but it is likely in the area of 300 kV, which results in approximately in 300 keV of maximum photon energy, according to short-wavelength equation. Ambrosi et al. measured spectral distribution with 160 kV potential and it resulted in a maximum intensity peak at around 70-90 keV. (Nariyama et al. 2011) (Ambrosi et al. 1996)

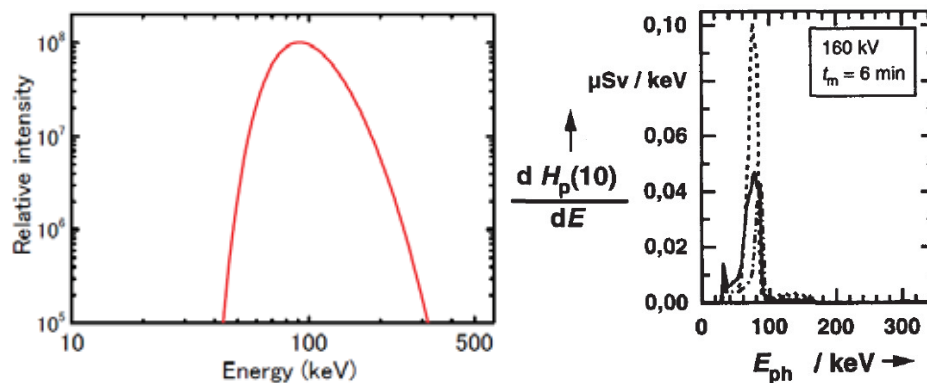


Figure 2. X-ray dose behind 3 mm copper plate and medical test on right. (Nariyama et al. 2011) (Ambrosi et al. 1996)

The spectrum and intensity distribution measurements show that the main range is from 20 to 300 keV, depending on the x-ray tube potential. Most of the studies of the area concerns medical devices and lower energy level devices, in which the potential is lower and photon energies also lower, maximum of 20 to 50 keV. (Trincavelli & Castellano 2008) The absorption, mass attenuation, difference causes contrast difference to the x-ray video, the higher the attenuation the lower the intensity at the scintillator and so in the camera. The tracer material use is based on these phenomena; this allows identifying and tracking the molten pool size, flow pattern and in some cases even molten metal flow speed.

Appendix 25. Image processing procedure with examples

The first step after image acquisition is to cut the shading videos into appropriate length that there are no black images in the video. The second step is to compile an average intensity image of the video. The averaging process first stores each pixels grey values along the whole video. Then a compilation all these values into one image is required, forming one image. Figure 1 shows two images, first is a single frame from the shading video and second is an average image of the whole shading video. As shown there are optical, system and imaging flaws, such as slightly uneven x-ray dose, spatters on the protection plate and the structure of the scintillator.

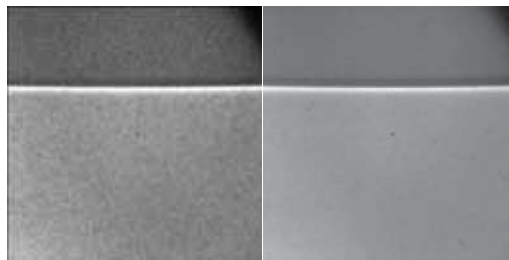


Figure 1. On left a single frame from shading video and on right an average image of the whole video.

After the shading average is compiled, a welding video is taken into the process. Figure 2 has a single frame from the welding video and an average of the welding process. The flaws are still clearly visible and this disturbs the analysis. The keyhole is visible, but the bottom tip is partly mixed into the scintillator structure. The uneven x-ray dose is disturbing several areas of the image and in some cases excessive x-ray dose can even look like uneven sample width.

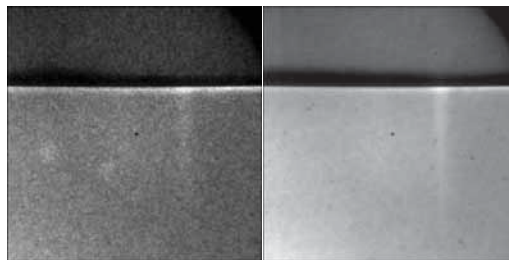


Figure 2. Single frame from welding on left and average of the welding process.

The shading means that the complete welding video is divided by the shading average. Figure 3 shows the same frames as in the previous figure, except that they have been shaded. The main difference is that the bubbles are more visible and also the keyhole. It looks like that the signal-to-noise ratio is slightly worse, but is in fact the same; the image looks differently due to removal of system flaws. The other image shows the average of the shaded welding video. As shown the keyhole is much more visible, the bubble flow is clearly visible and even top side of

the sample is visible, which were not clearly visible in the unprocessed average. In these images, a multiline sample top is shown, the sample top is not one single sharp line in this case due to misalignment of the sample to the x-ray tube.

Many different Z-Project methods are commonly used. Z-Project means that the program projects certain Z-values, pixel grey values along time. $X \times Y$ being the image width and height and Z is the time, a stack of images or a video in other words. The amount of images per video ranged from 1000 to 5000 in this study, depending on the welding speed. Minimum and maximum pixel values results in new types of images which gives the lowest and highest x-ray dose values, for example minimum and maximum keyhole sizes, main spatter direction on top of the sample and main bubble flow pattern. Figure 3 shows minimum and maximum pixel value images of the same process as previous figures.

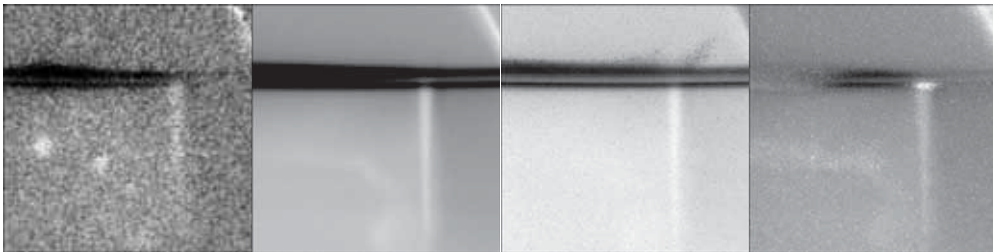


Figure 3. Single frame from the shaded welding video, shaded welding video average and minimum and maximum pixel values images.

As shown above, image processing of stacks can give very different results depending on the process and still be accurate when considering average geometries and average or main behaviour of the bubble flow for example. The weld length in above series is approximately 40 mm. In minimum values image the spattering above the surface is more visible, especially the main direction of travel can be determined. In maximum values image the bubble flow is more distinguishable and the keyhole opening. Kalman stack filtering is an image stack process that increases the image quality but the time resolution will suffer. It is based on small step averaging calculations. Figure 4 presents three single frames from Kalman stack filtered welding process video. The bubbles are more visible and bubble flow pattern can be determined. The keyhole is clearly visible, except the very small tip in the keyhole bottom.

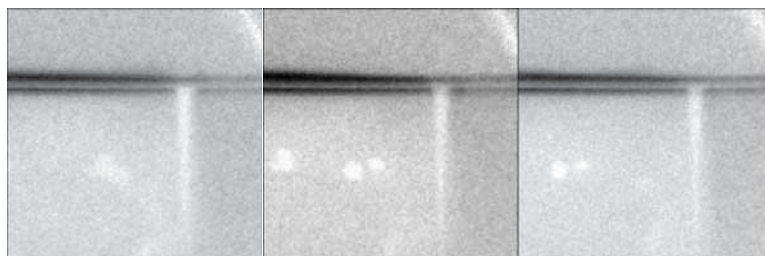


Figure 4. Three frames 200 ms from each other with shading and Kalman stack filtering.

As shown, digital image processing is a very powerful tool, especially in x-ray videography. It can help in the analysis process and some features are more visible after processing. The most critical issue with image processing is the possible deletion of data from the images. It is plausible that some of the features are lost during the processing, for example large contrast increase with some adjustment to brightness can remove some of the features. This can also add features to the image which are not really present; these features would be ghost features rather than actual features in the process. Automatic contrast and brightness adjustment usually results in a valid analysis, especially if the image processing software is well build that it preserves most of the features. Automatic contrast and brightness was used during the image processing in this study, it mainly helps in the recognition of the keyhole walls, which was done manually with automatic adjustment.

ACTA UNIVERSITATIS LAPPEENRANTAENSIS

- 587.** PHAM, THUY DUONG. Ultrasonic and electrokinetic remediation of low permeability soil contaminated with persistent organic pollutants. 2014. Diss.
- 588.** HOKKANEN, SANNA. Modified nano- and microcellulose based adsorption materials in water treatment. 2014. Diss.
- 589.** HINKKANEN, JUHA. Cooperative strategy in emerging markets – analysis of interfirm R&D cooperation and performance in Russian manufacturing companies. 2014. Diss.
- 590.** RUSKOVAARA, ELENA. Entrepreneurship education in basic and upper secondary education – measurement and empirical evidence. 2014. Diss.
- 591.** IKÄHEIMONEN, TUULI. The board of directors as a part of family business governance – multilevel participation and board development. 2014. Diss.
- 592.** HAJIALI, ZUNED. Computational modeling of stented coronary arteries. 2014. Diss.
- 593.** UUSITALO, VILLE. Potential for greenhouse gas emission reductions by using biomethane as road transportation fuel. 2014. Diss.
- 594.** HAVUKAINEN, JOUNI. Biogas production in regional biodegradable waste treatment – possibilities for improving energy performance and reducing GHG emissions. 2014. Diss.
- 595.** HEIKKINEN, JANNE. Vibrations in rotating machinery arising from minor imperfections in component geometries. 2014. Diss.
- 596.** GHALAMCHI, BEHNAM. Dynamic analysis model of spherical roller bearings with defects. 2014. Diss.
- 597.** POLIKARPOVA, MARIIA. Liquid cooling solutions for rotating permanent magnet synchronous machines. 2014. Diss.
- 598.** CHAUDHARI, ASHVINKUMAR. Large-eddy simulation of wind flows over complex terrains for wind energy applications. 2014. Diss.
- 599.** PURHONEN, MIKKO. Minimizing circulating current in parallel-connected photovoltaic inverters. 2014. Diss.
- 600.** SAUKKONEN, ESA. Effects of the partial removal of wood hemicelluloses on the properties of kraft pulp. 2014. Diss.
- 601.** GUDARZI, DAVOOD. Catalytic direct synthesis of hydrogen peroxide in a novel microstructured reactor. 2014. Diss.
- 602.** VALKEAPÄÄ, ANTTI. Development of finite elements for analysis of biomechanical structures using flexible multibody formulations. 2014. Diss.
- 603.** SSEBUGERE, PATRICK. Persistent organic pollutants in sediments and fish from Lake Victoria, East Africa. 2014. Diss.
- 604.** STOKLASA, JAN. Linguistic models for decision support. 2014. Diss.
- 605.** VEPSÄLÄINEN, ARI. Heterogenous mass transfer in fluidized beds by computational fluid dynamics. 2014. Diss.

606. JUVONEN, PASI. Learning information technology business in a changing industry landscape. The case of introducing team entrepreneurship in renewing bachelor education in information technology in a university of applied sciences. 2014. Diss.
607. MÄKIMATTILA, MARTTI. Organizing for systemic innovations – research on knowledge, interaction and organizational interdependencies. 2014. Diss.
608. HÄMÄLÄINEN, KIMMO. Improving the usability of extruded wood-plastic composites by using modification technology. 2014. Diss.
609. PIRTTILÄ, MIIA. The cycle times of working capital: financial value chain analysis method. 2014. Diss.
610. SUIKKANEN, HEIKKI. Application and development of numerical methods for the modelling of innovative gas cooled fission reactors. 2014. Diss.
611. LI, MING. Stiffness based trajectory planning and feedforward based vibration suppression control of parallel robot machines. 2014. Diss.
612. KOKKONEN, KIRSI. From entrepreneurial opportunities to successful business networks – evidence from bioenergy. 2014. Diss.
613. MAIJANEN-KYLÄHEIKO, PÄIVI. Pursuit of change versus organizational inertia: a study on strategic renewal in the Finnish broadcasting company. 2014. Diss.
614. MBALAWATA, ISAMBI SAILON. Adaptive Markov chain Monte Carlo and Bayesian filtering for state space models. 2014. Diss.
615. UUSITALO, ANTTI. Working fluid selection and design of small-scale waste heat recovery systems based on organic rankine cycles. 2014. Diss.
616. METSO, SARI. A multimethod examination of contributors to successful on-the-job learning of vocational students. 2014. Diss.
617. SIITONEN, JANI. Advanced analysis and design methods for preparative chromatographic separation processes. 2014. Diss.
618. VIHAVAINEN, JUHANI. VVER-440 thermal hydraulics as computer code validation challenge. 2014. Diss.
619. AHONEN, PASI. Between memory and strategy: media discourse analysis of an industrial shutdown. 2014. Diss.
620. MWANGA, GASPER GODSON. Mathematical modeling and optimal control of malaria. 2014. Diss.
621. PELTOLA, PETTERI. Analysis and modelling of chemical looping combustion process with and without oxygen uncoupling. 2014. Diss.
622. NISKANEN, VILLE. Radio-frequency-based measurement methods for bearing current analysis in induction motors. 2014. Diss.
623. HYVÄRINEN, MARKO. Ultraviolet light protection and weathering properties of wood-polypropylene composites. 2014. Diss.
624. RANTANEN, NOORA. The family as a collective owner – identifying performance factors in listed companies. 2014. Diss.